Mechanics of Hybrid Metal Matrix Composites

Jessica Anne Dibelka

Dissertation submitted to the faculty of
the Virginia Polytechnic Institute and State University
in partial fulfillment of the requirements for the degree of

Doctor of Philosophy
in
Engineering Mechanics

Scott W. Case, Chair
Romesh C. Batra
Robert H. Carter
Brian Y. Lattimer
Anne E. Staples

March 26, 2013
Blacksburg, Virginia

Keywords: Continuous Fiber, Discontinuous Fiber, Alumina, Aluminum Matrix,
Progressive Failure

MECHANICS OF HYBRID METAL MATRIX COMPOSITES

JESSICA ANNE DIBELKA

The appeal of hybrid composites is the ability to create materials with properties which normally do not coexist such as high specific strength, stiffness, and toughness. One possible application for hybrid composites is as backplate materials in layered armor. Fiber reinforced composites have been used as backplate materials due to their potential to absorb more energy than monolithic materials at similar to lower weights through microfragmentation of the fiber, matrix, and fiber-matrix interface. Composite backplates are traditionally constructed from graphite or glass fiber reinforced epoxy composites. However, continuous alumina fiber-reinforced aluminum metal matrix composites (MMCs) have superior specific transverse and specific shear properties than epoxy composites. Unlike the epoxy composites, MMCs have the ability to absorb additional energy through plastic deformation of the metal matrix. Although, these enhanced properties may make continuous alumina reinforced MMCs advantageous for use as backplate materials, they still exhibit a low failure strain and therefore have low toughness. One possible solution to improve their energy absorption capabilities while maintaining the high specific stiffness and strength properties of continuous reinforced MMCs is through hybridization. To increase the strain to failure and energy absorption capability of a continuous alumina reinforced Nextel™ MMC, it is laminated with a high failure strain Saffil® discontinuous alumina fiber layer. Uniaxial tensile testing of hybrid composites with varying Nextel™ to Saffil® reinforcement ratios resulted in composites with non-catastrophic tensile failures and an increased strain to failure than the single reinforcement Nextel™ MMC. The tensile behavior of six hybrid continuous and discontinuous alumina fiber reinforced MMCs are reported, as well as a description of the mechanics behind their unique behavior. Additionally, a study on the effects of fiber damage induced during processing is performed to obtain accurate as-processed fiber properties and improve single reinforced laminate strength predictions. A stochastic damage evolution model is used to predict failure of the continuous Nextel™ fabric composite which is then applied to a finite element model to predict the progressive failure of two of the hybrid laminates.

ACKNOWLEDGEMENTS

The author would like to thank the following people for their contributions to this work:

- Dr. Scott W. Case for subtly guiding me in the right direction and sharing your knowledge and expertise with me.
- Drs. Romesh C. Batra, Robert H. Carter, Brian Y. Lattimer, and Anne E. Staples for taking time out of their busy schedules to improve my performance as a researcher.
- Drs. Eric M. Klier and Robert H. Carter for funding my dissertation research and lending their time and knowledge of all things MMC.
- Army Research Laboratory for financially supporting this work.
- Drs. Michael W. Hyer, Romesh C. Batra, Scott W. Case, David A. Dillard, and Jack J. Lesko for being very influential in my solid mechanics education and future endeavors.
- Frances M. Davis and Tim B. Hartman for laughing, practicing, editing, questioning, and celebrating with me during this journey.
- Beverly Williams and Lisa Smith for your kindness and the countless tasks you performed to keep me on track.
- Dr. William A. Curtin for graciously giving me the tensile simulation FORTRAN code.
- Jim P. Sorensen at CPS Technologies for manufacturing the MMC laminates especially, the hybrid composites.
- Triton Systems, Inc. for donating the raw Nextel™ fiber.

DEDICATION

The author would like to dedicate this work to:

- Baylee Dibelka for being happy even when it rains and always making me smile. I couldn't have done this without you.
- Anthony C. Santago: I've made thousands of wonderful memories while being at VT but the best part was finding you.

TABLE OF CONTENTS

LIST OF FIGURES

LIST OF TABLES

Research was sponsored by the Army Research Laboratory and was accomplished under Cooperative Agreement Number W911NF-06-2-0014. The views and conclusions contained in this document are those of the authors and should not be interpreted as representing official policies, either expressed or implied, of the Army Research Laboratory or the U.S. Government. The U.S. Government is authorized to reproduce and distribute reprints for Government purposes notwithstanding any copyright notation heron.

1 INTRODUCTION

Layered armor systems consisting of a hard strike face and ductile backing can defeat projectiles at lower weights than traditional steel armor, increasing the fuel efficiency and mobility of armored vehicles [1], Figure 1. Upon projectile impact, the ceramic strike face dissipates energy through brittle failure and fragmentation while the backplate supports the strike face and further absorbs impact energy [2]. Fiber-reinforced composites have been used as backplate materials because they have the potential to absorb more energy than monolithic materials at similar or lower weights through microfragmentation of the fiber, matrix, and fiber-matrix interface [3]. Brittle epoxy matrix composites reinforced with S2-glass fiber have demonstrated a greater impact resistance than carbon and E-glass reinforced composites due to their higher strain to failure [3]. However, the use of continuous alumina fiber reinforced aluminum metal matrix composites (MMCs) as backplate materials may prove advantageous due to their specific transverse and shear material properties. Continuous alumina reinforced MMCs have higher specific transverse and specific shear properties than glass reinforced epoxy composites [4]. Plastic deformation of the metal matrix can result in increased energy absorption capabilities compared to epoxy matrices, which fail due to brittle cracking. Figure 2 is a scanning electron microscope image of a continuous alumina reinforced MMC tensile fracture surface showing three major modes of energy absorption or microfragmentation: ductile deformation in the matrix rich regions, debonding and pull-out at the fiber-matrix interface, and fiber fracture. Although continuous alumina reinforced aluminum MMCs have enhanced specific properties and energy absorption capabilities for ballistic applications, they still exhibit low failure strains. In this work, hybrid composites were made by laminating the continuous alumina fiber reinforced MMC with a short alumina fiber reinforced MMC to improve the breaking strain and toughness while maintaining the high specific strength and specific stiffness of continuous alumina fiber reinforced MMC.

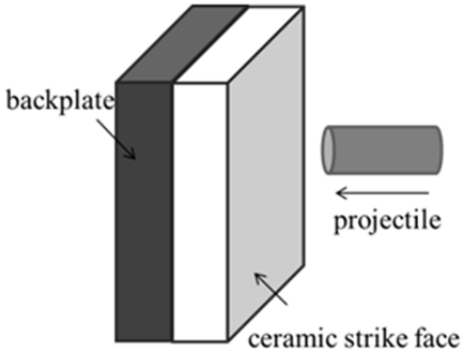

Figure 1. Layered armor system schematic.

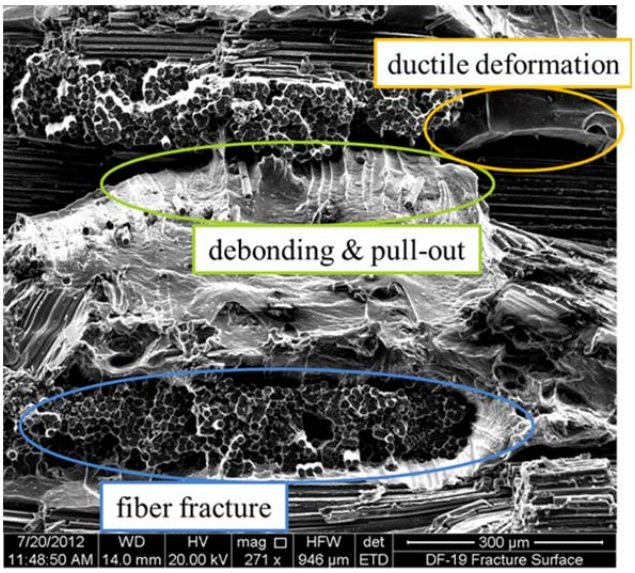

Figure 2. MMC fracture surface showing microfragmentations due to tensile loading.

The appeal of hybrid composites is the ability to create materials with properties which normally do not coexist such as high specific strength, specific stiffness and toughness. Hybrid composites consist of at least two load bearing components with different failure strains and can be constructed with intermingled or interlaminated reinforcements [5]. Intermingled hybrid composites have multiple reinforcements in the same layer while interlaminated hybrids have one reinforcement per layer. To increase the breaking strain of brittle particle composites, a short fiber reinforcement was added to create a successful intermingled hybrid [6, 7]. Titanium or iron mesh and particulate intermingled hybrids possess improved stiffness, tensile strength, hardness, and yield strength than the titanium wire composite alone [8-10]. Hybrid fiber metal laminates

(FMLs) consisting of interlaminated layers of metal and polymer fiber composites have improved toughness and impact performance over their base components [11]. Continuous fiber reinforced hybrids are intermingled or interlaminated and consist of high (HE) and low (LE) elongation fibers in an epoxy matrix. HE/LE continuous fiber reinforced hybrids have displayed a positive hybrid effect by exhibiting a higher breaking strain than the LE composite [5, 12-15]. A similar approach as the interlaminated HE/LE continuous hybrids is implemented in this work. The low failure strain continuous alumina fabric MMC is laminated with a high failure strain discontinuous alumina fiber MMC resulting in a mixed property hybrid laminate with improved toughness.

The interlaminated hybrid composite investigated in this study, referred to as a continuous/discontinuous hybrid MMC, was reinforced with a high strength, high stiffness, and low failure strain, continuous Nextel™ 610 fabric layer and a high failure strain, discontinuous, randomly oriented Saffil® layer. Tensile testing of continuous/discontinuous hybrid composites revealed a non-catastrophic tensile failure, which resulted in a positive hybrid effect, with a strain to failure greater than that of the continuous reinforced composite. In an effort to understand the mechanisms causing the non-catastrophic failure which prolonged ultimate failure, increased toughness, and therefore the amount of energy the composite absorbed during failure six hybrid laminates were tested in uniaxial tension. To predict the behavior of hybrid composites not tested in this study, the beginnings of a hybrid model will be developed incorporating a continuous reinforced composite strength model and a finite element simulation. Cracking in the continuous reinforced hybrid layer is predicted through a damage evolution model which uses constituent properties (fiber and matrix) and geometry as inputs. As-processed continuous fiber properties were characterized to support modeling and will be reported. The hybrid model used here which consists of the continuous strength predictions and discontinuous composite experimental results will be used to predict the non-catastrophic failure behavior of two hybrid laminates. Predicting the response of the discontinuous layer is a future goal in working towards a hybrid composite model and is beyond the scope of the current study. The long term goal of this work is to develop a model which predicts the tensile behavior of hybrid composites using fiber and matrix properties alone to identify continuous/discontinuous reinforced hybrid laminates which have improved properties for ballistic applications.

2 LITERATURE REVIEW

Hybrid composites allow for materials to be created with mixed properties that either single reinforced composite alone does not have. Aveston and Kelly define a hybrid composite as a material consisting of two load bearing components each having different strain to failures [5]. One type of hybrid composite investigated in the literature consists of low (LE) and high (HE) elongation continuous fiber reinforcements within an epoxy matrix. A positive hybrid effect indicated by a 91% increase in cracking strain has been measured for a hybrid with carbon (LE) and glass (HE) reinforcements, significantly increasing the energy absorption capabilities of the carbon composite [15]. A common feature in fiber reinforced composites with a positive hybrid effect is a non-catastrophic tensile failure, Figure 3 path (0ABCD). Non-catastrophic failure for LE/HE (continuous/continuous) fiber reinforced hybrids consists of the LE layer cracking many times while transferring load into the HE layer. The cracking and load transferring process prolongs failure until the HE layer is no longer able to sustain the overall applied load. Similar non-catastrophic behavior has been observed for the continuous/discontinuous alumina reinforced MMCs of interest in this study, Figure 19. During tensile loading of one of the continuous/discontinuous MMCs, a crack propagated through the outer continuous fabric layers, resulting in a 10% decrease in the axial stress. Then, the hybrid reloaded until another crack propagated through the fabric layer. This cracking and reloading process occurred multiple times until a catastrophic crack propagated through the inner discontinuous layer and ultimate failure occurred.

The following literature review focuses on modeling of continuous fiber reinforced LE/HE hybrid composites. These hybrid composites have been extensively studied by researchers and exhibit a similar failure behavior as the continuous/discontinuous hybrid. Many computational methods have been used to predict the behavior of unidirectional continuous fiber reinforced LE/HE hybrid composites including lamination theories, rule of mixtures approaches, statistical methods, damage evolution models, and fracture mechanics. This review will focus on the statistical methods and damage evolution models employed. Statistical methods can quantify the scatter in composite strengths, an important feature required for use of these materials in design. Damage evolution models have the ability to capture the saw tooth failure behavior seen in the

hybrid MMC. LE/HE hybrid composites studied in the literature were limited to unidirectional reinforcements with linear elastic fiber and matrix properties.

One of the first attempts to predict hybrid composite tensile behavior was performed by Zweben [16]. In an effort to simplify a continuous fiber reinforced hybrid composite consisting of LE and HE yarns, Zweben idealized the composite as being composed of an array of aligned alternating LE and HE composite strands within an epoxy matrix. Statistical strength characteristics for the composite strands were used instead of single fiber failure strain statistics. The length of each composite strand was divided into sections and randomly assigned a failure strain. Upon straining the composite, when a fiber section failure strain is exceeded, the section is considered broken. The strain carried by the broken segment is then transferred to the neighboring HE composite strands within the plane of the break. Strain concentration factors on the HE strands were determined using a closed-form solution. Initial failure was assumed to occur when the axial failure strain of a HE section was reached. Strain concentration factors calculated in this model are overly simplified, only allowing strain to transfer to the two HE strands next to the broken LE strand. The strain increase on the neighboring HE strands will have little effect on the overall composite behavior due to their high elongation failure strains. In practice, an increase in strain on the HE strands will result in a small increase in strain for the LE strands next to the HE strands. The small increase in strain on LE fibers two strands away from the broken segment will be substantial compared to their low elongation failure strains and may induce failure of these segments. This oversimplified model ignores strain transfer to intact LE strands within the plane of the break resulting in high failure strain predictions compared to experimental results.

Aveston and Kelly addressed hybrid cracking strain as an important hybrid composite characteristic [5] and attempted to predict the cracking strain and failure strain for hybrid composites. Figure 3 is an idealized hybrid axial stress-axial strain curve under uniaxial tension. The hybrid composite follows path (0ABCD) where A represents the initiation of cracking in the LE layer, section AB is where multiple cracks are forming within the LE layer and load is being transferred into the HE layer, ultimate failure of the composite occurs at C. Curve (0AHFG) is the behavior for the LE and HE layers loaded together but they are not joined and no stress is transferred between the layers when the LE layer cracks and unloads at A leaving only the HE

layer to carry load. Due to the addition of the HE layer and the multiply cracking hybrid behavior significantly higher strains are reached in the hybrid composites compared to the LE layer alone which fails at point A. Experimental cracking strains (symbol x) and failure strains (symbol o) are plotted in Figure 4 along with Zweben's solution for multiple hybrid composite HE fiber volume fractions [16]. Hybrid composites with less than 50% glass fibers (HE fiber) have failure strains similar to the carbon epoxy composite (LE fiber composite). Above 50% HE fiber hybrids have multiple cracks occurring within the LE layer and increasing failure strains up to three times higher than the LE composite failure strain. For HE fiber volume fractions above 60% the hybrid cracking strain is slightly increasing compared to the LE fiber reinforced composite failure strain. Hybrid composites with higher cracking strains also have higher failure strains. All hybrid failure strains are lower than the HE fiber reinforced composite (glass-epoxy). A measure of toughness in uniaxial tension is equal to the area under the stress-strain curve, Figure 5. Similar to the hybrid failure and cracking strains, initially the hybrid area is similar to the LE composite area until 60% HE fibers. At this hybrid HE fiber volume fraction the area under the stress-strain curve increases and multiple cracks are observed in the LE layer. At higher volume fractions of HE fiber the hybrid area plateaus and is always less than the HE fiber reinforced composite area. Aveston and Kelly identified hybrid cracking strain as an important property of hybrid composites. The hybrid cracking strain is directly related to failure strain for the glass-carbon-epoxy hybrid composite investigated in their study. Additionally, Aveston and Kelly recognized the importance of the multiply cracking LE layer and reported area under the stress-strain curve for multiple hybrid composites. As the HE fiber volume fraction is increased an increase in cracking strain, failure strain, and area occurred around 60%. Failure strains up to 3 times higher and areas up to 7 times higher than the LE fiber reinforced composite were reported. The findings in their study followed a similar trend as Zweben's [16] theoretical solution for hybrid composites. Aveston and Kelly also indicate that the interlaminated hybrid composite should always have outer HE composite layers to bridge the cracks of the inner LE composite and obtain non-catastrophic tensile behavior.

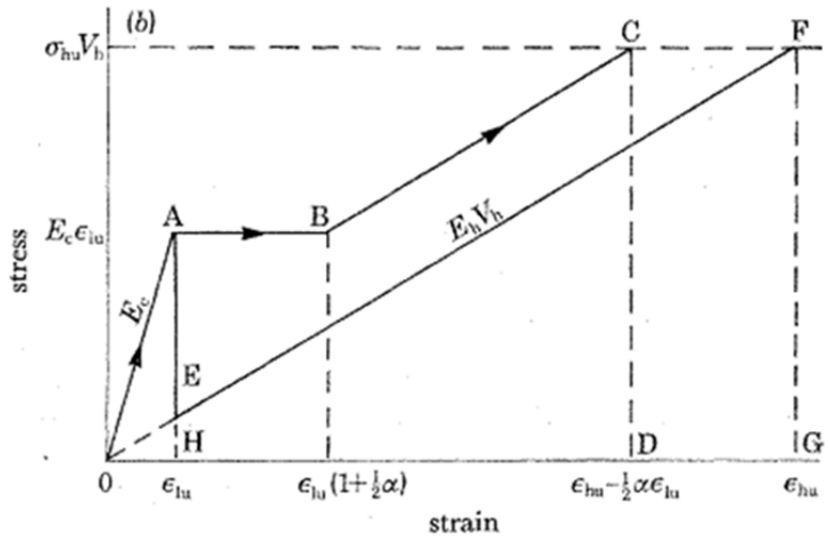

Figure 3. Idealized hybrid composite axial stress-axial strain curve for interlaminated layers (0ABCD) and un-joined layers loaded together (0AHFG) [5] by permission of the Royal Society, Section 11.3.

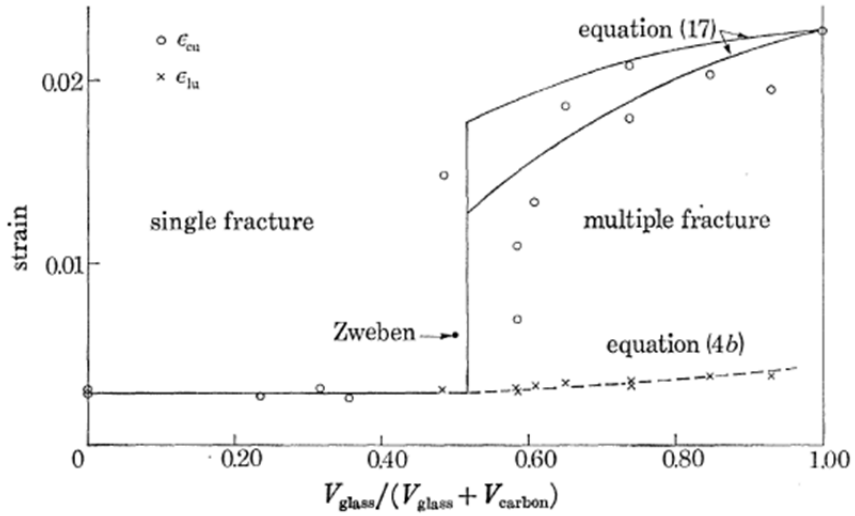

Figure 4. Hybrid composite cracking and failure strain for composites with various amounts of HE fiber [5] by permission of the Royal Society see Section 11.3.

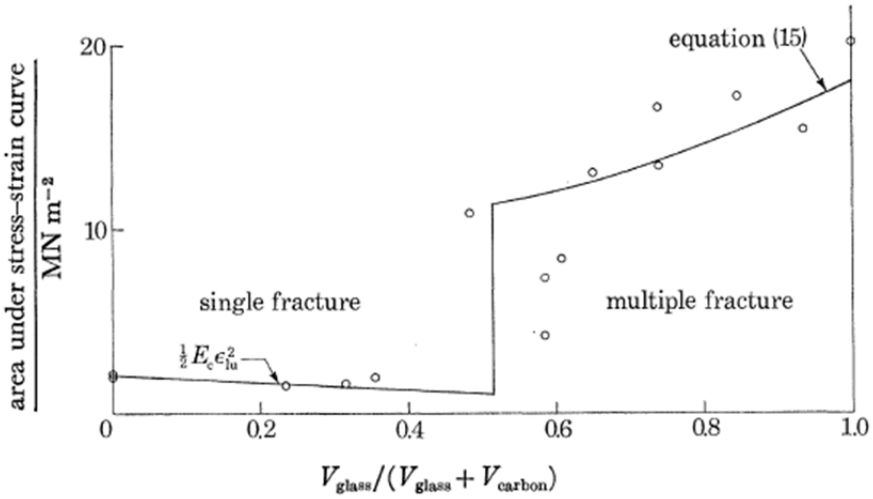

Figure 5. Hybrid composite area under the stress-strain curve for composites with various amounts of the HE fiber [5] by permission of the Royal Society see Section 11.3.

Fukunaga et al. developed a statistical approach based on a weakest link composite bundle model to predict the first tensile failure of interlaminated unidirectional carbon and glass fiber reinforced epoxy hybrid [17]. In this composite the LE and HE layers consisted of carbon and glass fiber with the LE layer sandwiched between two HE layers. Due to the complex nature of strain transfer between individual fibers after failure, a bundle approach was used. Each fiber was modeled as a chain of short fiber bundles in series. Each composite bundle was assigned a failure strain based on fiber failure strain statistics. The weakest link approach used for this model defined the first bundle failure to occur when it satisfied the Tsai-Hill failure criterion. When a bundle breaks, strain was transferred to the remaining bundles within the plane of the break. Linear elastic behavior was assumed for all composite bundles. Bundles within the HE layer were not permitted to fail and prediction of the hybrid initial failure strength was assumed to occur when all bundles in the LE layer failed. This approach was not capable of capturing the non-catastrophic tensile failure behavior of the hybrid however it was successful at predicting hybrid cracking strain.

A statistical model to predict the tensile behavior of unidirectional reinforced intraply hybrid composites was developed by Fariborz, Yang, and Harlow [14]. The hybrid composite was modeled as a fiber reinforced tape with a single row of high and low modulus fibers. Linear

elastic isotropic properties were assumed for the materials used in this model. Spacing between the fibers was defined by composite volume fractions. The row of fibers was partitioned into short sections or bundles equal to the ineffective length of the high modulus fiber. The breaking strains for each composite bundle were distributed using the Weibull common cumulative distribution function (CDF). A Monte Carlo approach was used to randomly assign breaking strains based on each composite's Weibull distribution. Local load sharing was assumed in the model, which evenly distributed the load from a broken bundle to the two nearest intact bundles along the ineffective length. Ineffective length is the length over which load is effectively transferred from a broken to an unbroken fiber. Using this approach, hybrid composite breaking strains were under predicted when compared to experimental results. In some cases, predictions were half the breaking strain found experimentally. This is believed to be due to the over simplified assumptions made on the ineffective length being independent of matrix properties and the load sharing rule being the same for all fiber breaking scenarios. Although calculating stress concentration factors for the load sharing of every breaking scenario is computationally very expensive, it would improve predictions from this model. Positive aspects to this approach are the ability to predict breaking strains for many bundle volume fractions and dispersions of the fiber types, as well as the ability to predict composite breaking strains for samples sized on the same scale as the experimental tests. Conclusions from the analysis included that a two parameter Weibull CDF accurately represented the hybrid breaking strain distribution. When fiber moduli were drastically different, even dispersion of the fibers in the composite resulted in the greatest hybrid effect or the largest increase in failure strain compared to the failure strain of the LE composite. Composite simulations which had groups of high modulus fibers or poor dispersion of LE/HE fibers, resulted in decreased composite breaking strains. The greatest hybrid effect occurred when the fibers had vastly different failure strains but similar moduli. This probability method was able to characterize the scatter in hybrid composite strengths and was used to perform a parametric study to determine the fiber properties and dispersions, which optimized the hybrid effect.

Fariborz and Harlow improved their previous intermingled hybrid composite model by improving the stress concentration factors using a shear lag analysis [18]. The shear lag model developed was applicable for random placement of LE and HE fibers and therefore easily

adapted to predict failure of hybrid composites with various degrees of dispersion and volume ratios. The stress concentration factor shear lag model accounted for the order in which fibers failed. In their previous study, load was shared equally to the surrounding intact fibers regardless of the sequence of failures [14]. A linear elastic behavior assumption was made and the hybrid strength was determined from the breaking strain based on the rule of mixtures prediction of the elastic modulus. This modified model was able to capture the hybrid effect and predict tensile breaking strains with improved accuracy compared to their previous model.

Jones and DiBenedetto investigated how hybrid behavior is effected by fiber spacing for three hybrid composites consisting of carbon/E-glass-epoxy laminates with tight, loose, and dispersed fiber packing [15]. Composites consisted of a row of aligned fibers infiltrated with epoxy, similar to the composite tape geometry used by Fariboz et al. discussed above [14]. By adapting Dilandro et al.'s [19] computational approach to the hybrid composites they were able to predict hybrid composite failure. Dilandro et al. used a statistical model to predict tensile failure for a unidirectional reinforced composite [19]. In the model, fiber segment strengths were represented according to a two parameter Weibull distribution. Stress concentration factors were used to transfer load to neighboring intact fibers when fiber segment strengths were reached. Stress was transferred away from the broken fiber segments within the plane of the break and along the broken fiber through interfacial shear, which is a major improvement compared to the preceding models. Failure was determined when the composite flaw size became unstable and cascading fiber failure was initiated. Jones et al. applied this simulation to hybrid composites consisting of up to nine fibers with controlled fiber spacing [15]. The maximum hybrid effect seen in this study was a 91.6% increase in hybrid failure strain compared to the carbon fiber composite and was achieved for the dispersed laminate case where fiber breaks had little effect on neighboring fibers. For the tightly packed fibers a lower hybrid effect was observed with a 30% increase in hybrid failure strain compared to the carbon-epoxy composite. Based on the results of this work, fiber spacing is critical in the effectiveness of hybrid composites with evenly dispersed HE and LE fibers having the highest hybrid failure strain.

Intermingled and interlaminated continuous fiber reinforced hybrid composites were the focus of Fukuda's statistical model [12]. This was the first study to predict interlaminated hybrid behavior

using statistical and Monte Carlo methods. Analogous to previous researchers, the hybrid composite was represented by short bundles of LE and HE fiber with failure strain cumulative distribution functions characterized by a Weibull distribution. A shear-lag analysis was used to solve for stress concentration factors within the hybrid composite for various fiber breaking scenarios. Concurrently, a Monte Carlo approach was used in this model to allow for bundle failures to occur. The predicted hybrid behavior resulted in a saw tooth failure/reloading pattern. Although, Fukuda's interlaminated hybrid model is similar to one we are seeking to develop, it is for linear elastic composites with unidirectional fiber reinforcements. In the current study the continuous MMC exhibits plastic deformation in uniaxial tension, Figure 14 (b), and the discontinuous composite layer consists of randomly oriented fiber reinforcements making Fukuda's approach over simplified for the current problem.

Multiple researchers have developed models to predicting the behavior of unidirectional reinforced low and high elongation hybrid composites. All of the models were developed for linear elastic unidirectional fiber reinforced hybrid components typically consisting of carbon/epoxy and glass/epoxy composites. When the hybrid geometry was complex, consisting of fabric reinforcements, assumptions were made to simplify the composite to sections of unidirectional axial and transverse reinforcements. Only two of the models summarized above were applied to interlaminated hybrid composites, leaving the majority only applicable to intermingled hybrids. When statistical and Monte Carlo approaches were used, non-catastrophic hybrid behavior was reasonably predicted including a saw tooth failure while cracks were forming in LE fibers. A positive hybrid effect occurred when the HE components were able to constrain the cracked LE components. The neighbor HE sections absorbed load released from the cracks and allow additional cracks to form in the LE sections. This behavior prolonged ultimate failure increasing the hybrid failure strain and toughness compared to the LE fiber reinforced composite. The goal of this study is to apply a similar continuous LE/HE hybrid approach by creating continuous/discontinuous hybrids to improve the failure strain and toughness of a continuous alumina reinforced aluminum composite.

3 GOAL OF THE PRESENT STUDY

The goal of this work is to characterize and obtain an understanding of the hybrid effect in continuous/discontinuous fiber-reinforced hybrid composites which exhibit a non-catastrophic tensile failure.

Key features are as follows:

- Six hybrid composites will be characterized in uniaxial tension to observe their properties and failure behaviors.
- Characterization of the hybrid constituents will be completed including: continuous fiber cumulative distribution functions and mechanical properties, single reinforced composite properties, and the matrix alloy properties.
- An understanding of the hybrid damage evolution behavior, (cracking) in the continuous layer, during tensile loading will be discussed and evidenced through imaging techniques.
- A study on the effect of fiber damage induced during processing and the consequence on single reinforced composite predictions will be performed.
- A hybrid model capable of predicting progressive failure will be used to allow for cracking, transfer of load within the hybrid components and ultimate failure.
- As an input to the hybrid model, simulations will be used to predict the tensile behavior, including plasticity, of the continuous composite including the cumulative distribution function for strength.
- The hybrid model will be capable of simulating failure for low failure strain layers sandwiched between high failure strain $[HE/LE]_s$ and high failure strain layers between low failure strain layers $[LE/HE]_s$.
- Accuracy of the hybrid model will be assessed by comparison with the experimental results of two continuous/discontinuous metal matrix hybrid composites.

4 HYBRID DESCRIPTIONS AND CONSTITUENT PROPERTIES

4.1 HYBRID GEOMETRY

The hybrid laminates examined in this study consist of continuous alumina fabric and discontinuous randomly oriented alumina fiber reinforcements in an aluminum-2% copper (Al-2Cu) matrix. Six different hybrid laminates were prepared with various ratios of continuous to discontinuous reinforcements. Two types of discontinuous reinforcement layers were used having either a 5% or 15% fiber volume fraction. Table I describes each hybrid's layup, composition ratio, and discontinuous reinforcement type. All hybrids have the same continuous reinforcement: a 27% volume fraction Nextel™ fabric layer. Each hybrid is labeled based upon the percentage and type of discontinuous reinforcement. For example, hybrid 65P is 65% Saffil® paper composite and 35% Nextel™ fabric composite while hybrid 63B consists of 63% Saffil® board and 37% Nextel™ fabric composites.

Hybrid 65P has outer low strain to failure continuous Nextel™ fabric composite layers and inner high strain to failure discontinuous Saffil® paper composite layers with a composition ratio of 65:35 Saffil®:Nextel™ composite by thickness. The 65:35 composition ratio was calculated by determining how much of the overall hybrid thickness consists of the Saffil® and Nextel™ composites. Hybrids 65P and 65P Inverted have equal composition ratios but different lamination schemes. The low failure strain fabric layer is on the outside of hybrid 65P and on the inside in hybrid 65P Inverted. 65P Inverted is the only hybrid with an outer discontinuous layer. Hybrid 63B was chosen to explore the effects of using a stiffer and stronger discontinuous layer while maintaining a similar composition ratio. To achieve this, the discontinuous layer used in hybrid 63B consists of the 15% volume fraction Saffil® board layer while hybrids 65P and 65P Inverted have the 5% Saffil® paper layer. Finally, the objective of hybrids 48P, 87B, and 54B was to determine the effect composition ratio has on hybrid properties. For these hybrids the composition ratios are 48:52, 87:13, and 54:46.

Table I. Saffil® paper reinforced hybrid composite descriptions.

Label	**65P**	**65P Inverted**	**48P**
Lamination Schematic	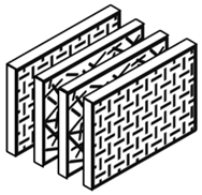	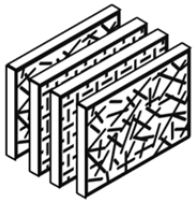	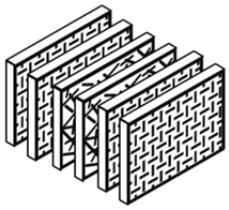
Saffil® Type	5% Paper	5% Paper	5% Paper
Saffil®:Nextel™	65:35	65:35	48:52
Layup	$[N/P]_s$	$[P/N]_s$	$[N_2/P]_s$

Table II. Saffil® board reinforced hybrid composite descriptions.

Label	**87B**	**63B**	**54B**
Lamination Schematic	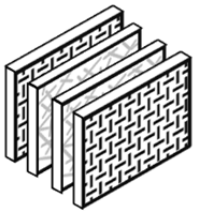	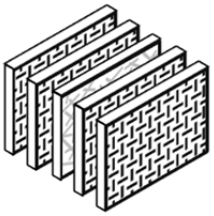	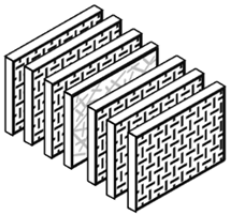
Saffil® Type	15% Board	15% Board	15% Board
Saffil®:Nextel™	87:13	63:37	54:46
Layup	$[N/B]_s$	$[N_2/B/N_2]$	$[N_3/B/N_3]$

4.2 Composite Uniaxial Tension Test Method

To characterize the tensile behavior and properties of the MMCs and neat matrix alloy quasi-static tensile testing was performed. All hybrid and single reinforced MMCs were manufactured by CPS Technologies in Worchester, MA. Reinforcement layers were stacked in a mold and infiltrated with liquid aluminum (Al-2Cu), under pressure. Composite panels were cut into 10

mm wide and 189 mm long rectangular samples. The tensile samples were sectioned from the MMC panel using a diamond blade saw and polished until the sides were reflective. This process ensured sample edges were smooth and no damage from machining was visible reducing the likelihood of stress concentrations, premature failures and inaccurate strengths as a result of the cutting process. Approximately 50 mm of each sample end was gripped in the load frame for a total of 100 mm gripped, leaving an 89 mm gauge length, within agreement of the ASTM D 3552 standard for tensile testing of metal matrix composites [20]. An MTS servohydraulic load frame was used to apply strain to the rectangular tension samples at a rate of 0.001 s^{-1} consistent with the ASTM D 3552 standard for tensile testing of metal matrix composites [20]. Alignment of the load frame was within ASTM E1012 specifications [21]. To be specific, the standard states a rectangular sample strained to 500 microstrain must have a maximum bending strain less than 10%. Additionally, gripping of the sample can apply no more than 50 microstrain at zero applied load. Alignment of the load frame was accomplished using a 6.35 mm thick, 76.2 mm wide, and 203 mm long aluminum sample instrumented with six pairs of strain gages. A pair of gages refers to aligned gages on both sides of the sample. Bending strains are calculated and monitored from all 12 gages while the MTS alignment fixture is adjusted to align the grips. A detailed explanation on how to prepare an alignment sample and calculate bending strains can be found in the ASTM E1012 standard [21]. In agreement with the standard, the load frame was aligned to a maximum bending strain of 4% at 500 microstrain and gripping resulted in 20 microstrains at zero load. Aluminum sheeting with a 0.51 mm thickness was wrapped around the grip sections of each sample to help prevent grip failures from debris or rough grip surfaces, as shown in Figure 6. Grip line pressures between 6 MPa - 14 MPa were applied to the samples. These grip line pressures equal a nominal applied grip pressure of 102 MPa - 255 MPa on the sample surface. After each tension test, grip sections were inspected to ensure no damage was done to the sample due to gripping. If deformation in the grip section was observed the grip pressure was reduced for the remaining samples. Strain gages and a digital image correlation system (DIC) were used to measure strains during loading. Figure 7 shows the instrumented test setup for a failed composite sample with the DIC system and strain gage. An Aramis digital image correlation system was used to capture images of the speckled sample surface at 12 frames per second. The Aramis software uses a proprietary algorithm to calculate two dimensional strain fields for the sample surface by tracking three dimensional speckle deformations. Strain gages

from Vishay Precision Group style CEA-13-125UW-350 were used with M-Bond AE-10 for the adhesive.

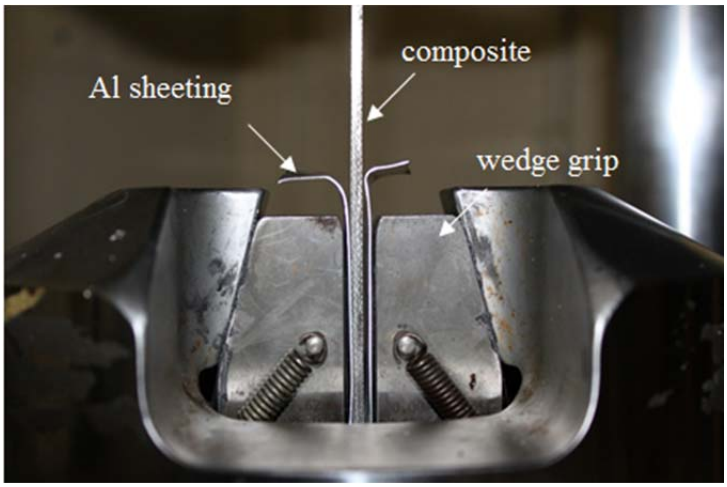

Figure 6. Uniaxial composite tension test setup profile before applying grip pressure.

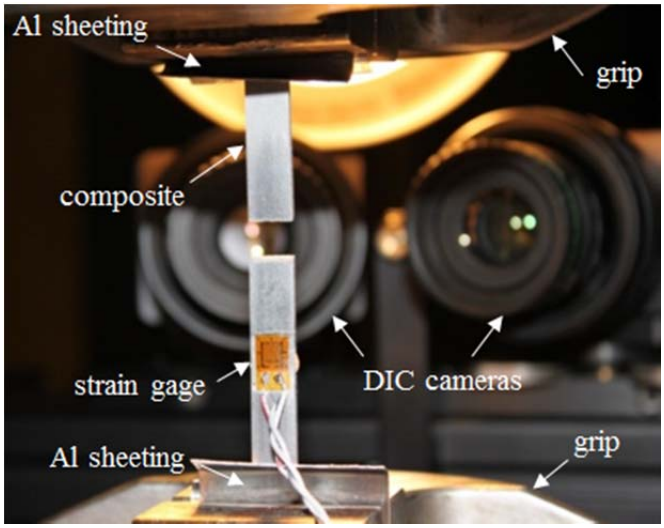

Figure 7. Uniaxial composite tension test setup.

4.4 Property Calculations

Stress Strain Curves

All axial stress-axial strain curves reported in Sections 4.5 and 5.1 were calculated using the MTS 407 load and stroke data. Where stress σ, equals the load P, divided by the cross sectional area A. Strain ε, is equal to the change in stroke divided by the sample gauge length, L. The load and stroke stress strain curves were only used to represent composite behavior in the axial stress-axial strain curves. All reported properties were calculated from the more accurate strain gage and DIC measurement methods which are representative of the overall composite strain before cracking where the properties are calculated.

Strength

Reported strength values are equal to the maximum load carried by the sample during tensile loading divided by the sample cross sectional area.

Modulus

Modulus is the slope of the straight portion of stress strain curve before yielding. A linear regression was used to calculate the slope. Load values were recorded from the MTS 407 controller. High resolution gage data was used for the modulus calculation.

Failure Strain

Failure strains were calculated from the digital image correlation system strain measurements. The DIC system can track strains until the speckle pattern cracks or moves out of the frame of the cameras. For this application the DIC was able to capture strain measurements during the entire tensile loading of the samples. Failure strains are equal to the strain in the sample at failure or zero load. The two dimensional axial strain field output by the DIC software is averaged over all strain points at each time increment to obtain the axial stress-axial strain curve.

Cracking Strain

The cracking strain is reported for each hybrid sample and is equal to the strain at the peak load. DIC strain measurements were used for this calculation.

Yield Stress

Composite yield stress is equal to the stress at which the initial portion of the stress strain curve is no longer straight. The limit of the straight portion is decided by checking the r-squared value of the linear regression and requiring it to be greater than 0.96. The aluminum-2% copper matrix alloy yield stress was calculated using the 0.2% offset strain method.

Poisson's Ratio

The axial and transverse strain fields from the DIC system were used to calculate Poisson's ratio for the composite materials, $= -{\varepsilon_{transverse}}/{\varepsilon_{axial}}$.

Density and Volume Fraction

A density kit with 2-propanol as the auxiliary liquid was used to determine density. Fiber volume fraction, V_f of the composite laminates was calculated using a rule-of-mixtures approach. $\rho_c = V_f\rho_f + (1 - V_f)\rho_m$ where ρ is the density. In this calculation, it is assumed that there are no voids present in the composite.

Modulus of Toughness

The area under the stress strain curve to failure is reported as the modulus of toughness. The modulus of toughness is a measure of the amount of energy stored in a material due to its deformation per unit volume. A trapezoidal rule was implemented to calculate the area under the stress strain curve for the uniaxial tension tests.

4.5 Single Reinforcement Composites & Behaviors

Continuous Fabric Composite

As discussed previously, the hybrid composites in this study consist of laminated continuous and discontinuous fiber reinforced layers in an aluminum-2% copper (Al-2Cu) matrix. The continuous fabric composite reinforcement is a woven alumina Nextel™ 610 3,000 denier fiber in an eight-harness satin weave geometry (Nextel™ DF-19 fabric) and has a composite fiber volume fraction of 27%, Figure 8. This weave geometry results in roughly half of the fiber reinforcement aligned in the axial and transverse directions. Nextel™ 610 fiber is a continuous filament ceramic oxide fiber available through 3M™ [22]. The fiber has a refined crystal structure of >99% α-Al_2O_3 with no glassy phases and a density of 3.9 g/cm^3. The continuous fiber comes in tow deniers of 1,500, 3,000, and 10,000 grams per 9,000 meters. Nextel™ 610 fiber is available in a variety of geometries including tows, woven fabric, tape, thread, chopped fiber, mat, and nonwoven paper. The interest of this study is the woven fabric and aligned tow used to make unidirectional composite. A scanning electron microscope image of the polished fabric MMC can be seen in Figure 50. As evidenced in the image, the fabric composite consists of axial reinforcement, transverse reinforcement, and matrix rich regions. To support fabric composite strength predictions, discussed in detail in Section 7.5, the uniaxial, transverse, and neat Al-2Cu matrix properties and behaviors were also characterized will be reported. The unidirectional (0°) and transverse (90°) composites tested are reinforced with Nextel™ 610 10,000 denier fiber tows and have a fiber volume fraction of 59% and 57%.

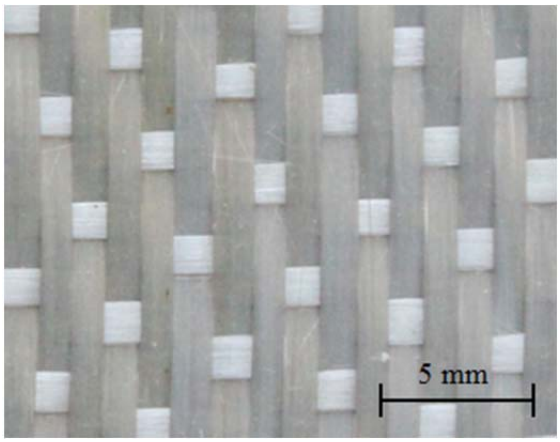

Figure 8. 8-harness satin weave Nextel™ fabric desized.

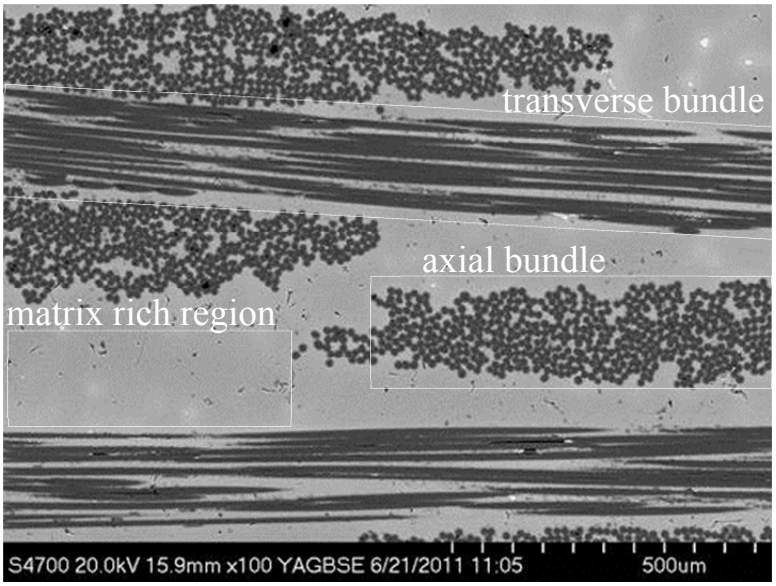

Figure 9. Fabric composite cross section consisting of axial and transverse continuous fiber reinforced sections as well as matrix rich regions [23].

DISCONTINUOUS COMPOSITES

The discontinuous composite consists of either Saffil® paper or Saffil® board which are composed of short randomly oriented alumina Saffil® fiber with 5% and 15% volume fractions. Similar to Nextel™, the Saffil® fiber is also made from alumina however, it has a different crystalline structure of approximately 97% δ-Al_2O_3 and 3% silica and a higher density at 3.3 g/cm^3 [24]. Saffil® fiber is available through SAFFIL® Ltd. in short fiber mat preforms with various degrees of packing density, which controls composite fiber volume fraction. The fibers have an average diameter of 3 μm and are approximately 500 μm long [25]. An image of a polished cross section of the 5% Saffil® paper composite can be found in Figure 10. The bright regions in the cross section are an eutectic θ-$CuAl_2$ phase, grey represents the Al-2Cu matrix region and the darker grey sections are Saffil® fiber.

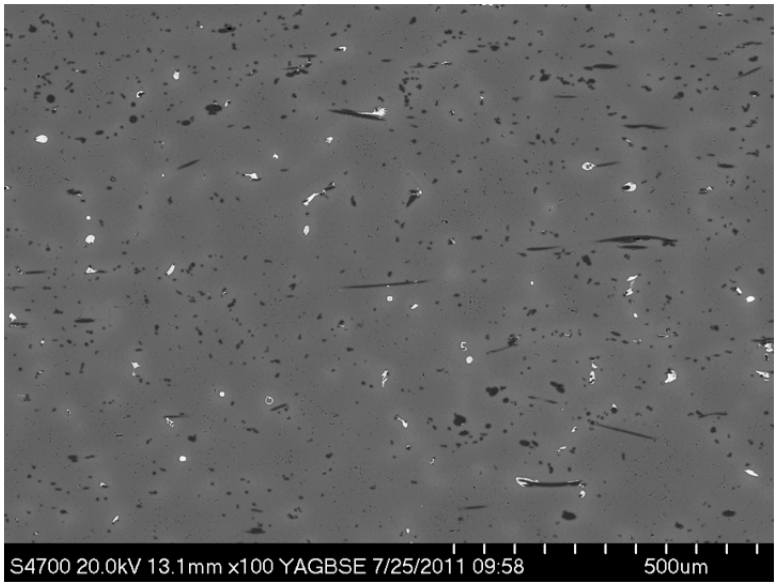

Figure 10. Saffil® reinforced Al-2Cu with a 5% fiber volume fraction [23].

UNIAXIAL TENSION BEHAVIOR

Typical axial stress-axial strain curves for composites with one type of fiber reinforced can be found in Figure 11. As evidenced in the tensile behavior, the Nextel™ fabric layer has high stiffness and strength but a low failure strain. The Saffil® paper composite has the highest elongation along with the lowest strength and stiffness. Mixed properties were measured for the Saffil® board layer having a lower elongation, higher stiffness, higher yield stress, and higher strength than those for the Saffil® paper. The Saffil® paper layer was chosen to be one of the discontinuous reinforcements due to its high strain to failure. Our goal is to create a fabric/Saffil® hybrid composite with a similar strength and stiffness, an improved failure strain, and an increased modulus of toughness compared to the fabric composite alone. Due to the low yield stress and strength of the paper composite, it was possible that the hybrid would exhibit a lowered stiffness and strength than the fabric composite as well as a low yield stress. For these reasons, a second type of hybrid composite was designed using Saffil® board as the discontinuous layer. The Saffil® board composite has more similarities to the behavior of the fabric composite, however, it does not exhibit the high failure strain like Saffil® paper.

Table III lists the measured single reinforced composite properties described in Section 4.3. Properties for the neat matrix as well as the unidirectional and transverse continuous composites are included in Table III since they will be used to validate the continuous strength model discussed in Section 7, refer back to Figure 9 to view the fabric cross section. Stress strain curves for the three continuously reinforced laminates are plotted together in Figure 12. The fabric composite consists of roughly 15% unidirectional reinforcement and 15% transverse reinforcement which is why the fabric composite strength is significantly lower than the unidirectional composite strength. The ductile axial stress-axial strain behavior of the aluminum-2% copper matrix can be found in Figure 13. With a 12.5% strain to failure the matrix material has the highest strain to failure nearly doubling the Saffil® paper failure strain and the highest modulus of toughness or area under the axial stress-axial strain curve of all the materials tested in this work of 12.7 MPa·mm/mm.

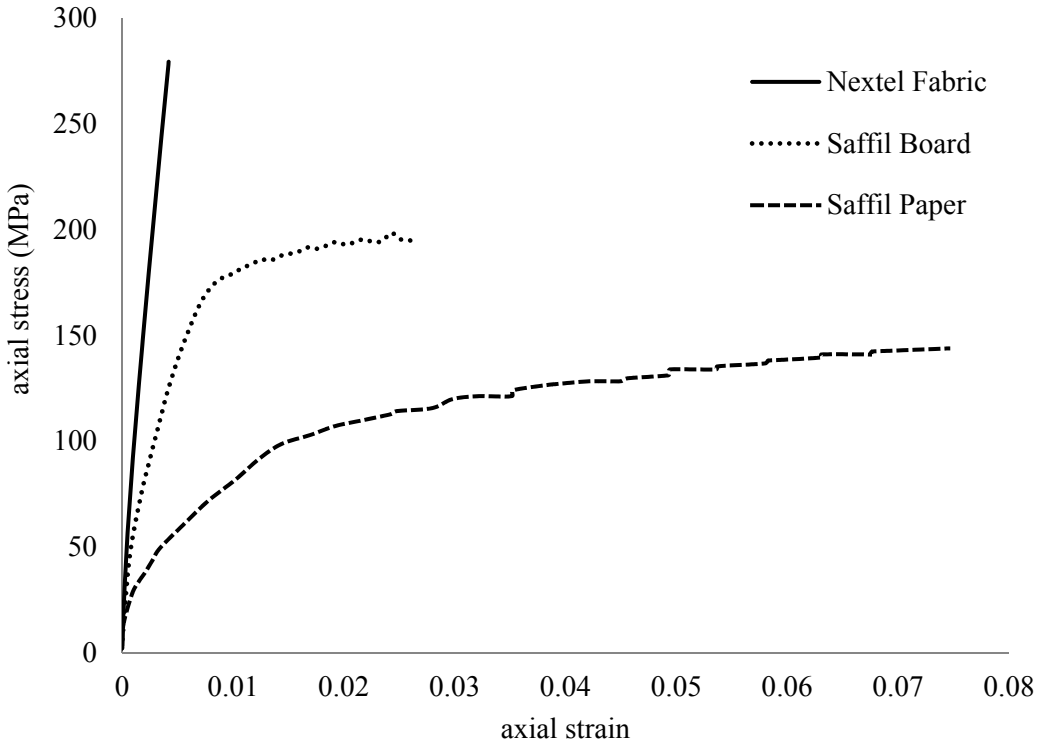

Figure 11. Single reinforcement composite tensile behavior to failure.

Table III. Single reinforcement composites and neat aluminum properties.†

Composite	**Strength (MPa)**	**Modulus (GPa)**	**Failure Strain (%)**	**Yield Stress (MPa)**	**Poisson's Ratio**	**Density $\left(\frac{g}{mm^3}\right)$**	**Modulus of Toughness $\left(MPa \cdot \frac{mm}{mm}\right)$**	**Volume Fraction (%)**	**Thickness (mm)**	**Population Size**
Nextel™ Fabric	270	125	0.42	50	0.23	2.99	0.64	22	2.49	5
Saffil® Paper	150	84	7.49	10	0.18	2.76	9.85	3	3.12	11
Saffil® Board	200	83	1.91	30	0.27	2.85	4.10	17	3.29	5
Al-2Cu* *no reinforcement	120	71	12.47	40	0.30	2.73	12.74	0	2.90	10
Nextel™ Unidirectional	1280	235	0.55	-	0.29	3.40	3.83	59	1.84	15
Nextel™ Transverse	190	140	0.30	110	0.18	3.38	0.34	57	1.53	14

† Standard deviations for each of the properties listed in Table III can be found in Appendix A.

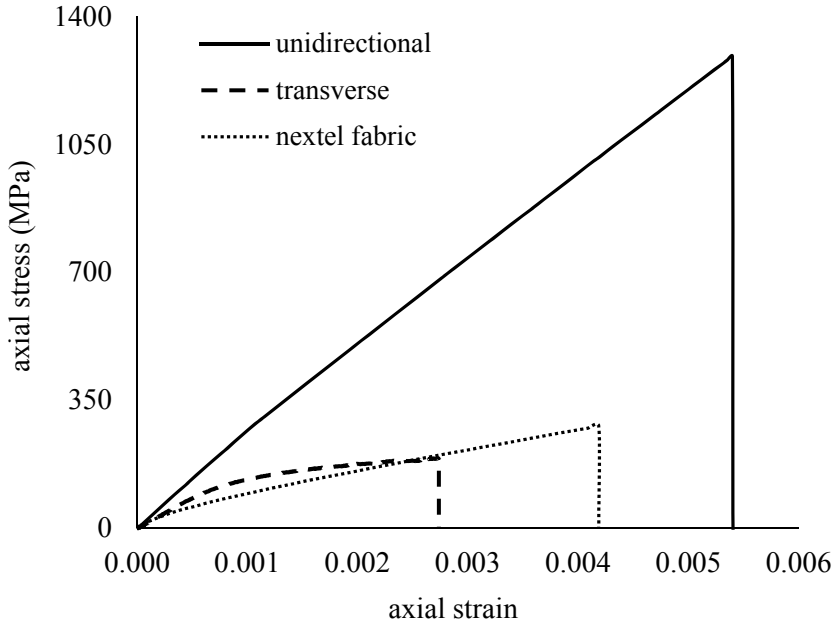

Figure 12. Nextel™ unidirectional (0°), transverse (90°) and woven fabric (0°/90°) continuous fiber reinforced composites.

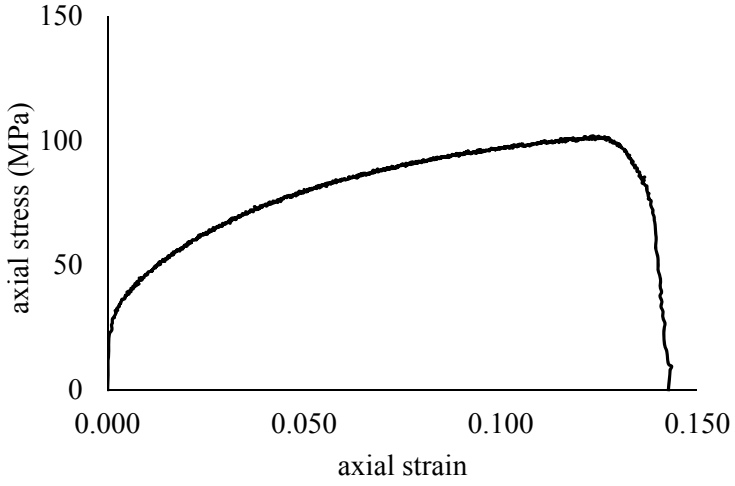

Figure 13. Aluminum-2% copper matrix uniaxial tension stress strain curve.

Figures 14-16 consist of the fabric, paper, and board lamination schemes (a), axial stress-axial strain behaviors (b) with labeled points on the curve corresponding to the digital image correlation axial strain fields at the point displayed in section (c). The last row in each figure, sections (d) and (e), contain photographs of typical failed sample surfaces from the side and front view. The images were taken of a failed sample, which typically failed near the middle of the gage length. This is also where the imaging equipment or strain gage was applied leaving traces of glue, gage parts, and spray paint on the sample surfaces. The side view (d) can provide a perspective on the thickness and number of the continuous and discontinuous layers in each composite. For example, the fabric composite consists of four layers of Nextel™ fabric visible in the side view of Figure 14 (d). Only a small portion of the entire sample's length is shown to improve visibility of the fracture behavior, the full length of these samples is 190 mm. The purpose of these figures is to compare strains in each composite at similar places on their axial stress-axial strain curves as well as viewing their macroscopic failure behavior.

AXIAL STRAIN FIELDS

The first digital image correlation strain field (I) is to show the uniform strain field before initial yielding of the sample occurs. The middle strain field, if it is present, is at yielding. The last strain field is taken at the strength of the sample. To calculate the axial stress-axial strain curve each axial strain field is averaged. The color bar, below each set of DIC images, describes the strain contour limits. The Nextel™ fabric sample right before failure shows regions of high strain concentrations in red with approximately 0.75% strain at those locations. When banded strain concentrations are seen they usually indicate a high potential for crack initiation or existing micro crack formation on the surface of the sample. The Saffil® paper and board samples have large regions of high strains indicating necking regions of the sample. The location of the DIC system and the strain field measured is random. For some tests, shown in the following section, failures can be captured and the growth and coalescence of crack formation on the sample surface is visible. The rubber bands in the Saffil® paper image (Figure 15 c. III) are from an extensometer. Initially, tests were performed with an extensometer, strain gage, and DIC to measure strain and to determine the most accurate method for these materials. The strain gage

and DIC stress strain curves were almost identical up to failure of the gage adhesive while the extensometer always measured significantly lower strains than the other two devices.

FAILURE PROFILES

The profile images for each sample provide a check on the lamination scheme. For example, in the Saffil® paper sample, starting at the top of the image and working down, there is a matrix rich layer followed by a paper layer, matrix rich, two paper layers (twice as thick as the initial dark grey region), and finally another matrix rich region. Also visible in this image is the severe amount of ductile deformation (yielding) in the Saffil® paper sample near (left of) the failure location. Both the paper and board composites failed in shear evidenced by the 45° angle of their fracture plane. The fabric composite failed almost straight across, which is better seen in the front failure view (e). The surfaces of each of these samples had one catastrophic crack propagate through the sample, which also corresponded to the failure surface.

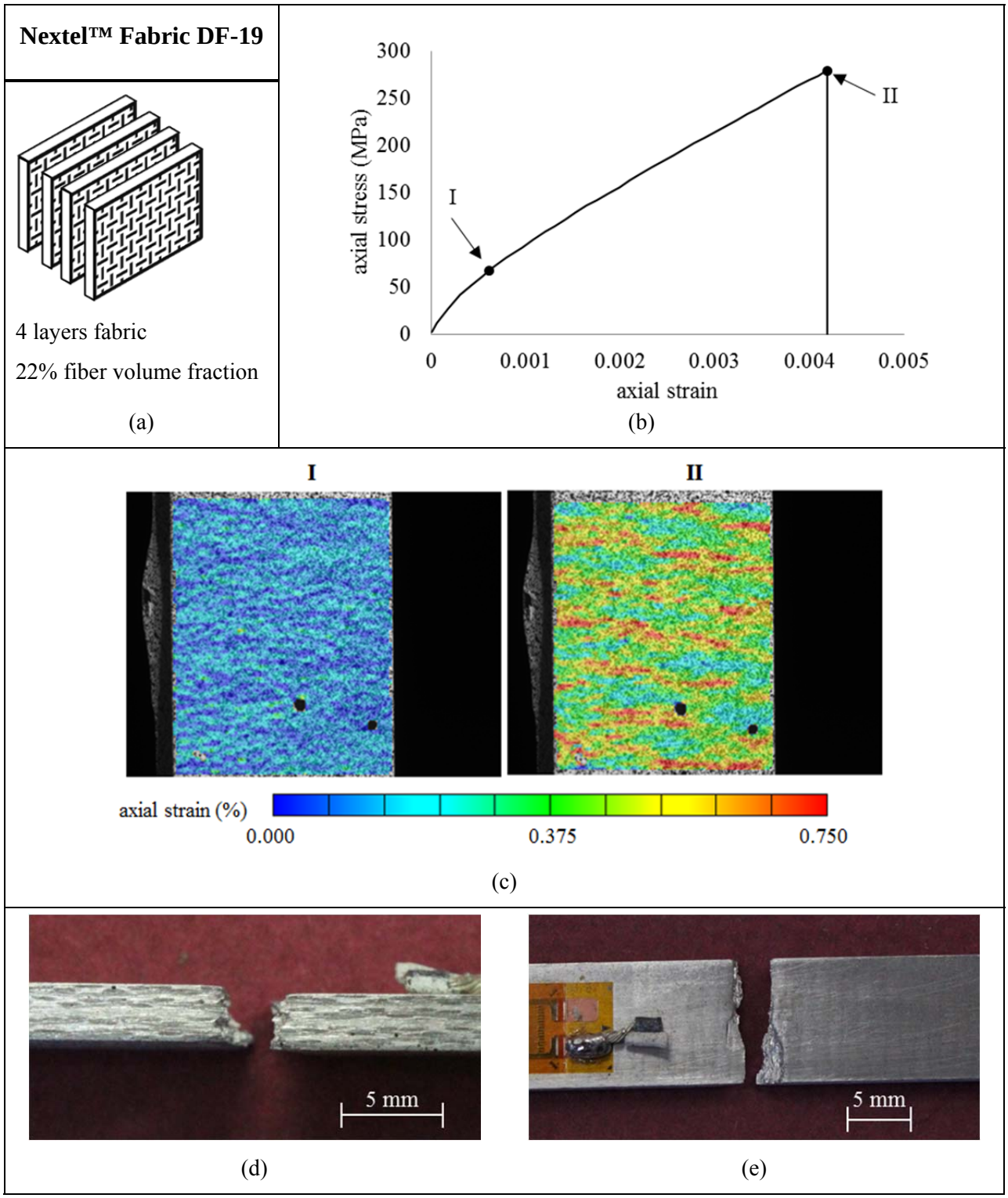

Figure 14. Nextel™ fabric composite: (a) layup schematic, (b) typical uniaxial tension stress strain curve with labeled regions (I) and (II) corresponding to the DIC axial strain contours in (c). Failed sample side (d) and top (e) profiles.

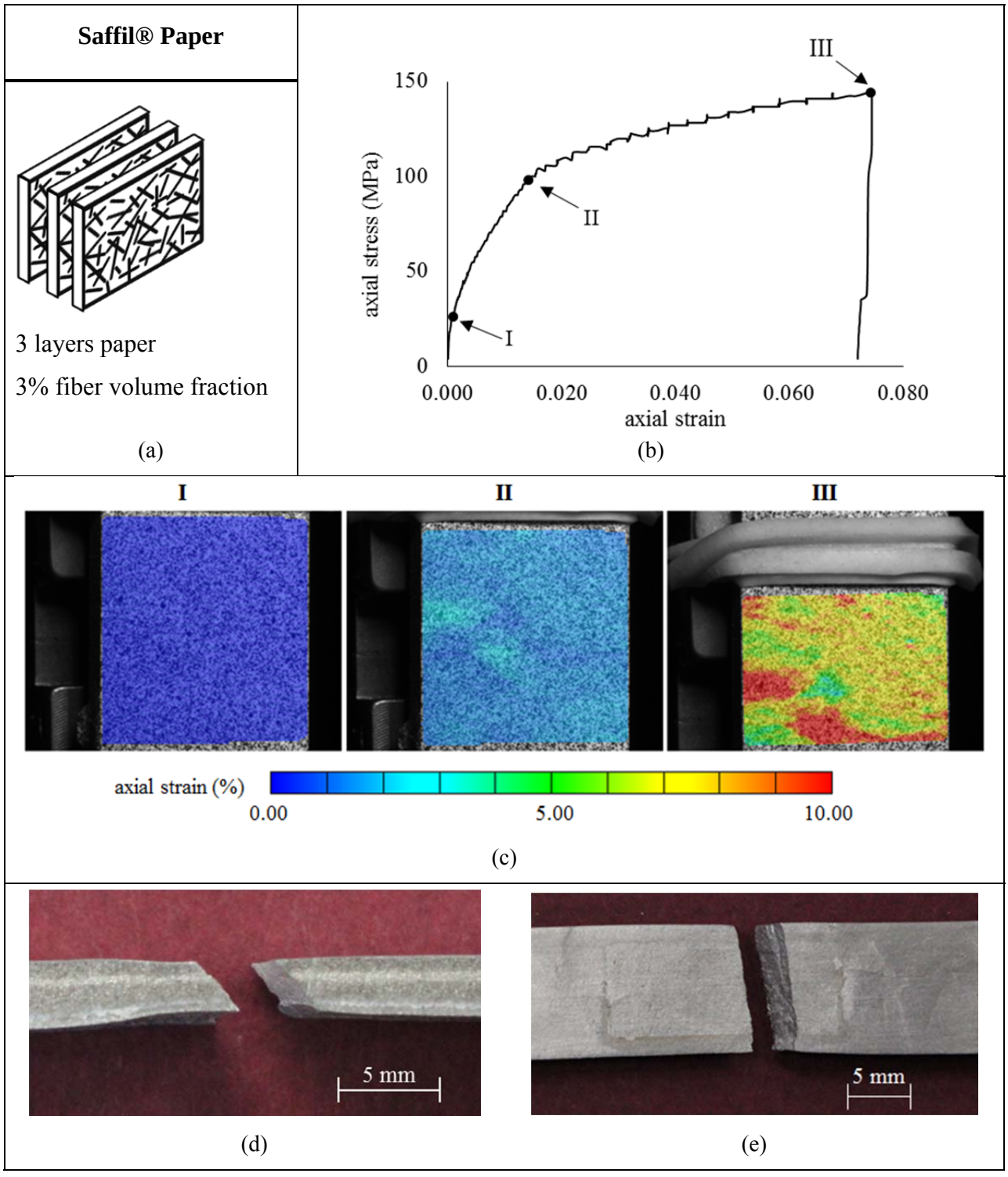

Figure 15. Saffil® paper composite: (a) layup schematic, (b) typical uniaxial tension stress strain curve with labeled regions (I), (II), and (III) corresponding to the DIC axial strain contours in (c). Failed sample side (d) and top (e) profiles.

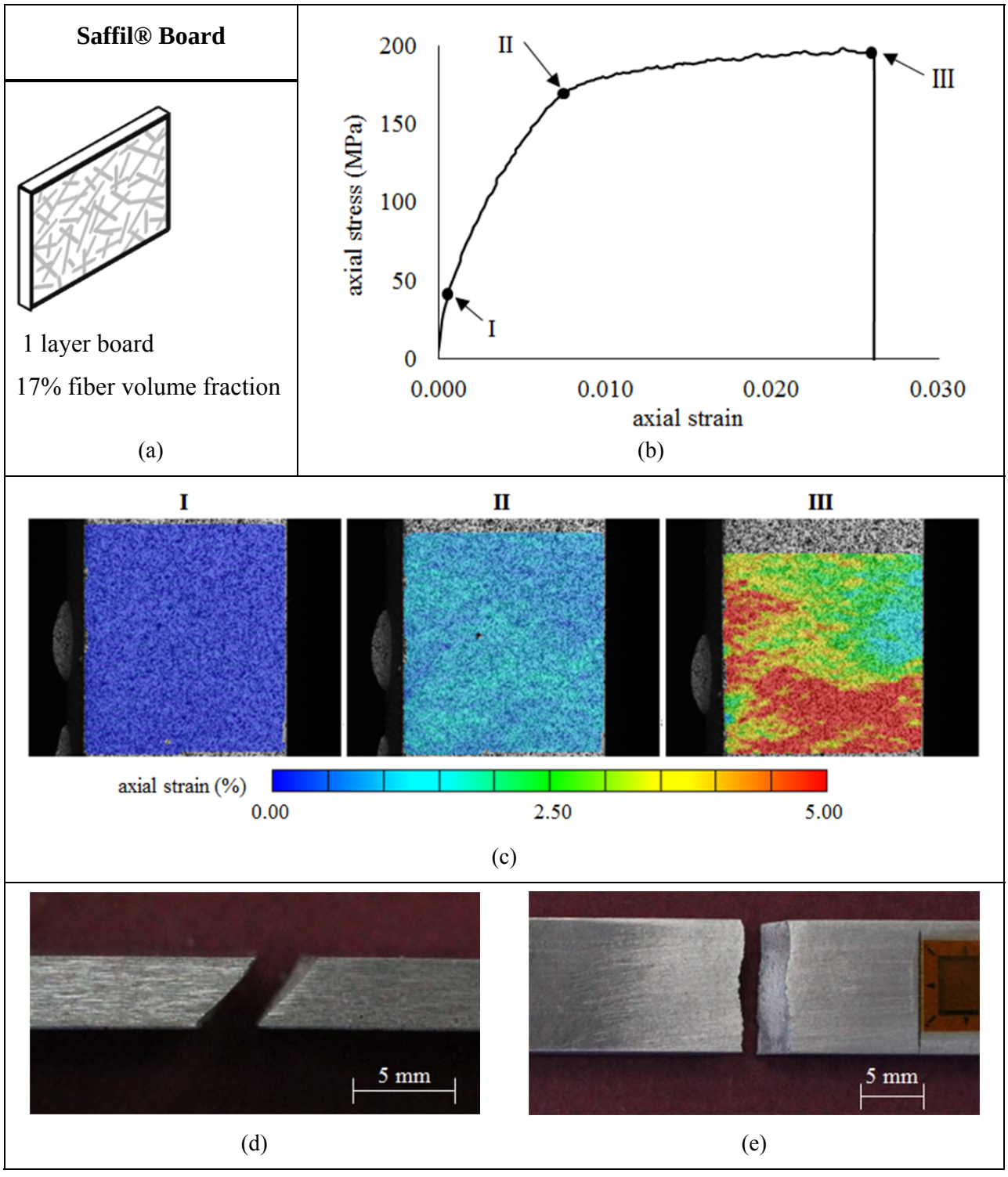

Figure 16. Saffil® board composite: (a) layup schematic, (b) typical uniaxial tension stress strain curve with labeled regions (I), (II), and (III) corresponding to the DIC axial strain contours in (c). Failed sample side (d) and top (e) profiles (d).

5 HYBRID COMPOSITE BEHAVIOR

The six hybrid composites, discussed in Section 4.1 were tested in uniaxial tension using the method described in Section 4.2. Axial stress-axial strain curves of all hybrids will be compared first, followed by each hybrid's failure behavior including their strain contours and failure surfaces. Then, average mechanical properties for each hybrid will be tabulated along with a comparison of their properties. Each curve presented was chosen by the author to represent the average behavior of the samples tested for each composite type. These representative curves have properties closest to the average of all samples tested from the panel and exhibit similar failure behaviors. Axial stress-axial strain plots for each sample from the panel are presented in Appendix B, Section 11.2. Hybrid composite failure behavior was non-catastrophic consisting of an initial failure, reloading, a number of additional failure and reloading segments, followed by elongation leading to ultimate failure. A few of the hybrids have a gradual unloading behavior (65P and 65P Inverted) while others display similar initial loading properties as the fabric composite (48P and 63B). Hybrid 87B showed no improvements in properties with a behavior closely following the Saffil® board composite behavior and a decreased failure strain. As discussed below, the "ideal" hybrid would combine the improved initial loading behaviors of 48P and 63B with the gradual failure of 65P and 65P Inverted.

5.1 UNIAXIAL TENSION AXIAL STRESS-AXIAL STRAIN BEHAVIOR

To compare hybrid behavior with their single reinforced composite layers (fabric, paper, and board composites) each discontinuous reinforcement type will be plotted separately in Figures 17-19. Looking at the behavior of paper reinforced hybrids, it is difficult to discern hybrid characteristics due to the high failure strain of the paper composite, Figure 17. Figure 18 magnifies the hybrid behaviors by prematurely cropping the plot before the paper failure strain. As indicated in the image the paper composite failure slowly increases in stress to a failure strain of 0.075.

Laminates 65P and 65P inverted were made to investigate the effect of having the continuous fabric layer on the outside or inside of the layup. 65P Inverted is carrying a higher stress at strains before the peak of the axial stress-axial strain curve than 65P after yielding. Although these composites were designed to have the same reinforcements it is difficult to replicate the manufacturing process. 65P Inverted has a smaller composite thickness than 65P however both have the same amount and thickness of reinforcements. This indicates less aluminum in composite 65P Inverted and therefore a higher fiber volume fraction resulting in the differences in behaviors. Samples from the 65P panel consistently showed multiple loading/unloading steps in the failure behavior while 65P Inverted typically had one drop in load at cracking (maximum load) followed by a gradual convex unloading curve. After multiple cracks, 65P had a concave failure behavior reaching failure strains 33% higher than 65P Inverted. During testing, hybrid 65P had visible cracks propagating through the outer fabric layers resulting in a decrease in load of about 10%. The initial crack was followed by either one or two more loading and unloading curves. Failure behavior of hybrid 65P provides the most information on how the hybrids are responding to loading due to the visible damage. The cracked hybrid 65P carried load for an additional 0.65% strain until the Saffil® layer failed resulting in ultimate failure of the composite. 65P Inverted was expected to have an improved hybrid effect since the inner cracking fabric layers were bridged with the Saffil® layers constraining the crack and delaying fracture. This opinion came from the reported unidirectional hybrid behavior, Section 2, with inner low failure strain layers. The opposite is seen in these experimental results with 65P reaching higher failure strains and maintaining higher loads during failure than 65P Inverted. All hybrids other than 65P Inverted consist of outer fabric layers.

The purpose of hybrid 48P was to look at the effect of reinforcement ratio. Hybrid laminates 65P and 65P Inverted have a similar discontinuous/continuous reinforcement ratio of 65% while 48P consists of more fabric reinforcement. As a result 48P has a significantly higher strength than the other paper hybrids. The cracking strain (strain at maximum load) for 48P is higher than the failure strain of the fabric composite by 24%. Another positive quality of 48P is the similar strength and stiffness in the initial loading portion of the curve as those of the fabric composite. After the onset of plasticity, 48P is reaching higher strains than the fabric composite at similar

loads. The increase in hybrid cracking strain and similar hybrid stress levels as those of the continuous fabric composite follows the behavior reported in the literature review, Section 2, for continuous low failure strain/high failure strain hybrids [5]. Unlike in the literature review (Figure 3), where during cracking the axial stress is constant, in these hybrids after cracking there is a 65% drop in load carried by the sample. The unidirectional hybrids in the literature sustained a high load level for significant strains before ultimate failure, similar to hybrids 65P and 65P Inverted.

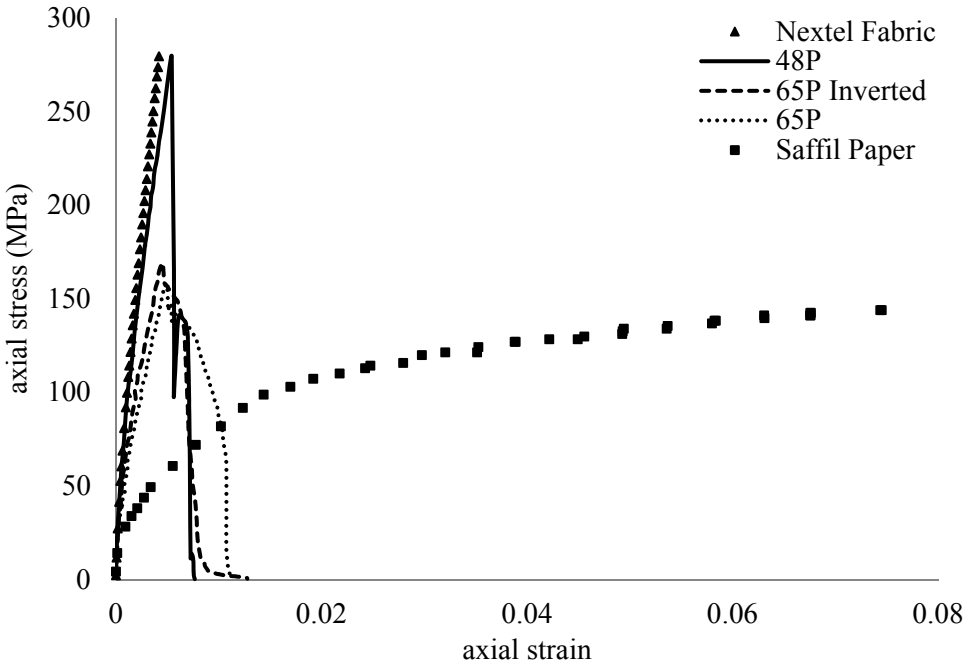

Figure 17. Saffil® paper hybrid composites and single reinforcement laminates (Nextel™ fabric and Saffil® paper).

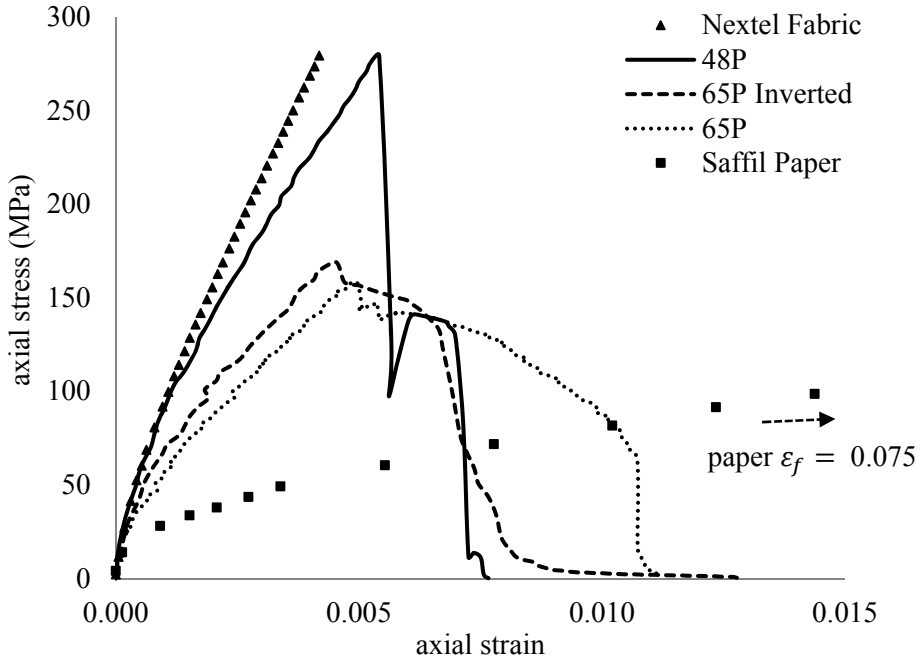

Figure 18. Magnified plot for the Saffil® paper hybrid composites. (Saffil® paper composite curve not plotted to failure.)

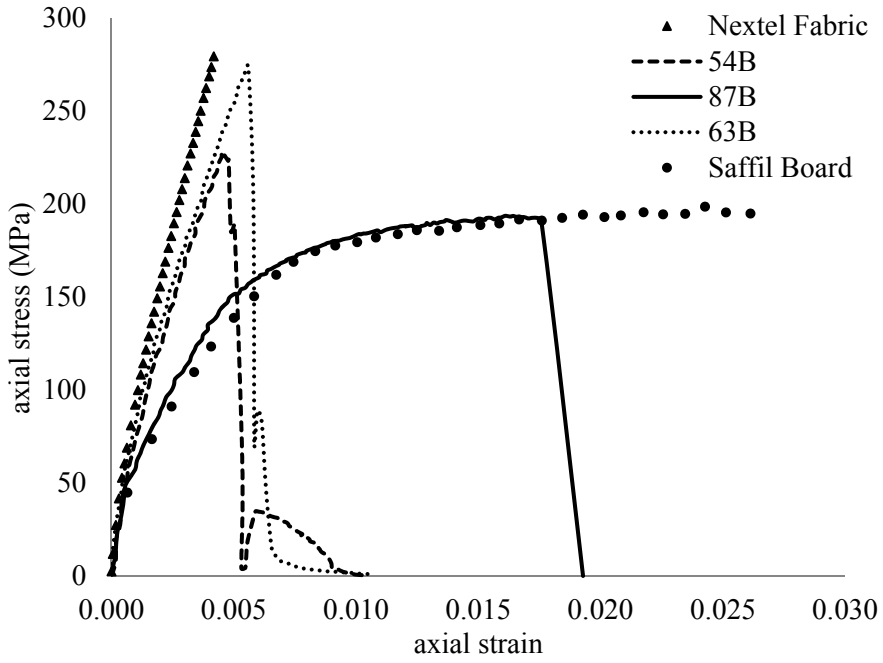

Figure 19. Saffil® board hybrid composite axial stress-axial strain behavior.

The next hybrid variable investigated was the use of a stiffer and stronger discontinuous layer, Saffil® board. Axial stress-axial strain curves for three hybrid composites with Saffil® board discontinuous reinforcement layers are shown in Figure 19. Hybrid 87B failed to have any positive hybrid behavior exhibiting a lower strain to failure than the Saffil® board layer and having no increase in stiffness or strength. 63B has the most improved hybrid behavior for this group with a cracking strain higher than the fabric composite failure strain. After cracking, there is a 75% decrease in load and a small reloading curve followed by ultimate failure. Similar failure behavior was observed for 54B however the strength of this hybrid is much lower than the fabric composite with a slightly higher failure strain than 63B.

A comparison of hybrid behaviors with similar reinforcement ratios (63B, 65P, 65P Inverted) are plotted in Figure 20. Although these three hybrids have similar discontinuous to continuous reinforcement ratios, by thickness, the Saffil® board layer has a higher volume fraction of 15% compared to the Saffil® paper layer at 5%. These three composites display drastically different behaviors although all three have positive hybrid effects. To obtain a better understanding of the effect of the Saffil® board vs. Saffil® paper layer, hybrids exhibiting a large drop in load after cracking are shown in Figure 21. Hybrid 48P and 63B have similar behaviors up to cracking. During failure 48P has a more gradual unloading behavior, sustaining stresses of 140 MPa for approximately 0.001 strain while 63B has one reloading curve followed by a steep unloading curve to ultimate failure. 54B also has some gradual unloading behavior with a 20% lower strength. The Saffil® board hybrids had a more unstable cracking behavior with large drops in loads and few reloading curves reaching lower failure strains than the Saffil® paper hybrids.

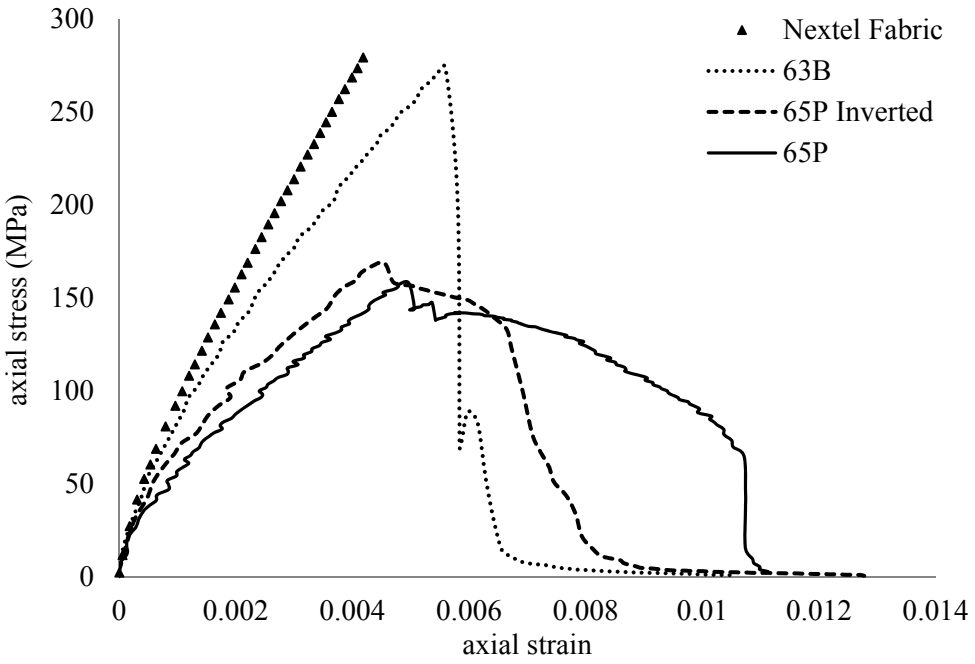

Figure 20. Hybrid composite uniaxial tension behavior consisting of approximately 65% discontinuous reinforcement by thickness.

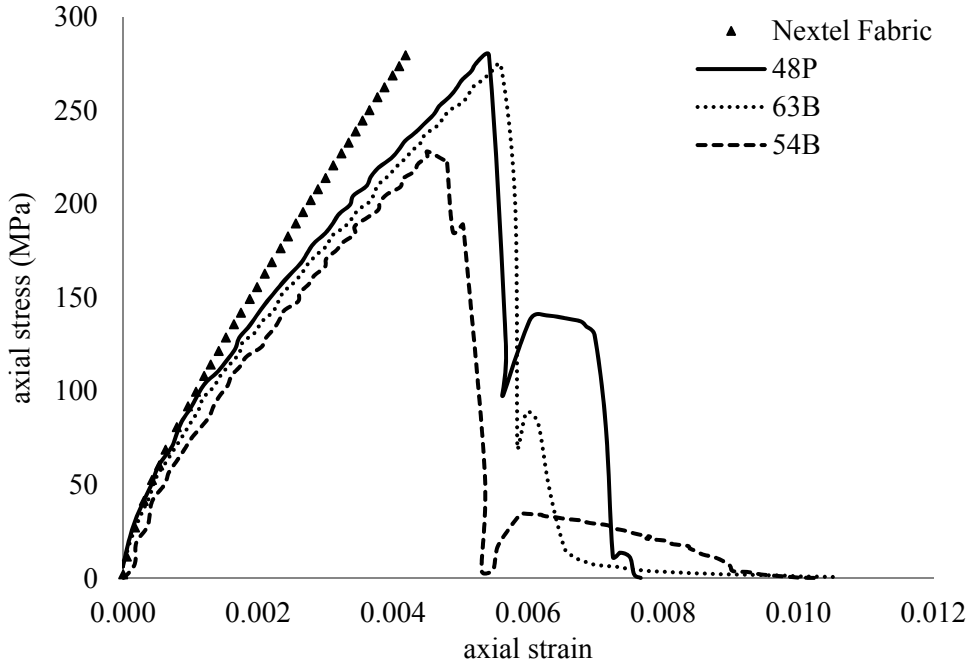

Figure 21. Hybrid composite uniaxial tension behavior exhibiting large drops in load after initial cracking.

The behavior seen from the hybrid laminates is complex including multiple loading/unloading portions of the stress strain curves, some improved cracking strains while maintaining high strengths and stiffness of the fabric composite failure strain, and failure strains up to three times higher than the fabric composite. These observations are based on average behaviors of each hybrid, now differences in failure profiles and strain fields will be discussed to gain knowledge on how the failure process occurred for each hybrid. Figures 22 through 27 each consist of multiple images including: hybrid lamination schemes (a), stress-strain behaviors (b) with labeled places on the curve corresponding to the digital image correlation axial strain fields at the point displayed in section (c). The last row in each figure, sections (d) and (e), contain photographs of typical failed sample surfaces from the side and front view.

As discussed previously, cracks were visible on the surface of hybrid 65P samples during failure. Observing the strain fields at critical points in the stress strain behavior support the idea that after a crack propagated through the fabric layer the load dropped by 10%. The DIC images in Figure 22 (c) clearly show no cracks at the peak load (I). After the load drop and at the beginning of reloading a crack was captured in the DIC images (II). The crack fully propagated through the fabric layer shown in (II) in red. At the onset of the final unloading, III, the crack has opened further causing the DIC to be unable to track strains across the surface since the speckle pattern was destroyed where the crack opened. Also shown at point III on the stress-strain curve is a second crack which has propagated through the fabric surface above the first crack. Between the two cracked regions the fabric strain has reduced to zero (blue contour color). Parts (d) and (e) in Figure 22 show typical sample failure profiles and surfaces. The failure profiles of 65P show clear cracks through the fabric layer. Although it is hardly visible in these images, the Saffil® layer failure occurred at approximately a 45º angle indicating a shear failure within the layer while the fabric cracks were straight through the thickness of the layer. Figure 23 is for the 65P Inverted sample with strain contours at similar locations on stress strain curve for comparison to 65P. Although there are bands of high strain on the surface of the sample (red contour sections at locations I and II) these regions do not correspond to cracks in the Saffil® layer. This region ultimately did crack and failure occurred at this location further along in the stress strain curve, with the crack visible and beginning to form in image III. No cracks were seen on the outer

Saffil® layers in any 65P Inverted sample other than the catastrophic crack. This is as expected, the inner fabric layers were expected to crack while the outer Saffil® layers bridged the cracks.

Similar images for the remaining hybrids are displayed in Figures 24 through 27. Each hybrid will not be discussed in detail since it will be repetitive, only the differences will be highlighted here. No failures were caught within the DIC images for hybrid 48P resulting in the uninformative strain fields. What they do show are banded regions of high strain at the peak load after which the sample becomes unstrained shown by the scattered color contour of high and low strains. These DIC images were taken away from the failure location and therefore indicate unloading at cracking is not localized like in 65P. Upon cracking large sections of the fabric layer are being unstrained while in hybrid 65P the fabric layer had narrow unstrained bands surrounding the cracks. Hybrid 87B was the only other sample to display visibly cracked outer fabric layers. This was also the only other hybrid with a single outer layer of fabric while the other hybrids had either 2 or 3 stacked outer fabric layers. Even though approximately 20 cracks were visible along the gage length of 87B they had no positive effect on the hybrid behavior and did not result in any loading/unloading behavior. The observed unloading/loading behavior in the hybrids which did not have outer cracked fabric layers but clearly underwent damage may be cracking within the fabric layers in contact with the Saffil®. The failure profiles of all hybrids have similar features with straight failures through the fabric layer and shear failure through the Saffil® layer. Based on the location and consistent spacing of cracks in the 65P laminate it is believed the fabric cracks are to following the weave geometry. Similar crack spacing was observed in hybrid 87B. An interesting feature in 54B (Figure 27 c. III) is the strain contour at location III in the axial stress-axial strain curve. A large crack through the fabric layer is visible in the contour however this image is within the gradual unloading portion of the stress strain curve. This evidence suggests the gradual unloading behaviors may be attributed to failure of the discontinuous layer.

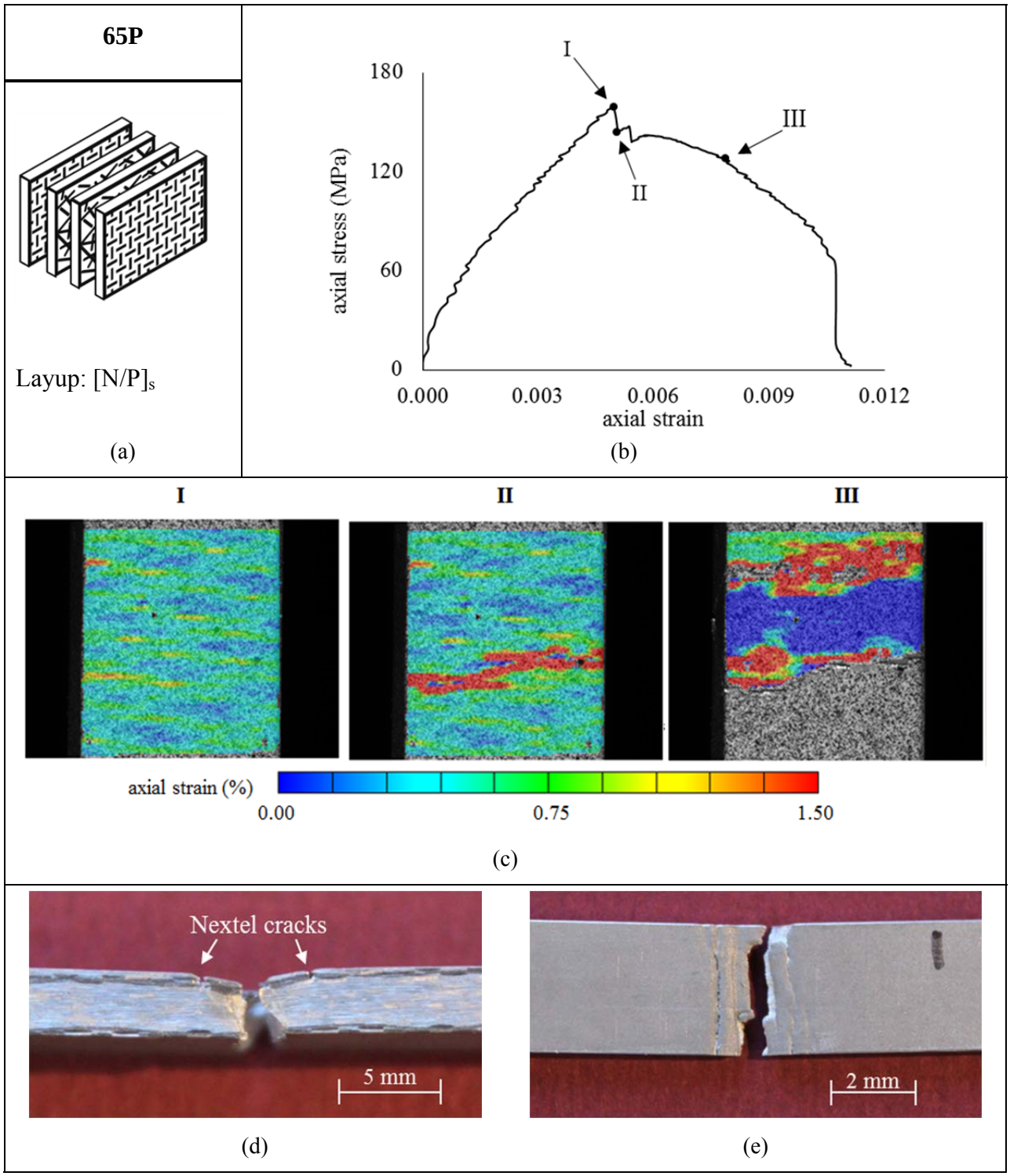

Figure 22. Hybrid laminate 65P: (a) layup schematic, (b) typical uniaxial tension stress strain curve with labeled regions (I), (II), and (III) corresponding to the DIC axial strain contours in (c). Failed sample side (d) and top profiles (e) showing non-catastrophic cracks in the outer Nextel™ layer.

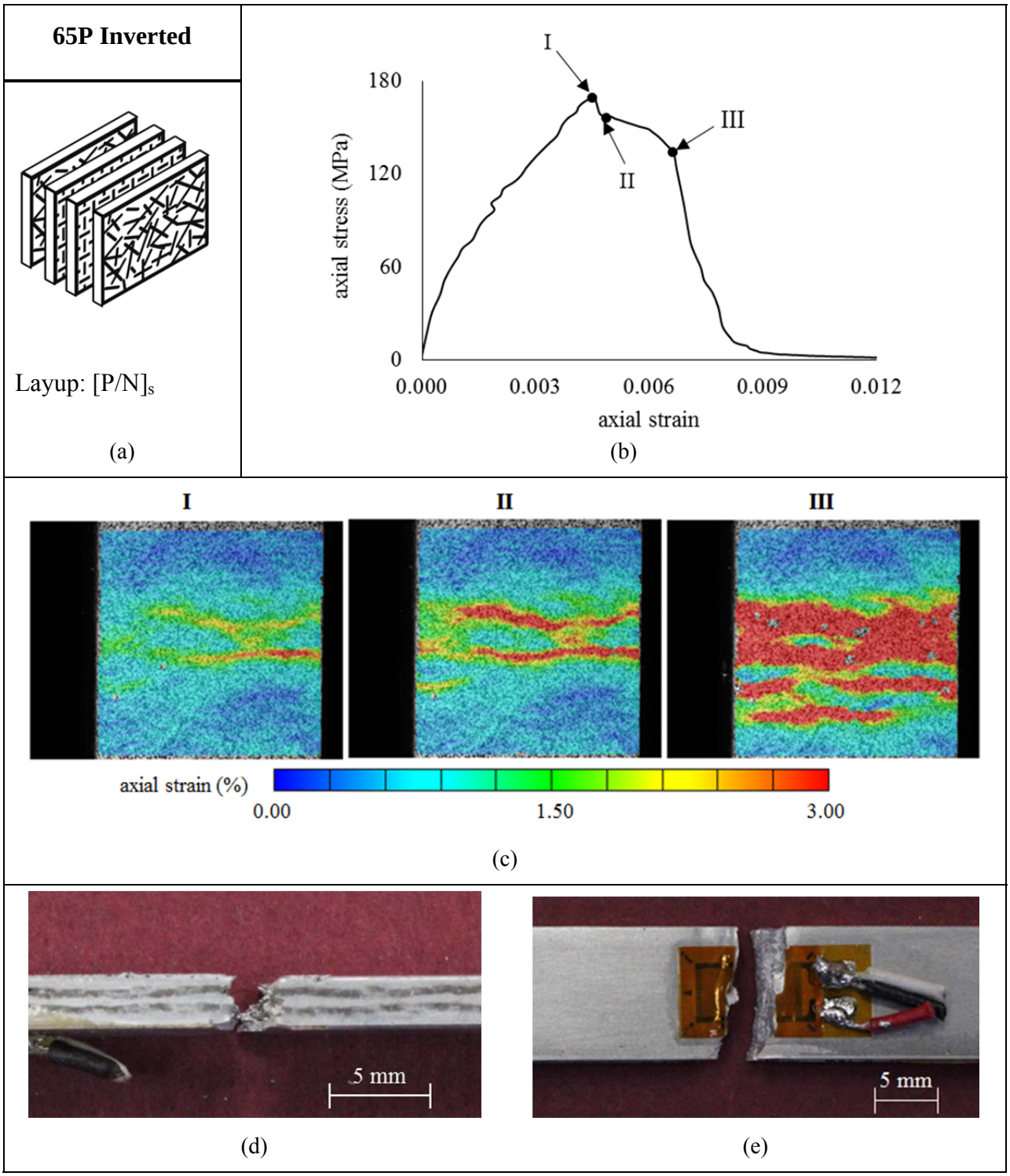

Figure 23. Hybrid laminate 65P Inverted: (a) layup schematic, (b) typical uniaxial tension stress strain curve with labeled regions (I), (II), and (III) corresponding to the DIC axial strain contours in (c). Failed sample side (d) and top (e) profiles.

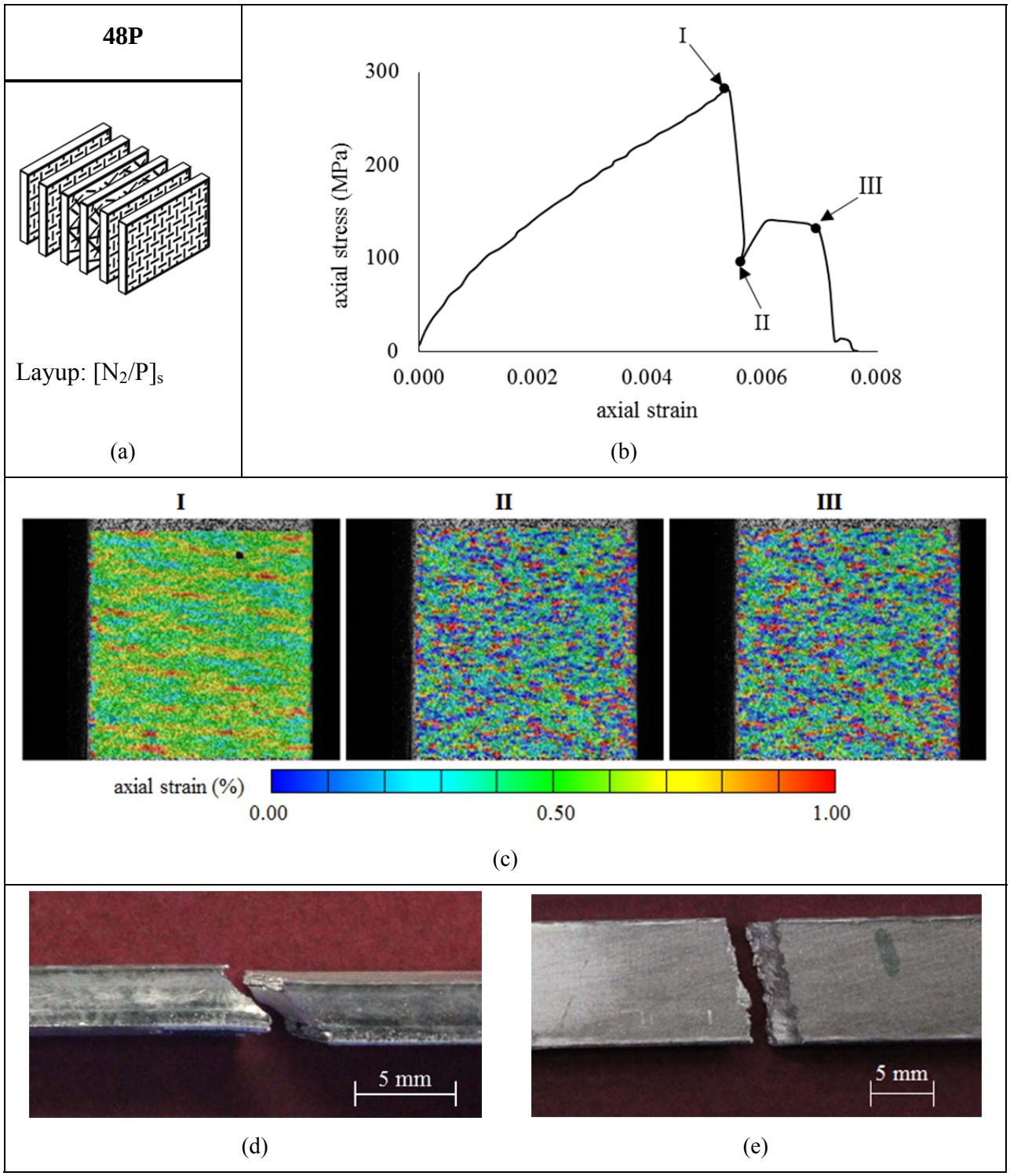

Figure 24. Hybrid laminate 48P: (a) layup schematic, (b) typical uniaxial tension stress strain curve with labeled regions (I), (II), and (III) corresponding to the DIC axial strain contours in (c). Failed sample side (d) and top (e) profiles.

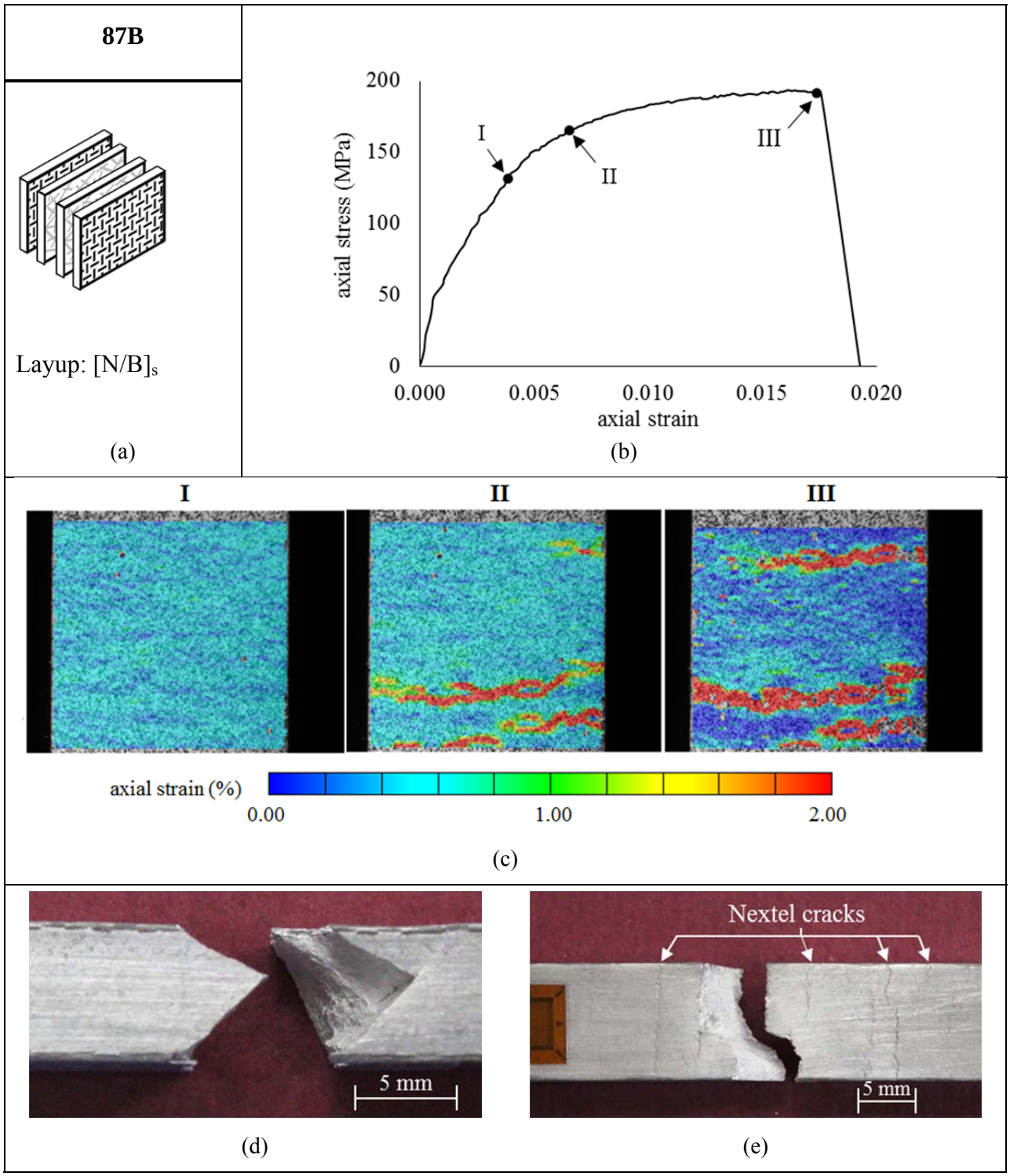

Figure 25. Hybrid laminate 87B: (a) layup schematic, (b) typical uniaxial tension stress strain curve with labeled regions (I), (II), and (III) corresponding to the DIC axial strain contours in (c). Failed sample side (d) and top (e) profiles showing non-catastrophic cracks in the outer Nextel™ layer.

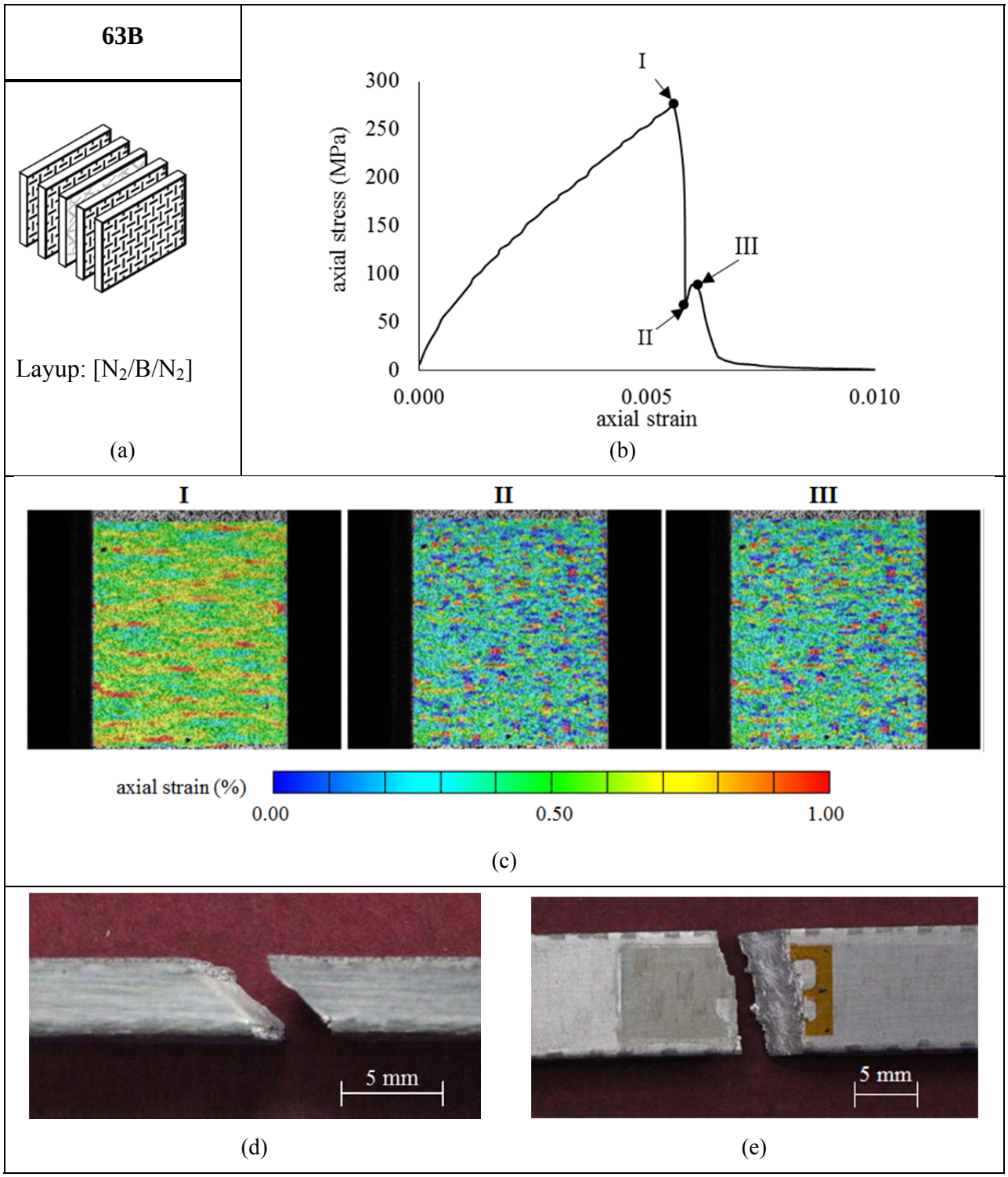

Figure 26. Hybrid laminate 63B: (a) layup schematic, (b) typical uniaxial tension stress strain curve with labeled regions (I), (II), and (III) corresponding to the DIC axial strain contours in (c). Failed sample side (d) and top (e) profiles.

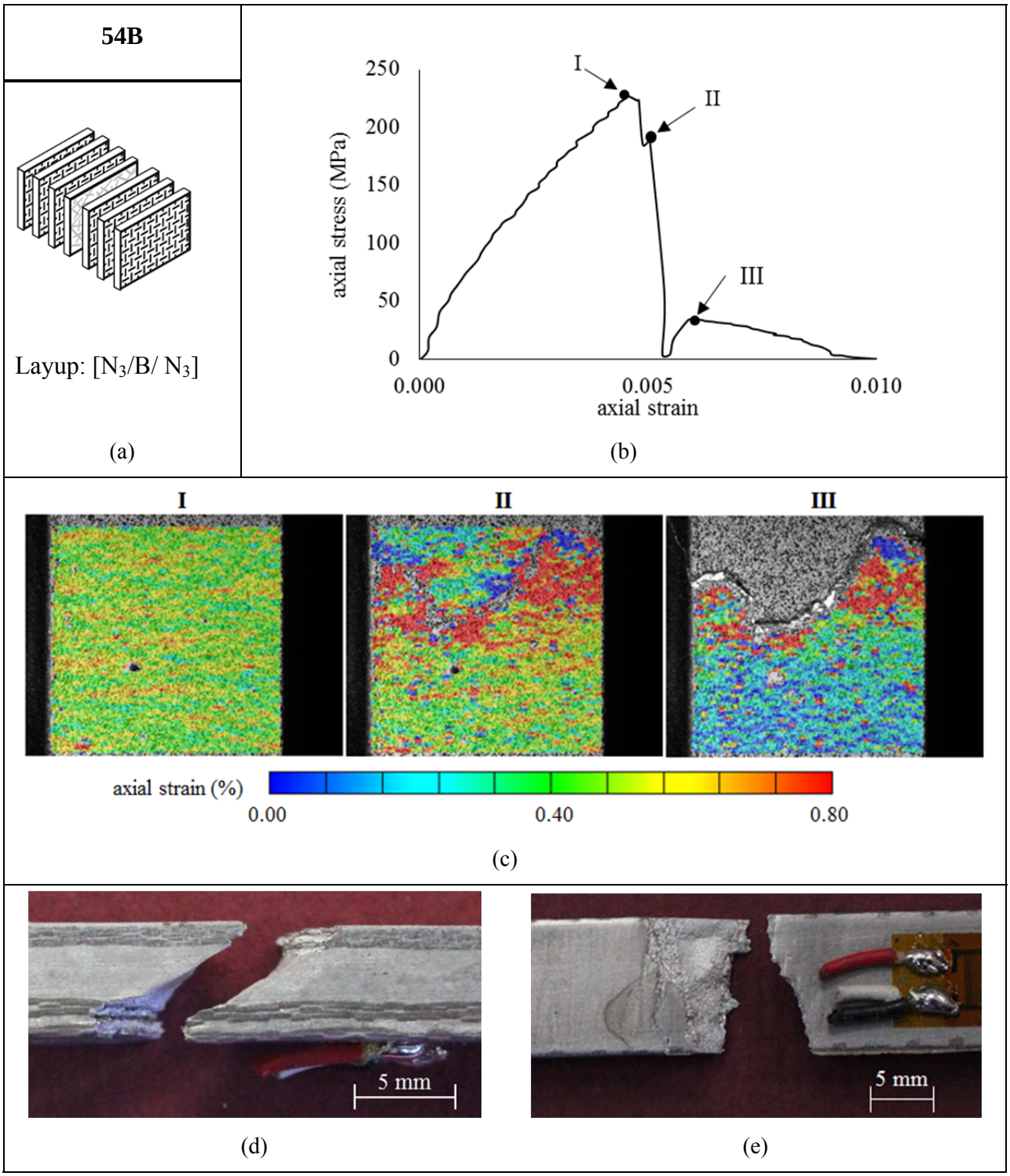

Figure 27. Hybrid laminate 54B: (a) layup schematic, (b) typical uniaxial tension stress strain curve with labeled regions (I), (II), and (III) corresponding to the DIC axial strain contours in (c). Failed sample side (d) and top (e) profiles.

Table IV. Hybrid composite properties. †

Hybrid Composite	**Layup**	**Strength (MPa)**	**Modulus (GPa)**	**Cracking Strain (%)**	**Failure Strain (%)**	**Density $\left(\frac{g}{mm^3}\right)$**	**Modulus of Toughness $\left(MPa \cdot \frac{mm}{mm}\right)$**	**Thickness (mm)**	**Population Size**
65P	$[N/P]_s$	150	104	0.44	1.01	2.91	0.88	3.10	11
65P Inverted	$[P/N]_s$	170	104	0.47	1.04	2.88	0.79	2.78	9
48P	$[N_2/P]_s$	280	145	0.54	0.71	2.98	1.14	3.28	10
87B	$[N/B]_s$	200	131	none	1.89	2.86	3.08	7.15	8
63B	$[N_2/B/N_2]$	260	127	0.53	0.56	2.99	0.91	4.02	15
54B	$[N_3/B/N_3]$	220	149	0.45	0.75	2.97	0.79	5.81	9

† Standard deviations for each of the properties listed in Table III can be found in Appendix A.

5.2 Hybrid Composite Properties

Average properties for all hybrid samples characterized are reported in Table IV. One of the goals of this work was to maintain a similar specific strength and specific stiffness as the fabric composite in the hybrid composites. Specific stiffness and specific strengths for the hybrid and single reinforced composites are plotted in Figure 28. The board and paper composites have the lowest specific stiffness. Hybrid composites 87B, 63B, 54B, and 48P have similar or improved specific stiffness than the fabric composite. Looking at specific strength, hybrid 63B and 48P have similar properties as the fabric composite. The specific strength of hybrid 48P is higher than the fabric composite because it has a lower density. Hybrid 48P has both an improved specific strength and specific stiffness compared to the fabric composite.

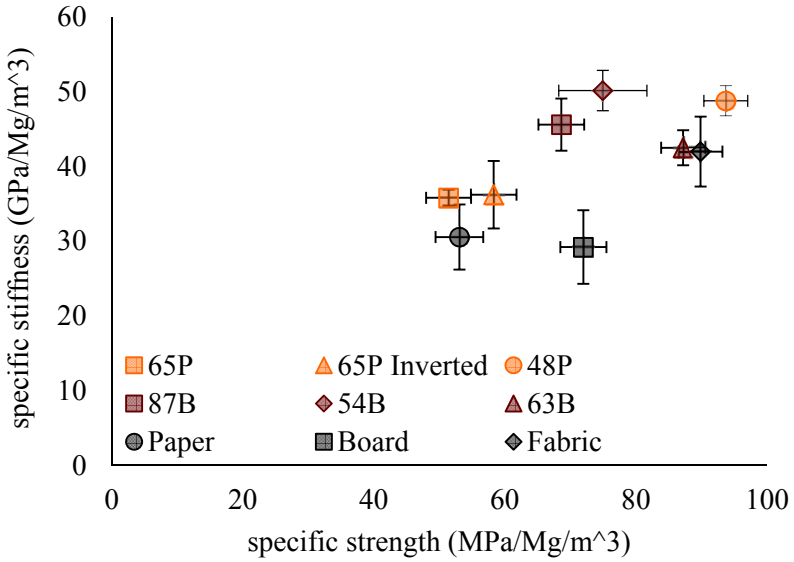

Figure 28. Average composite specific stiffness and specific strength.

Another hybrid goal was to increase the toughness or amount of energy required to fail the composite sample. This is reported as the modulus of toughness in Figure 29 and Table IV and is equal to the area under the axial stress-axial strain curve. Due to the high paper composite failure strain it has a modulus of toughness much greater than any of the other composites, followed by the Saffil® board and 87B hybrid composite. Properties for the remaining hybrids are shown in Figure 29 all displaying about a 30% higher modulus of toughness than the fabric composite. Although 65P and 65P Inverted were able to sustain higher loads post cracking for large strains they have a similar modulus of toughness as the other hybrid composites. Once again, hybrid 48P has the largest improvement in properties with an improved specific strength, similar specific stiffness and improved modulus of toughness compared to the fabric composite.

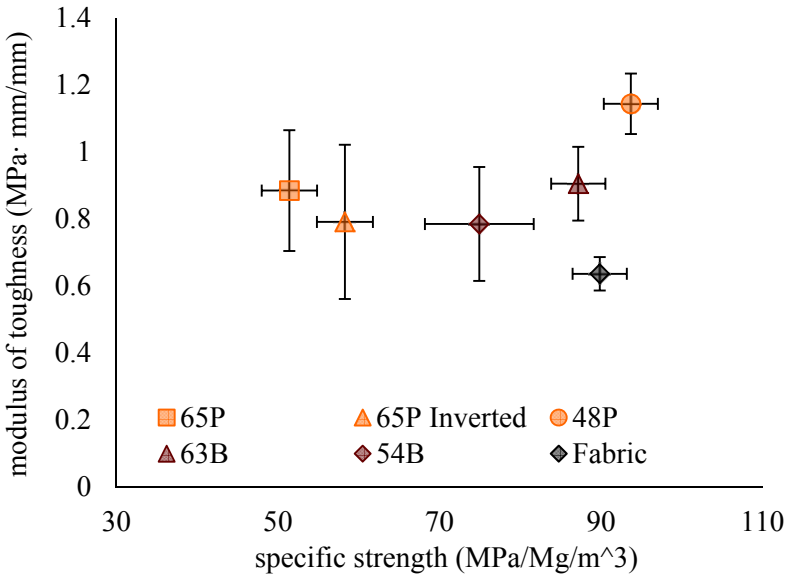

Figure 29. Average composite modulus of toughness and specific strength.

Figure 30 reveals the effect the amount of discontinuous reinforcement has on composite failure strain and cracking strain. The discontinuous fiber content was estimated using the single reinforced composite theoretical fiber volume fraction and layer thickness. The amount of Saffil® fiber divided by the total volume of fiber in each composite is reported here as the discontinuous fiber content. The Saffil® paper and board composites had the highest failure strains at 0.075 and 0.019 strain respectively. Figure 31 excludes the Saffil® paper failure strain to magnify the differences in hybrid failure and cracking strains. Hybrid composite 87B (78% discontinuous fiber content) had a slightly lower failure strain than the board composite but did not have multiple loading/un-loading portions of the hybrid axial stress-axial strain curves. Excluding 87B, hybrid 65P and 65P Inverted (28% discontinuous fiber content) had the highest failure strain as well as the lowest cracking strain among the hybrids. The hybrid layups chosen resulted in a gap in composite properties obtained at discontinuous fiber contents between 47% and 78%. All hybrid composites had higher failure and cracking strains than the Nextel™ fabric composite. Hybrid 48P (17% discontinuous fiber content) had the highest cracking strain at 25% higher than the fabric composite (0% discontinuous fiber content). There is no clear relationship between discontinuous fiber content and failure/cracking strain.

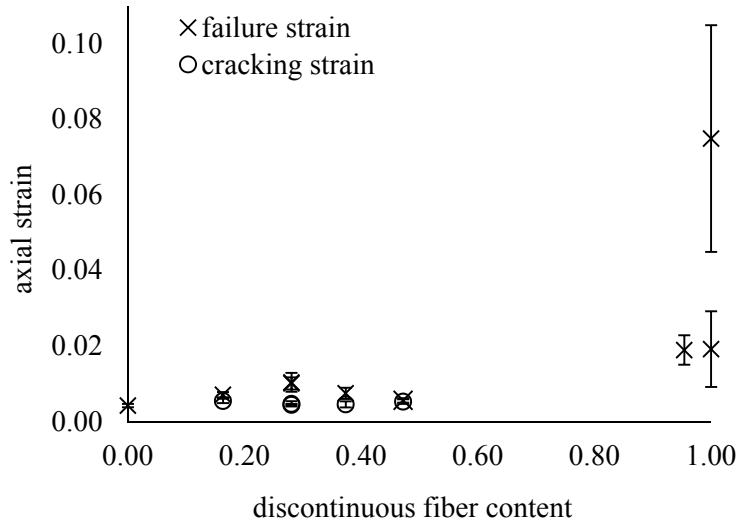

Figure 30. Effect of discontinuous fiber content on composite failure strain and cracking strain.

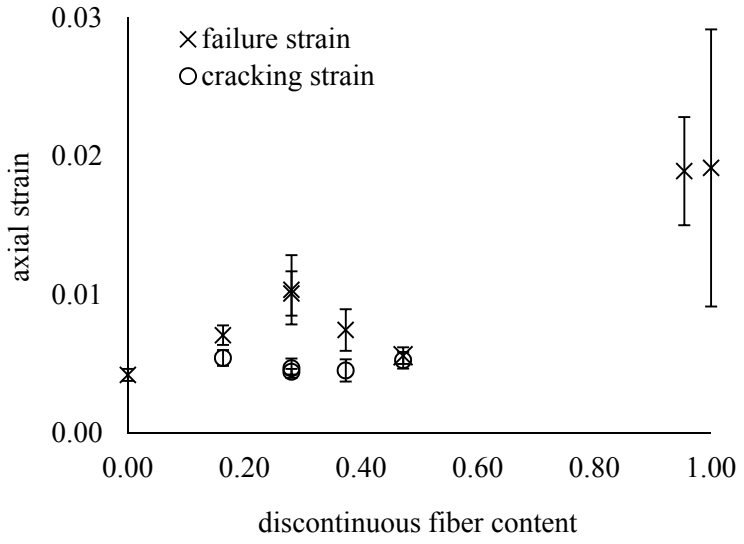

Figure 31. Excluding Saffil® paper failure strain (0.075 strain), effect of discontinuous fiber content on composite failure strain and cracking strain.

The final consistent characteristic in the hybrid behavior was the cracking strain and failure strain. The cracking strain is the strain which occurred at the peak axial load and onset of damage. Failure strain is the strain at which the sample unloaded to carry zero load. The percent increase in axial failure strain is the difference between the fabric axial failure strain and the hybrid axial failure strain. Similarly, the axial cracking strain percent difference is the difference between the hybrid cracking strain and the fabric composite failure strain. The percent difference between the hybrid cracking strain and the fabric failure strain are plotted in Figure 32 along with the percent difference in hybrid axial failure strain. Hybrids exhibiting higher cracking strains had smaller increases in failure strain. At the point of cracking more energy is stored in the sample which must be released once damage occurs. The hybrids which prolong cracking at similar loads as the fabric composite cannot efficiently redistribute the released load due to damage within the sample thus initiating the large drop in axial load and minimal reloading before ultimate failure. Hybrids 65P and 65P Inverted reached lower axial cracking strains and were able to effectively handle progressive damage accumulation and reach higher axial failure strains.

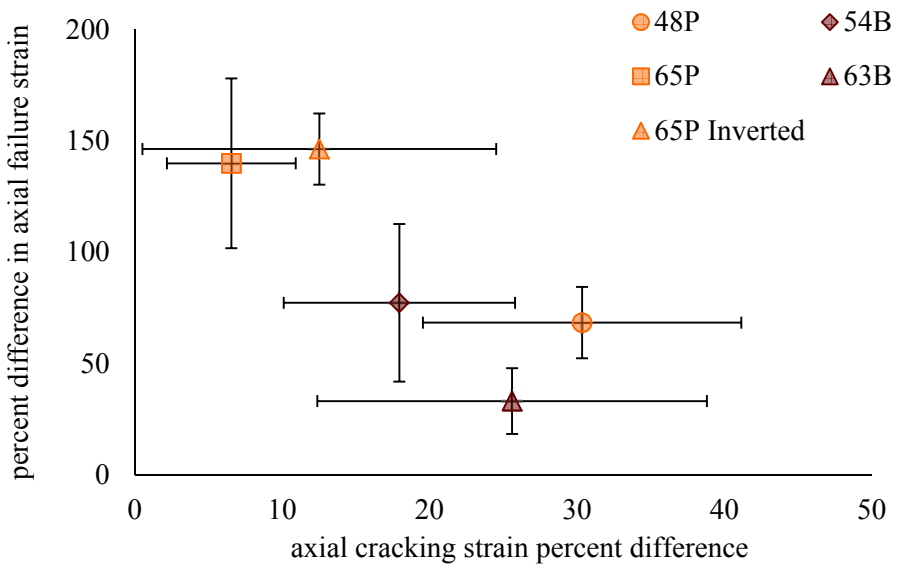

Figure 32. Relation between the average increase in hybrid composite failure strain and cracking strain compared to the fabric composite failure strain.

5.3 Hybrid Behavior Discussion

Two distinct behaviors were observed in the hybrid composites characterized in this work. A hybrid behavior which displayed the desired specific strength and stiffness properties similar to the fabric composite was seen. These hybrids, 48P and 63B, had a similar strength and higher cracking strain than the fabric composite. After initial failure, large decreases in load were observed with very small reloading portions of the axial stress-axial strain curve making the progressive failure of these samples more catastrophic and abrupt. The second type of hybrid behavior was observed in 65P and 65P Inverted. These hybrids reached a little over half the strength of the fabric composite but they exhibited an effective damage response. Once the maximum load was reached, small decreases in load were seen, approximately 10%, and was followed by stable damage propagation in the sample with slow steady unloading (65P Inverted) or reloading and unloading (65P) of the sample gradually reaching ultimate failure. Contrary to Aveston and Kelly's work on continuous unidirectional hybrid composites [5], outer continuous layers resulted in a more effective hybrid damage response and higher failure strains. In 65P, the outer layers were able to deform more, absorbing more energy through deformation instead of transferring load into the Saffil® layer. With inner fabric layers, it is believed, that the cracks were confined by the Saffil® layers and damage was not effectively redistributed into the undamaged layers. This resulted in the convex unloading behavior and no reloading portions or additional fabric cracks occurring, as evidenced in the stress strain behavior. There is a limit to the effect the continuous layer can have, hybrid 87B had a decreased failure strain due to the hybrid lamination, creating a composite which is less effective than the Saffil® board layer alone. Five of the six hybrid laminates had enhanced properties with a higher modulus of toughness (area under the axial stress-axial strain curve) and failure strain than the continuous fabric composite. Four hybrids had a higher specific stiffness than the fabric composite while one hybrid 48P had both a higher specific stiffness and specific strength than the fabric composite. As hybrid composite discontinuous fiber content increased, there was no clear effect on cracking and failure strain. Up to a 150% increase in hybrid failure strain was measured with the highest cracking strain improvement being 30%. Hybrids with higher failure strains also had lower cracking strains, indicating cracking strain as an important hybrid property.

The ideal hybrid would have a combination of the behaviors observed, creating a hybrid with a high strength, increased cracking strain, and stable damage propagation with gradual loading and unloading curves ultimately reaching strain values 3 to 4 times larger than the fabric composite. The six hybrids characterized here were chosen based on available reinforcing layer thicknesses, limitations to the abilities of the tensile testing equipment, and to cover a range of discontinuous/continuous reinforcement ratios. Now that these hybrids have been characterized, there is a basis to which predictions can be compared. To design a hybrid with ideal behavior modeling efforts are needed to determine the properties of the discontinuous layer and ratio of reinforcements necessary. As evidenced in the failure behavior observed here, hybrid failure is controlled by the failure response of the Nextel™ fabric layer. The approach chosen in this work, to predict failure of the fabric composite, is a stochastic damage evolution model discussed in Section 7. To simplify the complex fabric geometry it will be looked at as consisting of two continuously reinforced layers of unidirectional and transverse fiber. Modeling the behavior of the discontinuous Saffil® reinforced composite is beyond the scope of this work and the experimental behavior will be used. Finally, an initial hybrid composite model will be made and used to predict the behavior of hybrids 65P and 65P Inverted in an attempt to capture the gradual progressive failure observed in these composites.

6 CONTINUOUS FIBER CHARACTERIZATION

6.1 BACKGROUND

Stochastic damage evolution models, used in this work, to predict the tensile strength of fiber reinforced metal matrix composites depend greatly on fiber mechanical property statistics or cumulative distribution functions (CDF) used as inputs [26]. Two different types of Nextel™ 610 fibers were used to reinforce the fabric (Nextel™ 610 3,000 denier) and the unidirectional (Nextel™ 610 10,000 denier) composites. Scanning electron microscope (SEM) imaging revealed significantly different cross sectional shapes for the 3,000 and 10,000 denier fibers, Figure 33. For imaging, fiber ends were cut with a pair of ceramic scissors creating the large stepped fracture on a portion of the end of the fiber. These two images are not representative of the fiber fracture surface under uniaxial tensile loading. The 3,000 denier fiber cross section is circular while the 10,000 denier fiber has a peanut shaped cross section. Approximately one out of every twenty 10,000 denier fibers had a round cross section. Nextel™ 610 fiber properties found in the literature were for 1,500 denier fiber [27] or the denier was not reported [28] and all references listed the fiber cross section to be circular. The lack of 3,000 and 10,000 denier properties and difference in the 10,000 denier cross sectional shape compared to the literature indicates the need to measure fiber properties using single fiber tension tests.

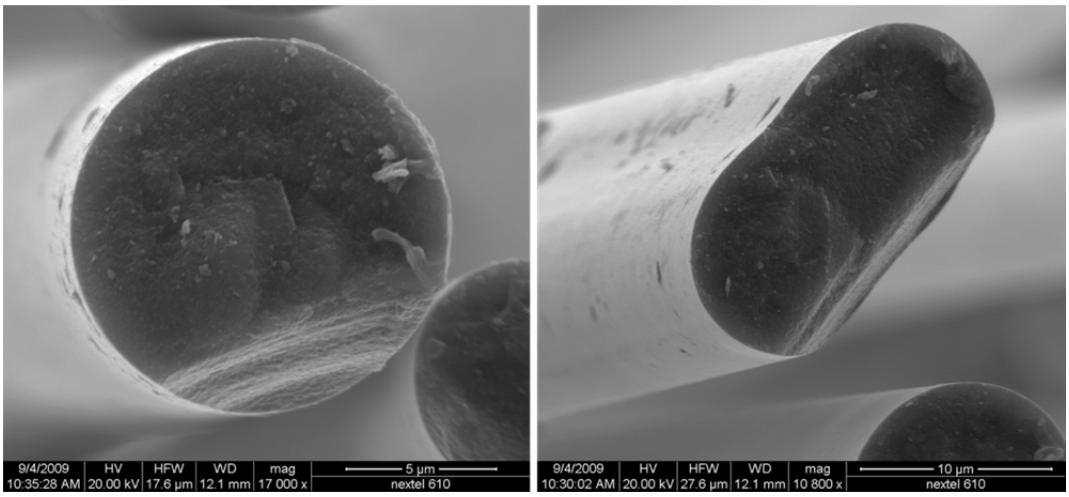

Figure 33. Nextel™ 610 3,000 denier (left) and 10,000 denier (right) typical cross sectional shapes.

In addition to characterizing unprocessed fiber properties for both the 3,000 and 10,000 denier Nextel™ 610 fiber, another goal of this work was to determine the in-situ fiber properties. During processing, damage to fibers can occur, which degrades fiber properties and results in reduced composite strengths. In certain metal matrix composites fibers can be extracted from a processed composite through chemical reactions [29-31]. Fibers successfully extracted from composites have exhibited decreased strengths when compared to their unprocessed counterparts. Using an etching technique, Asthana et al. extracted sapphire fibers from a nickel alloy composite and measured a 66% decrease in fiber strength [29]. Draper and Locci extracted alumina fibers from various MMCs through etching and reported a 30% - 50% reduction in fiber strength for the extracted fibers [30]. Carbon fibers have been extracted from an aluminum matrix composite using a sodium hydroxide treatment and a 40% decrease in fiber strength was measured [31]. In this work, a sodium hydroxide treatment was used to extract alumina fibers from the unidirectional and fabric composites. Single fiber tension testing was performed to determine the effect composite processing has on fiber strength. The measured and literature fiber properties were then used to predict unidirectional composite strengths through a stochastic damage evolution model. Finally, the predicted and experimental composite strengths were compared to determine if using the extracted fiber properties results in a significant improvement in the composite strength prediction over the literature or unprocessed fiber properties.

6.2 Fiber Mechanical Testing

Strength measurements for Nextel™ 610 3,000 denier fiber and 10,000 denier fiber both unprocessed and extracted were obtained using single fiber tension testing. The unprocessed alumina fibers were manufactured with a sizing, which was burned off in an open air furnace at 800°C for one hour [27]. Fibers were extracted from two metal matrix composites using a one hour sodium hydroxide treatment [31].

Figure 34 shows a composite section before and after the extraction treatment resulting in clean as-processed fibers. To quantify the effect of the extraction process on fiber properties, unprocessed fibers were exposed to the sodium hydroxide treatment for one hour and will be referred to as “treated”. Single fiber tension test preparation was similar to that employed by Feih

et al. [32] in which each fiber was glued onto a paper tab with Loctite® 454. The paper tab was used to ensure a consistent gauge length of 10.95 mm for each fiber tested. Next, the paper tab was gripped in a TA Instruments Q800 load frame and the sides of the paper tab were cut ensuring only the fiber was carrying load during the experiment, Figure 35. The fibers were then loaded in tension at the strain rate specified in ASTM D3552 for tensile testing of metal matrix composites (0.001 s^{-1}) to be consistent [20]. Load and strain data were recorded for each fiber population. Stress was calculated assuming that the fiber radius did not vary from sample to sample for each denier type. This assumption was based on fiber cross sectional area measurements made using optical microscopy images of polished composite cross sections. Average fiber cross sectional areas were 122 μm^2 and 120 μm^2 for the 3,000 and 10,000 denier fiber.

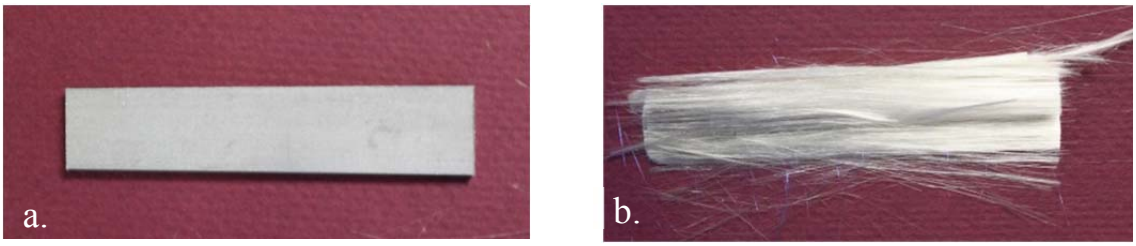

Figure 34. Cast composite section before (a) and after (b) sodium hydroxide fiber extraction treatment.

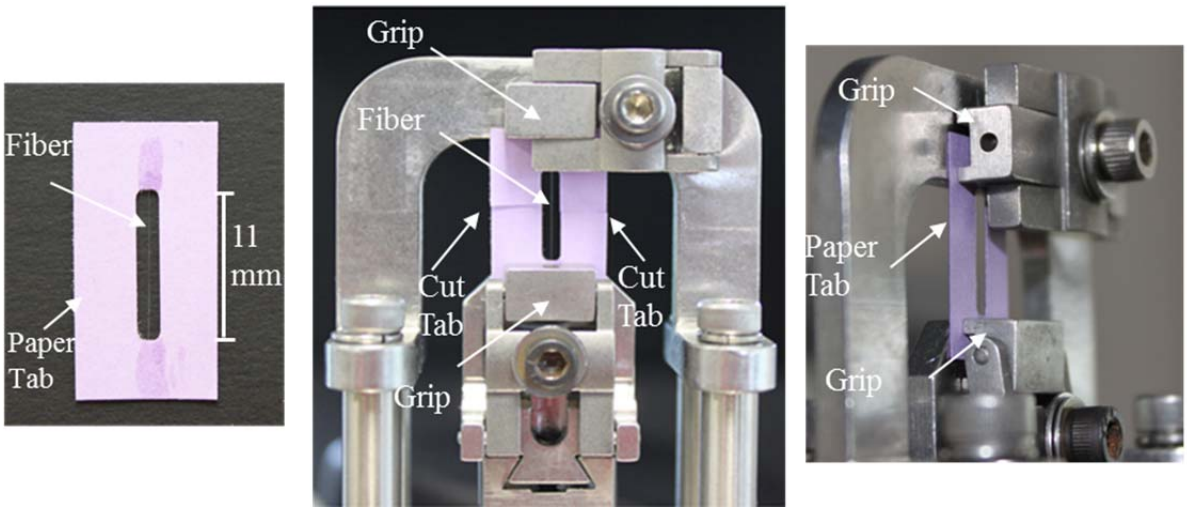

Figure 35. Single fiber tension test specimen loaded in Q800 load frame.

6.3 WEIBULL DISTRIBUTION

Weibull developed a probability approach to define a cumulative distribution function (CDF) for the strength of materials [33]. In this work, Weibull distributions will be used to define strength populations for the Nextel™ 610 fiber and fabric composite strength predictions. Once the fiber CDF is defined, the distribution will be used to randomly assign segment properties in a stochastic damage evolution model to predict unidirectional fiber reinforced composite strength.

The Weibull distribution is based on a statistical flaw based theory where a volume of stressed material contains evenly distributed flaws that will initiate failure. Ultimate failure occurs when the applied stress exceeds the weakest flaw strength. A larger volume of material will contain more flaws, which increases the probability of having weak flaws and therefore a lower strength. This approach assumes stresses are uniformly distributed throughout the sample volume. A two parameter Weibull distribution can be used to describe uniaxial strength populations of materials which have a uniform cross section along the length of the sample. A brief summary of a two parameter Weibull distribution and how to apply it to strength populations is described below.

The flaw based model requires a population of fiber strengths to be measured at a constant gage length, L_o. According to the theory, the probability of failure, $P_f(\sigma)$, for a fiber segment at a given stress σ is defined in Equation 1. In this equation, V represents the stressed volume, while σ_o and m are the two fit parameters which define the strength distribution. If it is assumed that there are no changes in cross sectional area along the length of the sample then the volume of stressed material loaded uniaxially is proportional to its length. The probability of failure can then be simplified to Equation 2 where L is defined as any sample length and L_o is the gage length of the sample tested.

$$P_f(\sigma) = 1 - \exp\left(-V\left(\frac{\sigma}{\sigma_o}\right)^m\right) \quad (1)$$

$$P_f(\sigma) = 1 - \exp\left(-\frac{L}{L_o}\left(\frac{\sigma}{\sigma_o}\right)^m\right) \quad (2)$$

To determine the fit parameter values a graphical method can be used by linearizing the probability of failure function. When determining fit parameters $L = L_o$ and Equation 2 is simplified to Equation 3. To create the plot, a form for the probability of failure is assumed using a probability estimator. In this work, the probability estimator chosen is defined in Equation 4. P_f is a function of the number of strength data points where $n = 1 \ldots N$ with N equaling the total number of data points.

$$\ln\left(\ln\left(\frac{1}{1 - P_f(\sigma)}\right)\right) = m \ln(\sigma) - m \ln \sigma_o \quad (3)$$

$$P_f = \frac{n - 0.3}{N + 0.4} \quad (4)$$

A plot of $\ln\left(\ln\left(\frac{1}{1-P_f(\sigma)}\right)\right)$ versus $\ln(\sigma)$ is then generated and the two Weibull fit parameters are calculated by applying a linear regression to the data. If the linear regression represents the data then a two parameter fit is appropriate for the strength population. The Weibull modulus m is the slope of the linear regression. It is a measure of the scatter in the strength data and is independent of sample volume. The second fit parameter σ_o is referred to as the Weibull strength and is a function of the intercept and slope of the linear regression, Equation 5. Fiber length scales in the stochastic damage evolution model are much smaller than the ones used in tension testing. To properly assign material properties the Weibull distribution must be scaled through calculation of the characteristic strength for the new gauge length, L as defined in Equation 6.

$$\sigma_o = \exp\left(-\frac{\text{intercept}}{m}\right) \quad (5)$$

$$\sigma_1 = \sigma_o \left(\frac{L_o}{L}\right)^{\frac{1}{m}} \quad (6)$$

6.4 NEXTEL™ 610 FIBER PROPERTIES

Nextel™ 610 fibers have linear elastic behavior in uniaxial tension as shown in Figure 36 for three typical fiber tests. Fiber properties measured through single fiber tension testing are summarized in Table V. A 13% and 15% decrease in strength was seen for the extracted 3,000 and 10,000 denier fibers. Similarly, the Weibull mean strength and modulus were higher for the unprocessed fibers than those for the extracted fibers. Weibull probability plots for all five fiber populations are shown in Figure 37. As shown in the Weibull plot, the fiber strength populations are nearly linear and therefore are accurately represented by the two parameter Weibull CDF. The treated unidirectional fiber population had a small decrease in properties and similar strength distribution compared to the unprocessed unidirectional fiber. This decrease could be due to the additional handling the treated fibers endured however, the utmost care was taken to not bend or induce damage to the fibers during handling. To check for a negative chemical reaction to the sodium hydroxide solution, SEM images were taken of the unprocessed, desized, treated and extracted fibers, Figure 38. The treated and extracted fiber images show an increased amount of debris on the fiber surfaces however, no indication of damage was seen in any of the treatment images. Other than the debris, all fiber sides were smooth and no pitting or erosion was observed, further indicating the desizing and sodium hydroxide treatment did not induce damage to the fibers. The Nextel™ 610 10,000 and 3,000 denier fiber properties measured in this work are lower than those reported by Wilson [28] and Gonczy [27], reproduced in Table VI. The Weibull moduli measured here are around 4 while reported values are between 6 and 10. A smaller Weibull modulus indicates a larger amount of scatter in the strengths measured indicating the measured strengths have a larger range. Weibull strength comparison must be done at equivalent gage lengths. Using Equation 6, Wilson and Gonczy's Weibull strengths at the gage length used in this work are 3480 MPa and 3550 MPa respectively. The reported Weibull strengths are between approximately 9% and 28% higher than the unprocessed fiber populations. The measured and reported fiber properties will be used to simulate composite strengths and determine the effectiveness of measuring extracted fiber properties from untested composites to improve prediction accuracy.

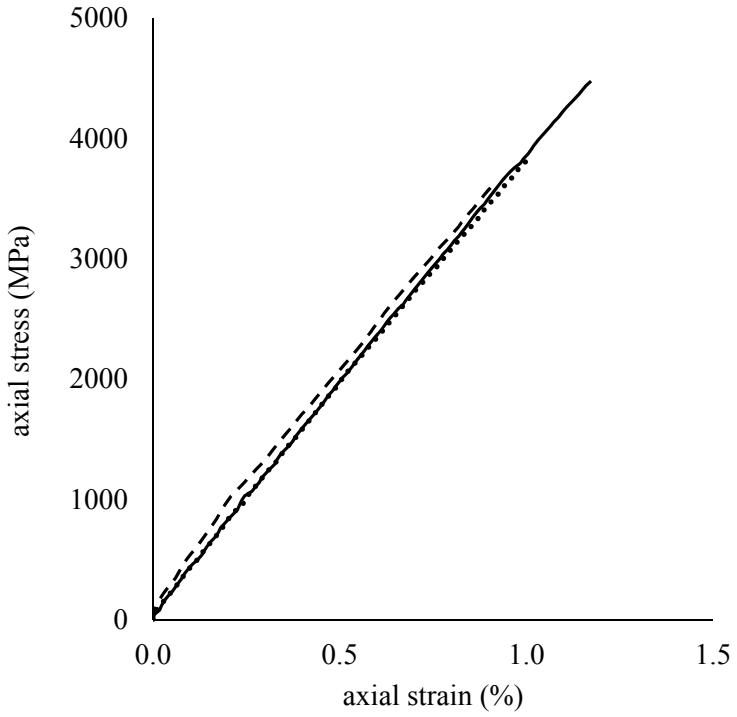

Figure 36. Typical uniaxial tension axial stress-axial strain behavior of Nextel™ 610 10,000 fiber.

Table V. Nextel™ 610 fiber properties.

Property	Woven fabric fiber 3,000 denier		Unidirectional fiber 10,000 denier		
	Unprocessed	Extracted	Unprocessed	Treated	Extracted
Weibull strength (MPa)	2500	2170	3190	3010	2700
Weibull modulus	4.99	3.73	4.46	4.20	4.26
Strength (MPa)	2300	2000	2900	2730	2500
Axial modulus (GPa)	265	324	370	350	340
Strain to failure (%)	0.87	0.62	0.77	0.76	0.70
Population size	82	77	90	42	53

Table VI. Reported Nextel™ 610 fiber properties.

Property	Literature reference	
	Wilson [28]	Gonczy [27]
Weibull strength (MPa), $L_o = 25$ mm	3220	3130
Weibull strength (MPa), $L_o = 11$ mm	3480	3550
Weibull modulus	10.54	6.62
Strength (MPa)	3077	3070
Axial modulus (GPa)	380	-
Denier	unknown	1500

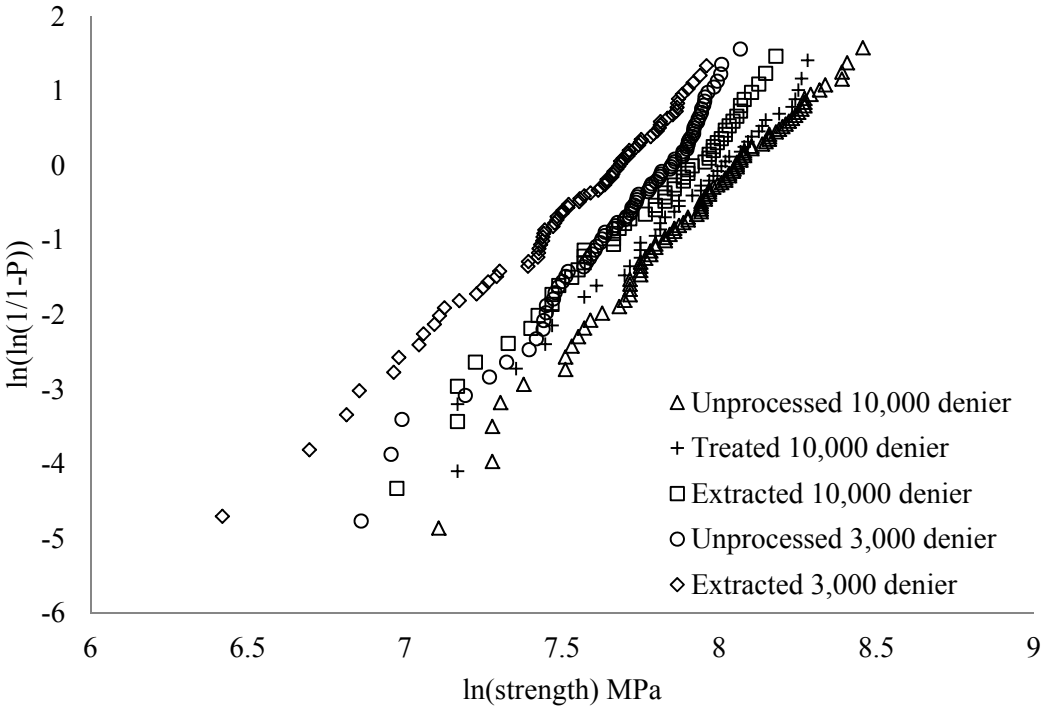

Figure 37. 3,000 and 10,000 denier Nextel™ 610 fiber Weibull probability plot.

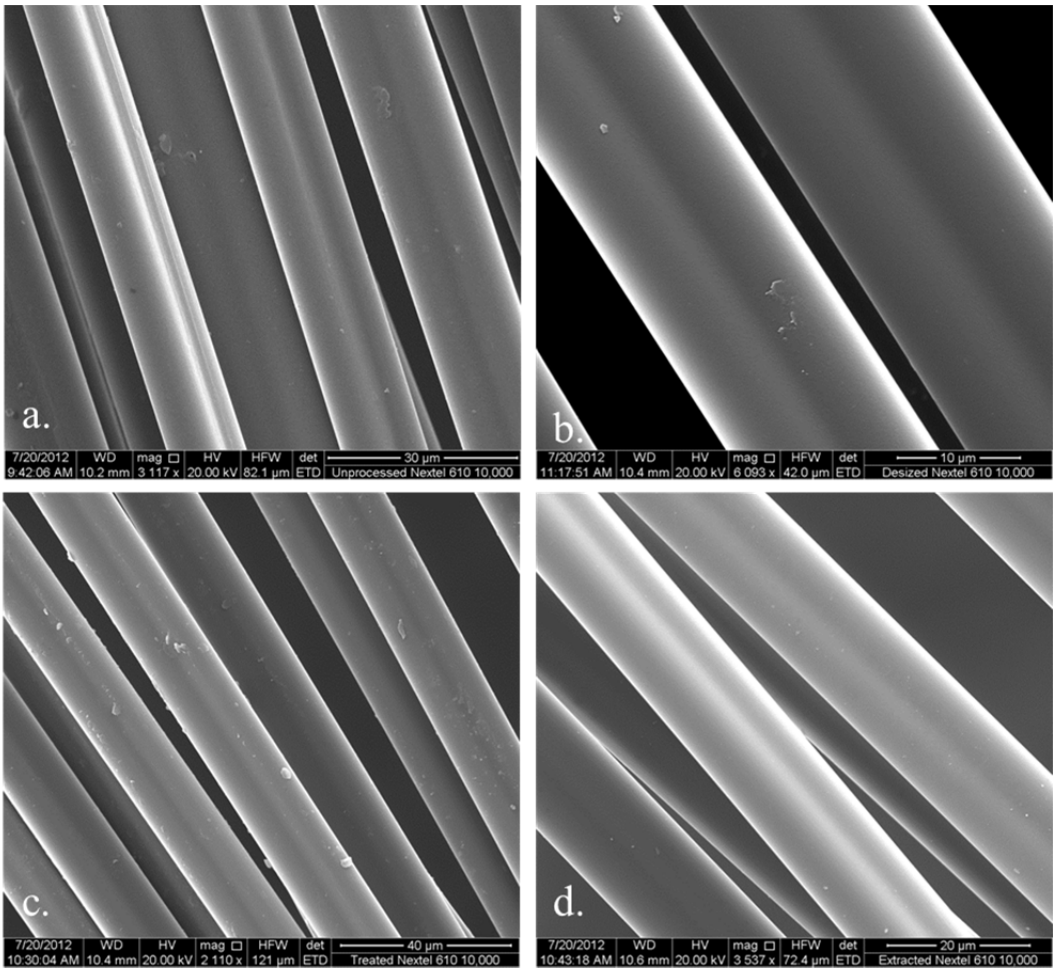

Figure 38. Scanning electron microscope images of Nextel™ 610 10,000 denier fibers unprocessed (a), desized (b), treated (c), and extracted (d).

7 CONTINUOUS COMPOSITE MODEL

Continuous/discontinuous fiber reinforced hybrid composite failure was driven by damage in the continuous fabric reinforced MMC layer. A key parameter in a future hybrid model is being able to predict failure of the fabric composite layer based on constituent (fiber and matrix) properties alone. Modeling of the continuous fiber reinforced Nextel™ fabric layer is complex and therefore has been simplified to predicting the uniaxial tension behavior of a unidirectional axial fiber reinforced composite and volume averaging stress with the transverse composite experimental results, [0°/90°]. This simplified approach idealizes the fabric composite to laminated layers of unidirectional axial (0°) and transverse (90°) continuous fiber reinforced MMCs. Prediction of the unidirectional axial fiber reinforced composite strength was accomplished by applying Xia and Curtin's stochastic damage evolution model [34]. The multiscale damage evolution model utilizes a finite element model to predict stress concentration factors (SCFs) around a single broken fiber within the composite. The SCFs are then used as inputs into a composite tensile simulation along with the continuous fiber strength distribution, matrix properties, and composite geometry. In the tensile simulation, Green's function is used to predict the stress state in the composite around multiple interacting fiber breaks. Under uniaxial tension loading, the tensile simulation identifies fiber segments which have exceeded their failure strength, redistributes the load once carried by the broken fibers into the composite, and tracks damage within the composite to predict ultimate strength. This tensile simulation can be used to predict the scatter in composite strengths by randomly assigning fiber strengths. Additionally, the tensile simulation was developed for matrix materials which are elastic-perfectly plastic which is a reasonable assumption for the Al-2Cu matrix material of interest in this work.

7.1 UNIAXIAL TENSION DAMAGE EVOLUTION

Tensile failure of unidirectional axial fiber reinforced composites occurs over many size scales specifically, the micro-, meso-, and macroscales [34]. Fiber reinforced composites have a random distribution of fiber flaw strengths based on the fiber's cumulative strength distribution. At the microscale, fiber defects initiate failure with cracks that propagate through the fiber cross

section and are arrested at the fiber/matrix interface. Crack arrest occurs only if sufficient energy is absorbed through debonding, yielding, and sliding [26]. Along the length of the broken fiber, debonding occurs if the fiber/matrix interface is weak enough to fail due to the high shear stress at the fiber/matrix interface. Local yielding occurs in the matrix close to the broken fiber absorbing a fraction of the failed fiber load. If a previously broken and debonded fiber is within the vicinity of the break then frictional sliding at the debonded fiber/matrix interface occurs. In a successful composite, debonding, sliding, and matrix yielding absorb enough energy to stop the crack from propagating past the fiber/matrix interface. If the crack does propagate into the matrix catastrophic failure is likely. At the macroscale, composite failure occurs when a critical cluster of fiber breaks develops and a catastrophic crack propagates through the sample.

Two main approaches are used to predict damage evolution: continuum damage mechanics and finite element methods. Continuum damage mechanics are applied at the macroscale level where composite damage and failure is represented by internal damage parameters. The internal damage parameters do not include details on the micro- and mesoscale mechanics mentioned above [26]. Finite element models are typically used at the microscale level to investigate local damage evolution, however, due to computational inefficiency these simulations are only performed on small composite sections. For these reasons, Xia, Curtin, and co-authors identified the need for a computationally feasible multiscale model which incorporates stochastic fiber properties, microscale fiber and matrix interactions, as well as macroscale damage evolution with an intent to predict composite tensile strength distributions [34]. Their approach uses a finite element model to define the stress state around a single broken fiber incorporating the complex local stress distribution information. Then, a tensile simulation is used at the microscale to assign stochastic fiber strengths and calculate composite stress distributions due to multiple fiber breaks. There are no fit parameters used with this approach, which only requires material properties, strength distributions, and geometry are required as inputs. A discussion of the tensile simulation is provided below and is referenced in numerous articles by Xia, Curtin and co-authors [26, 34-39].

7.2 Local Load Sharing Through Stress Concentration Factors

An important parameter in damage evolution modeling is how load is transferred within a composite when a fiber break occurs. Two main methods are used to quantify load transfer: shear-lag models (SLMs) and finite element methods (FEM). Shear-lag models are frequently used to estimate the stress state around broken fibers, due to their computational efficiency and accuracy for simple loading cases [36]. When fiber breaks occur, the matrix transfers stress to the near neighbor intact fibers through shear. Shear-lag methods assume fibers only carry axial stresses while the matrix carries purely shear stress [40]. In metal matrix composites the contribution of axial loads carried by the matrix during damage is significant and should not be excluded from the analysis. SLMs become less accurate than FEM for composites where debonding, interface yielding and or matrix yielding have a significant role in the damage response [36]. All of these failure modes are active in metal matrix composites especially matrix yielding which can be quantified using FEM stress concentration factors. For these reasons, a finite element model was used to determine stress concentration factors (SCF) for the metal matrix composite in this study.

The following section discusses specifics of the finite element simulation used in this work to determine composite stress concentration factors for a single fiber break. An implicit 3-dimensional Abaqus 6.10 model was developed to represent a uniaxial fiber reinforced composite section with hexagonal fiber packing. Taking advantage of the hexagonal symmetry, only a 30° composite wedge was modeled. The composite wedge consists of a central fiber, which will be broken, and the 11 nearest neighbor intact fibers. A 60% fiber volume fraction was used and is similar to the measured volume fraction for the unidirectional composite, Table III. A Nextel™ fiber radius of 6 μm and the 60% fiber volume fraction defined fiber spacing within the model. The composite section is 600 μm long ensuring the applied loading, achieved using a displacement boundary, is far away from the plane of the break and the broken fiber stress is fully recovered in the model. Fibers were defined as elastic materials with a modulus equal to the fiber type simulated 3,000 or 10,000 denier Nextel™ 610 and a Poisson's ratio of 0.22. The Al-2Cu matrix was considered to be elastic-perfectly plastic, to be consistent with the tensile simulation. Property inputs included modulus, Poisson's ratio, and yield stress which were

measured in this work and reported in Section 4.5. Figure 39 shows the unidirectional composite model geometry, cylindrical coordinate system, and symmetry boundary condition on the wedge faces ($u_\theta = 0$). Another hexagonal symmetry boundary condition exists at the point of the composite wedge. There is no radial displacement for the composite wedge for all values of z at $r = 0$ and $u_r = 0$. The mesh used in this FEM simulation, shown in Figure 40, incorporates a finer mesh near the broken fiber. Simulation of the fiber break is performed in two steps: loading and breaking. During the loading step, the bottom of the model ($z = 0$) is fixed with the boundary condition $u_z = 0$. Then, a uniform displacement is applied to the top surface ($z = 600$ μm) of the model, $u_z = 3.33$ μm. This displacement corresponds to an applied composite axial stress of 1,320 MPa. In the second loading step, breaking, the fixed boundary condition on the central fiber is released simulating a fiber break. The center fiber's axial displacement before and after the break is displayed in Figure 41. For this model, the displacement due to breaking at the center of the broken fiber was 0.78 μm. Stress concentration factors are defined as the ratio of average axial stress within the breaking plane on a fiber after and before the break. The broken fiber SCF is zero at $z = 0$ because after the break the broken fiber load is reduced to zero within the plane of the break. Figure 42 displays how stress was distributed to the 11 intact fibers in the composite wedge when the center fiber broke. Intact fibers further away from the break had a slight increase in stress while fibers closest to the break carried the majority of the broken fibers stress. Stress concentration factors as a function of their distance away from the broken fiber are shown in Figure 43. The normalization distance is the distance between the first and second fiber centers or the hexagonal packing fiber spacing. The first nearest neighbor fiber to the break will see a 2% increase in stress due to the fiber break. The SCFs, within the plane of the break, are used as inputs into the tensile simulation. For consistency between the tensile simulation and the stress concentration factors, the FEM loading stress and the simulation strengths should be in agreement. Since the FEM SCFs are calculated first, they are input into the tensile simulation, and used to predict composite strength. If the predicted composite strength is not similar to the FEM applied stress the SCFs should be recalculated at the new simulation stress. This iterative process should be performed until both the SCF applied axial stress and the predicted composite strength are in agreement. Two iterations of this process were needed in this study for the tensile simulation, discussed below.

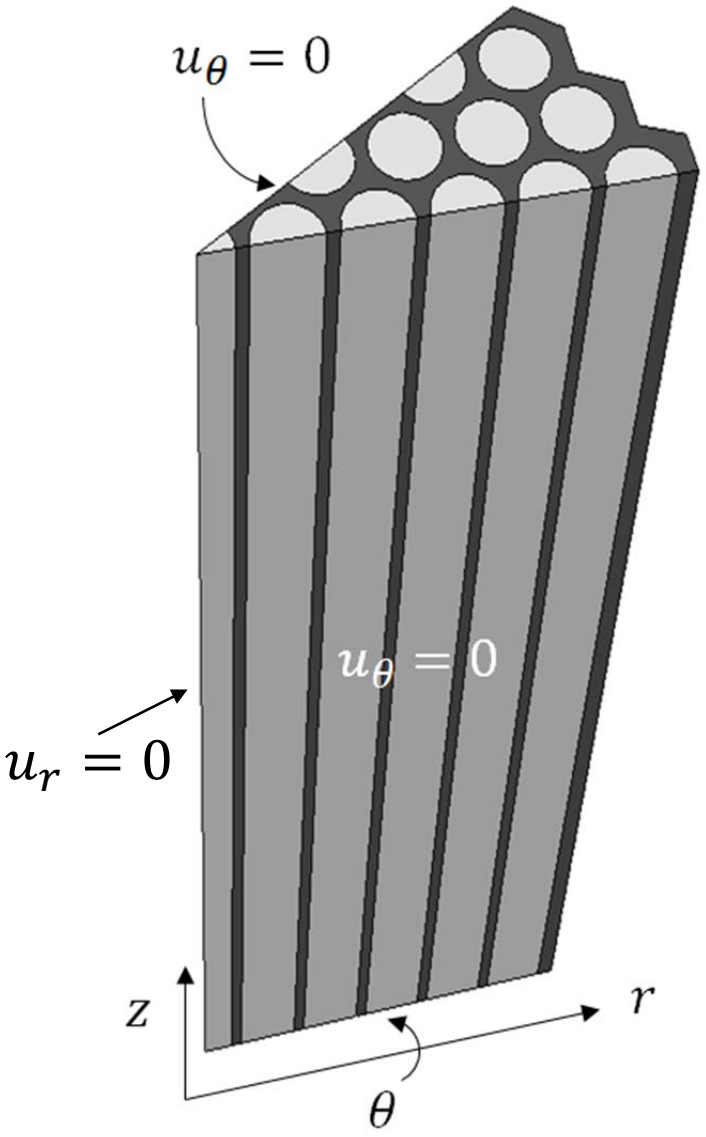

Figure 39. Unidirectional composite finite element model geometry and hexagonal symmetry boundary conditions.

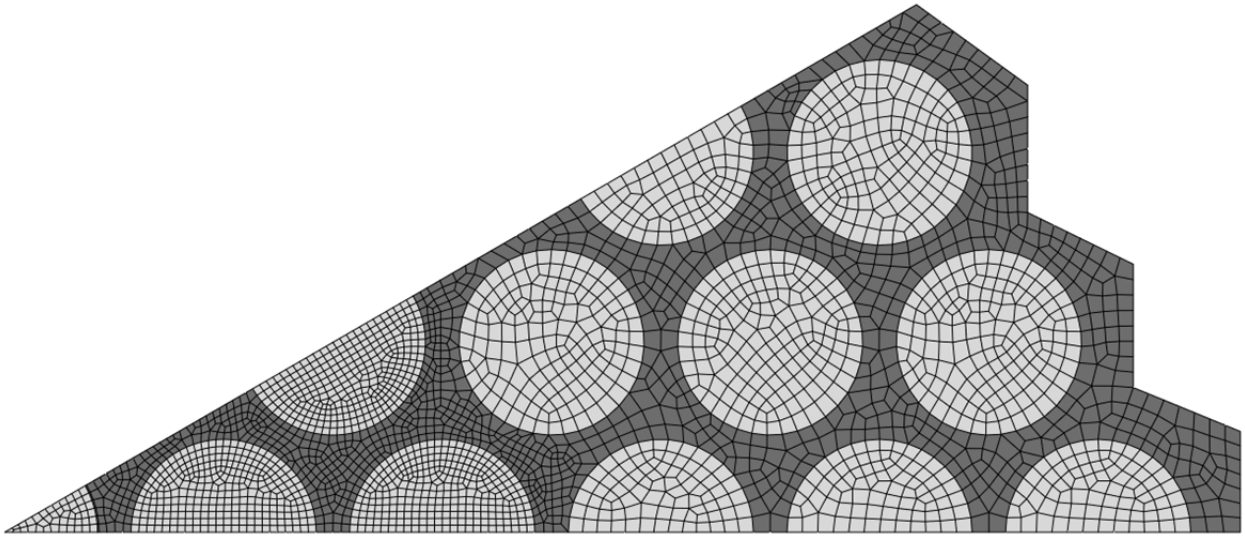

Figure 40. Mesh used to calculate SCFs with a finer mesh near the breaking center fiber.

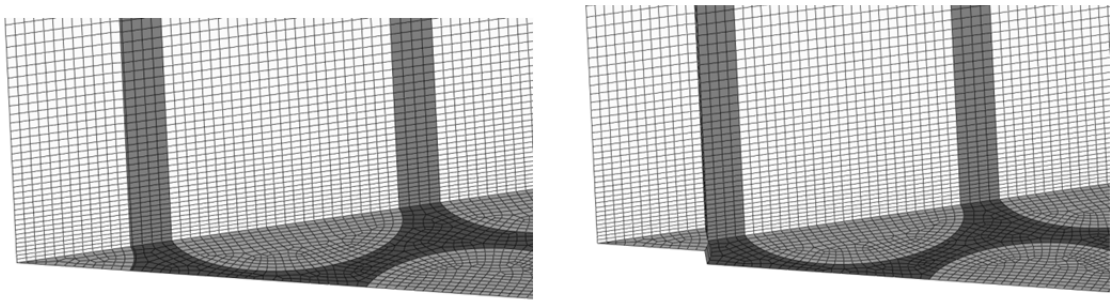

Figure 41. Center broken fiber displacement before (left) and after (right) the simulated break.

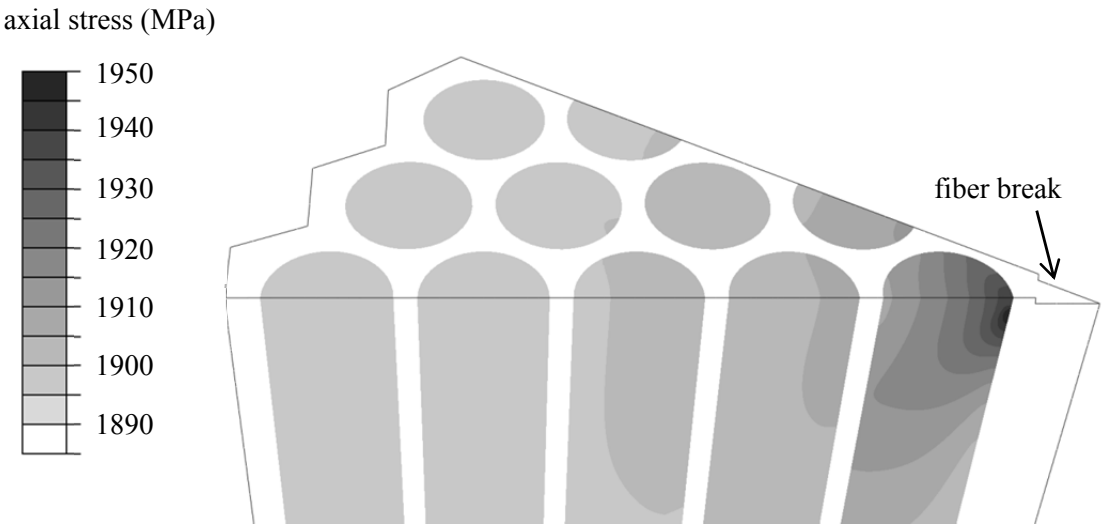

Figure 42. Composite stress redistribution after simulated fiber break.

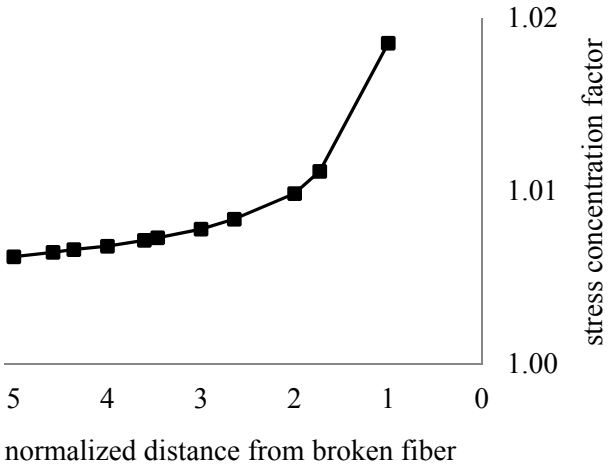

Figure 43. Stress concentration factors within the plane of the break.

7.3 Stochastic Damage Evolution Simulation

The second step in implementing Xia and Curtin's mulitscale approach is the stochastic damage evolution simulation for a 3D composite referred to here as the composite tensile simulation [26, 34-39]. The tensile simulation takes the FEM SCFs for a single break and calculates the composite response for multiple interacting fiber failures. This mesoscale level model consists of an array of continuous fibers sectioned into lengths much smaller than their stress recovery length l_f, defined in Equation 7 [41]. Each fiber length is assigned a failure strength according to the fiber CDF or fiber Weibull parameters, obtained in Section 6.3. The stress recovery length refers to the length required for a broken fiber to return to the applied far field fiber stress. In the tensile simulation a linear stress recovery assumption was made to recover stress along the fiber length. Since the stress recovery happens over many fiber segments, until the full field fiber stress is achieved, the nearest neighbor fibers see an increase in stress along their fiber length as well to satisfy equilibrium. To be clear, the intact fibers see an increase in stress within the plane of the break, defined by the SCFs, and along their length in planes perpendicular to the break plane until the broken fiber stress is fully recovered.

In the simulation, load is incrementally applied to the composite until the strength of the weakest fiber segment strength is reached and a fiber failure occurs. Then, the load once carried by the broken fiber is redistributed within the break plane to neighboring intact fibers, based on the

SCFs. Out of the breaking plane the broken fiber gradually increases load until it reaches the far field applied stress at the recovery length. Due to the decrease in load carried by the fiber along the axial length, the neighboring fibers also see an increase in load along their length. Load transfer in planes perpendicular to the break is performed by ensuring equilibrium is satisfied in each individual plane. If multiple breaks occurred during the load increment one of the breaks is randomly chosen and stress is redistributed then the next break is addressed until all breaks have been redistributed to intact fibers. In some instances, two neighboring fibers break in the same increment or redistribution from a broken fiber causes a near neighbor fiber segment to fail. In these cases, the simulation uses the single break FEM SCFs to calculate Green's function for multiple breaks as part of the simulation algorithm. For a similar composite with a higher aluminum yield stress of 100 MPa, Xia and Curtin have reported the difference between the stress concentration factors determined using a FEM solution and Green's function calculation for a cluster of seven breaks, Figure 44 [34]. Green's function over predicts the SCFs at fibers close to the broken cluster because they are based on the single break SCF and the additional matrix hardening, which occurs during a cluster of break is not included. Further away from the break, Green's function predicts SCFs lower than the FEM. Although the two methods are not exactly the same, they only differ slightly by about 5% for the near and far intact fibers. This SCF error is reasonable when considering the amount of time necessary to calculated all possible breaking scenarios using the FEM method. In this work, the FEM took on average 3 hours to solve for the SCFs of one fiber break in a 12 fiber composite with a 600 μm length. The tensile simulation, consisting of 1024 fibers at 88.9 mm lengths, solves for hundreds of fiber breaks using Green's function and predicted composite failure within one minute. In the tensile simulation, once every break is detected at an applied stress level and load is redistributed the applied stress level is increased and the algorithm continues to solve until 20% of the fibers within a plane are fractured resulting in the composite strength. Ultimate failure is chosen to be at 20% because at this stage the composite is in cascading failure and additional failures do not appreciably increase the calculated composite strength, Figure 45.

$$l_f = \frac{r_f E_f \sigma_c}{2 \tau E_c} \qquad 7$$

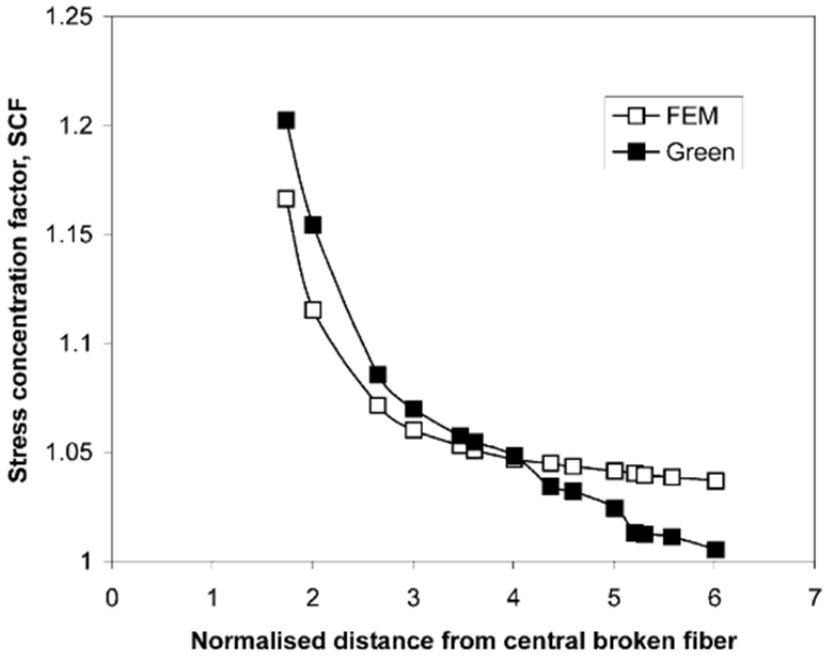

Figure 44. Stress concentration factors calculated using FEM and Green's function solution for a cluster of seven fiber breaks, from Xia and Curtin [34] figure 8 with permission by Elsevier see Section 11.3.

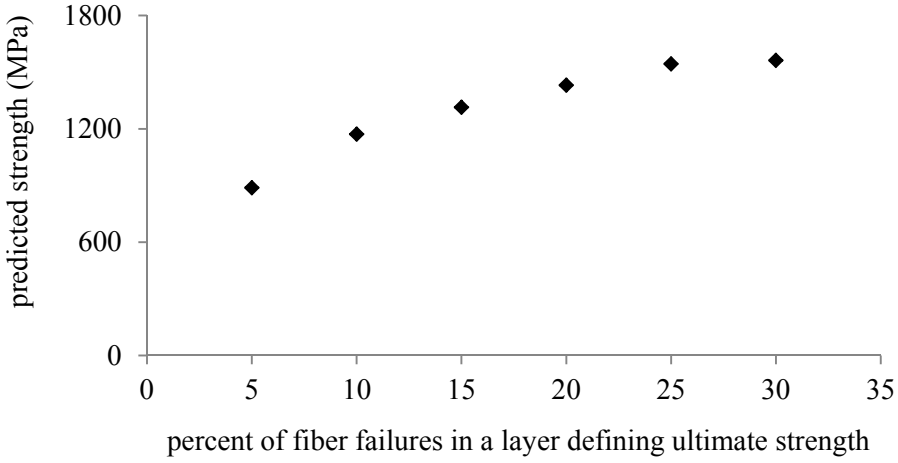

Figure 45. Percent of fiber failures within a simulation layer defining ultimate strength and the effect on predicted strengths.

7.4 Continuous Composite Strength Prediction

To apply Xia and Curtin's tensile simulation to the unidirectional composite of interest in this work, material properties and geometries were modified in the tensile simulation FORTRAN code kindly provided to the author by William Curtin. Inputs included geometry, fiber CDF (Weibull parameters), and matrix properties. As one example, the simulation inputs and results discussed here used the unprocessed 3,000 denier Nextel™ 610 fiber population as inputs. The simulation was performed for all of the Nextel™ 610 populations characterized in Section 6.4. A unidirectional composite consisting of 256 continuous fibers in a hexagonal array with total lengths of 88.9 mm, similar to the composite tensile test coupons, was simulated. Each fiber was sectioned into 20 μm lengths for a total of 4445 layers. A 20 μm section length is smaller than the composite recovery length of $l_f = 266$ μm. Fiber radius, Weibull modulus, Weibull strength, and Weibull length were required inputs which can be found in the single fiber tension test results section. Additional inputs include composite volume fraction $V_f = 60\%$ and the interfacial shear stress $\tau = 21.9$ MPa, is assumed to be roughly equal to the 57% of the matrix yield stress $\sigma_y = 38$ MPa, Equation 8. Catastrophic failure or the composite tensile strength was achieved when the model had 57 broken fiber segments within a layer. Since Green's function simulation uses a stochastic fiber strength distribution, i.e. fiber segment strengths are randomly assigned, every simulation iteration results in a different strength. Repeating strength predictions many times (approximately 100) will result in a prediction of the composite strength distribution similar to the fiber strength distributions characterized in Section 6.4. To obtain an average composite strength 10 tensile simulations are performed and averaged. Weibull's theory applies to composite strengths including composite length scaling. At smaller lengths fewer clusters of weak fiber segments are probable and therefore the composite has a higher strength. A study of composite length effects on the tensile simulation is shown in Figure 46. For sufficiently long lengths ~88.9 mm, the simulation strength begins to plateau.

$$\tau \approx \sigma_y/\sqrt{3} \qquad 8$$

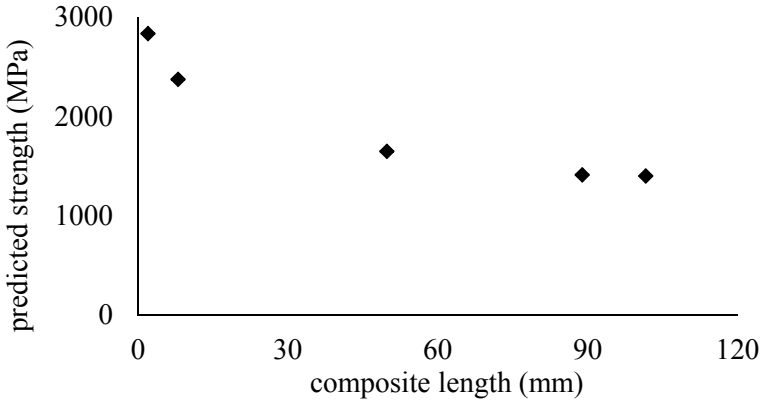

Figure 46. Unidirectional composite tensile simulation strength predictions at various composite lengths.

Using these inputs and the SCFs from the FEM with an applied stress of 1320 MPa the average extracted Nextel™ 10,000 unidirectional composite strength averaged over 10 simulations was 1343 MPa. There is a 2% difference between the SCF applied stress and the simulation results. As discussed above, it is important to have SCFs that are representative of local stress distribution when a break occurs. If the simulation is performed and the SCF applied stress does not align with the simulation strength the SCFs must be recalculated. Initially, SCFs were calculated using an applied stress of 2000 MPa which resulted in simulation strengths of 1411 MPa. Since the SCF applied stress and simulation strength were not similar, a second FEM model was solved with an applied stress of 1320 MPa. This was the final iteration between the tensile simulation and SCF model since the strength results are within 2% of each other.

Two main assumptions were made in the tensile simulation: 1) τ is constant along the recovery length of the broken fiber and is equal to $\sigma_y/\sqrt{3}$, 2) axial stress in the broken fiber recovers linearly to the far field fiber stress. In their study, Xia and Curtin plot the interfacial shear stress along the length of the broken fiber which reproduced in Figure 47 [34]. For low matrix yield stresses (50 MPa in their study) this assumption is accurate within the broken fiber's stress recovery length. Their SCF FEM model (Figure 47) had a 27 MPa interfacial shear stress while a value of $\tau = 27.8$ MPa was used in the tensile simulation. These values are similar making the tensile simulation assumption of $\tau = \sigma_y/\sqrt{3}$ appropriate. Figure 48 is a plot of the axial stress along the length of the broken fiber from the SCF FEM model and the assumed behavior within the tensile simulation. In Xia and Curtin's tensile simulation the linear stress recovery

assumption was based on a shear lag theory [41]. Both the SCF FEM model and shear lag model have similar behaviors except for distances near the recovery length, l_f. The tensile simulation linear stress recovery assumption does a good job at capturing the broken fiber recovery.

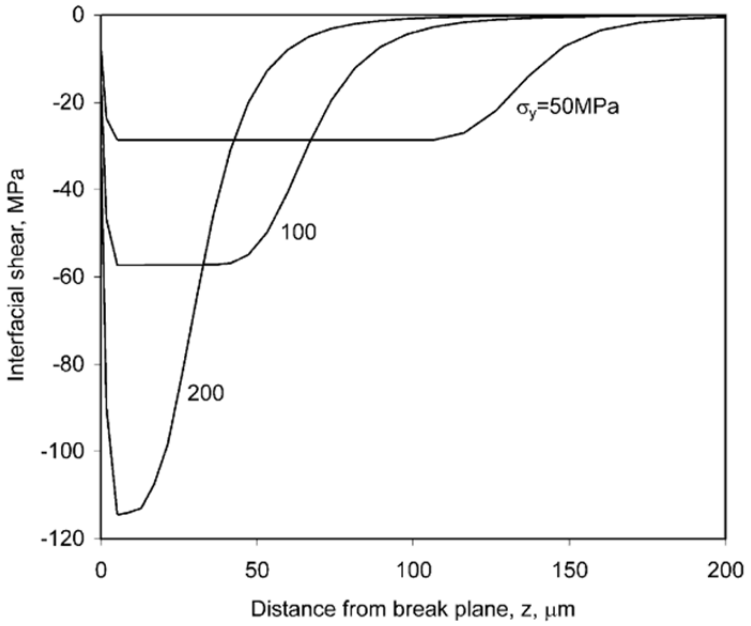

Figure 47. Interfacial shear stress along the length of the broken fiber from Xia and Curtin [34] figure 2 with permission from Elsevier, see Section 11.3.

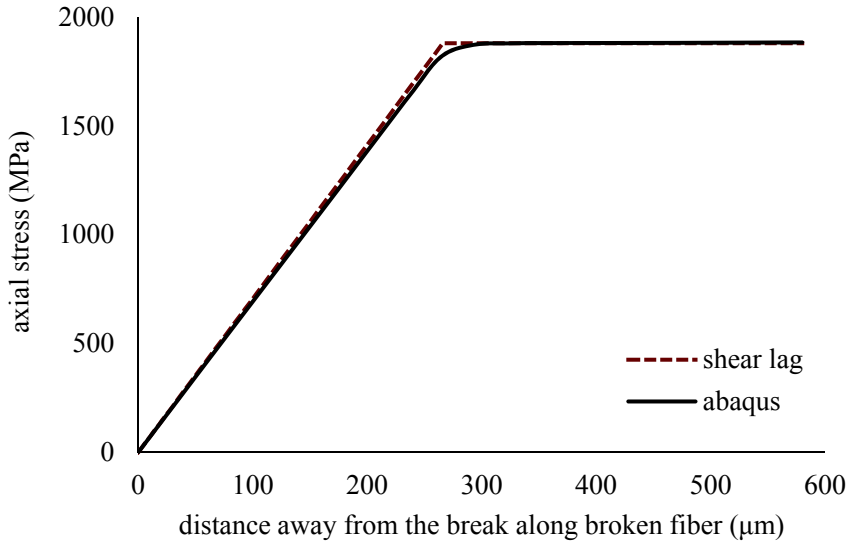

Figure 48. Abaqus axial stress along the broken fiber and the tensile simulation shear lag assumption representation.

The tensile simulation directly predicts the unidirectional composite strength. Strength predictions were computed for both unprocessed and extracted unidirectional fiber populations. Simulated and experimental strengths are reported in Figure 49. Tensile strength predictions were also performed using Wilson [28] and Gonczy et al. [27] fiber properties. Referenced properties predicted composite strengths 50% higher than the experimental results for the unidirectional composite. The extracted unidirectional fibers predicted a composite strength of 1430 MPa within 10% of the measured strength while the unprocessed fiber prediction was 1700 MPa within 30% of the composite strength. The extracted fiber prediction resulted in an improved estimate of the composite strength than the unprocessed and literature fiber property predictions.

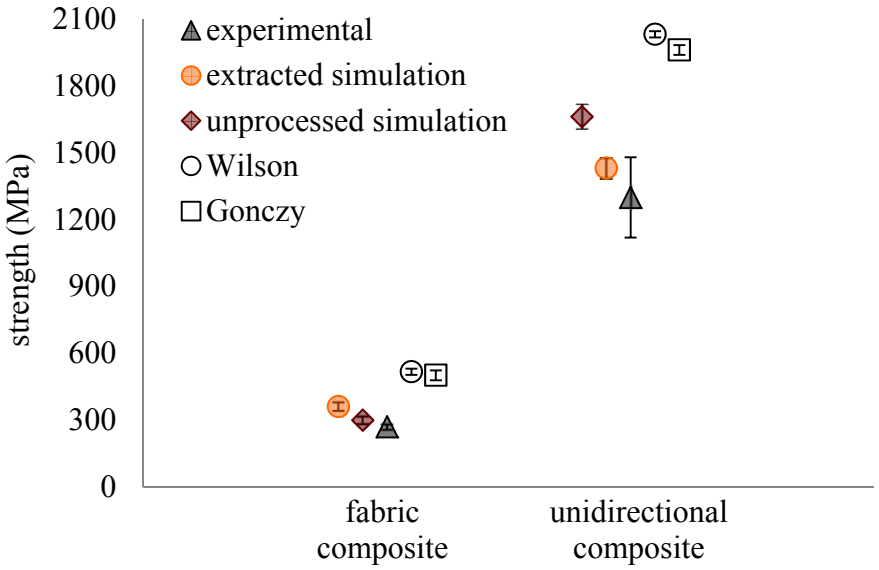

Figure 49. Measured and simulated composite strengths.

7.5 Fabric Composite Strength Prediction

The fabric composite's complex fiber geometry required additional calculations after the initial strength prediction to determine composite strength. The fabric composite consists of axial reinforcement, transverse reinforcement, and open matrix regions within the cross section, Figure 50. Locally, within an axial fiber bundle, the fibers behave similarly to the axial fiber reinforced composite with a 60% volume fraction while the overall fabric composite volume fraction is 22%. Fabric fiber properties were input into the tensile simulation with a 60% volume fraction to simulate the strength of the axial fiber bundle. Then an area analysis was performed on cross sectional images of the fabric composite to determine what fraction of the composite consists of axial reinforcement, transverse reinforcement, and neat matrix. The overall composite strength (X_c) was calculated following Equation 9.

$$X_c = A_{uni}X_{uni} + A_{trans}X_{trans} + A_{matrix}\sigma_y \qquad 9$$

In the above equation X represents strength values, A is the area fraction of each composite type within the sample, and σ_y is the matrix yield strength. The FEM which calculated SCFs for the axial bundle used an elastic-perfectly plastic material model for the aluminum matrix. To be consistent with the simulation, the maximum stress the neat aluminum could carry was equal to the yield strength of the matrix material. Following this procedure fabric composite strengths were predicted and plotted in Figure 49. The extracted fiber simulation results were within 11% or 30 MPa of the experimental strength while the unprocessed fiber strength prediction was 34% higher than the experimental results. Strength predictions using Wilson [28] and Gonczy et al. [27] fiber properties predicted composite strengths 90% higher than the experimental results. Similar to the unidirectional composite the extracted fiber strength predictions produce an improved estimate of the composite strength than the literature or unprocessed fiber predictions.

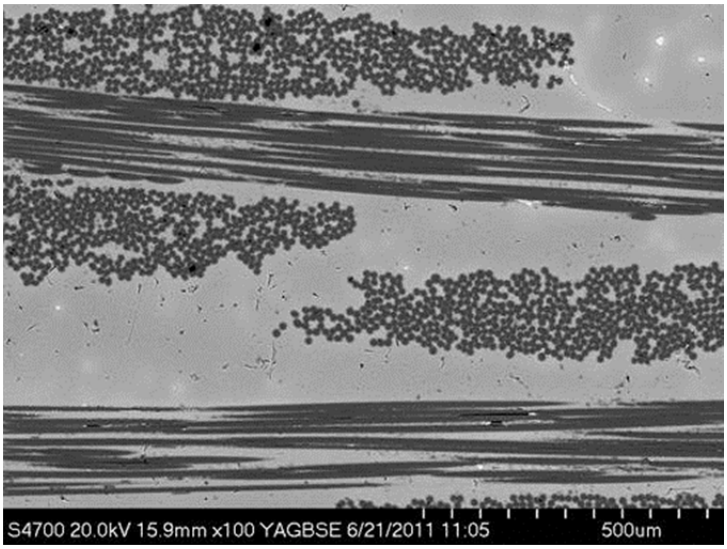

Figure 50. Fabric composite cross section consisting of axial and transverse fibers [23].

7.6 Strength Prediction Discussion

The improvements in strength prediction for the extracted fiber properties indicate damage during processing does have an effect on composite predictions. A 15% decrease in fiber properties was measured due to fiber damage during processing. When possible, extracted fiber properties should always be chosen over unprocessed fiber properties to be used as modeling inputs. When comparing the unprocessed fiber properties, measured in this work, to the literature fiber properties available, significant differences in average strengths and strength distributions were seen. A lower average strength and larger strength distribution fiber population was measured. The fiber property distribution reported by Wilson in 1997 [28] is still commonly cited and used to represent Nextel™ fiber strengths. Due to the number of fiber tests required to quantify the population it isn't surprising these experiments are not often repeated. The initial motivation behind this study was to measure all inputs necessary for the modeling approach. Xia and Curtin's tensile simulation used no fit parameters. Inputs only include material properties and geometry making this simulation a great way to quantify the effect as-processed fiber properties have on composite strength predictions. Strength predictions using the as-processed (extracted) fiber properties were within 10% of the experimental results. Measured unprocessed fiber properties and literature fiber properties resulted in 30% and 92% difference respectively, between the predicted composite strengths and experimental results.

8 HYBRID COMPOSITE SIMULATION

In an effort to gain a better understanding of the mechanics at work in the hybrid sample, a uniaxial tension hybrid simulation in Abaqus was performed on the 65P and 65P Inverted hybrids. These two samples were chosen since they exhibit the most interesting ductile type failure, with load gradually decreasing after cracking, unlike the other hybrids which have large drops in load during failure. Both the Saffil® paper and Nextel™ fabric property assignments and failure will be defined using an elastic-plastic material model with an Abaqus ductile damage definition.

8.1 NEXTEL™ FABRIC COMPOSITE

During tensile testing of the 65P $[N/P]_s$ samples, cracks were forming on the sample surface while the sample continued to carry load. Each crack resulted in about a 10% drop in load after which the sample continued to increase load again. One, two, or three full cracks (through the width and thickness of the Nextel™ layer) were present on each sample surface. There was no correlation between the number of visible fabric cracks and the number of reloading portions of the axial stress-axial strain curve. Due to the visible cracking behavior it was hypothesized that the Nextel™ fabric sections were failing, transferring stress into the Saffil® layer and back into the Nextel™ layer away from the crack. If stress was not transferred back into the Nextel™ layer the sample load would have dropped substantially and would have been similar to the Saffil® paper layer behavior. Cracks were between 1.0 mm and 5.5 mm apart, comparable to the fabric weave spacing. In Figure 8 (repeated below for convenience) the smallest spacing between transverse rows on two adjacent axial fiber tows is 1.5 mm. The largest spacing exists along one axial tow and is approximately 5.5 mm. The transverse tow spacing is significant since the transverse composite has a significantly lower failure strain than the unidirectional composite, Figure 12 (repeated below). The fabric composite has a failure strain between the unidirectional and transverse composites. Based on this crack spacing and fabric geometry the hybrid finite element model consists of stacked Nextel™ fabric composite segments, each 1.5 mm long, joined to a 25.5 mm long Saffil® section. Fabric composite axial stress-axial strain curves were obtained using a similar approach as Section 7.5. One-hundred fabric unidirectional composite

axial stress-axial strain curves at 88.9 mm were predicted using Xia and Curtin's tensile simulation. In Section 8.3, only strengths were taken from the tensile simulation, here the applied stress and strain were printed to a text file at each stress increment during the simulation resulting in unidirectional bundle stress strain curves. Unlike the fabric composite prediction with 4 layers of fabric, in this instance only one layer of fabric needs to be predicted. To achieve this fabric layers were isolated in the polished cross section image and the percentage of unidirectional composite bundle, transverse bundle and matrix rich regions were calculated. The single layer fiber volume fraction is about 27% while the 4 layer fabric composite volume fraction is 22%. The difference in volume fraction is due to manufacturing constraints, there are a finite number of mold sizes available and if the reinforcements are not tightly packed, matrix rich regions will fill in the space decreasing the overall composite volume fraction. Area averaging was implemented to obtain fabric composite axial stress-axial strain curves. For each strain output of the unidirectional bundle simulation, a similar strain was found in the transverse experimental and Al-2Cu experimental curves. Area averaging of the unidirectional simulation bundle, transverse and matrix stresses was then performed at each matched strain. This procedure resulted in 100 different simulated fabric composite axial stress-axial strain curves at a composite length of 88.9 mm or 4445 layers in the simulation. A comparison of the experimental 22% and simulated 22% and 27% volume fraction fabric composite behavior is shown in Figure 51. The tensile simulation fabric composite behavior is similar to the experimental results except for over predicting failure properties. The simulation predicts higher strengths and failure strains than the experimental data. Also plotted in Figure 51 is the predicted one layer (27% V_f) fabric composite behavior.

Predictions were performed at an 88.9 mm composite length to compare with the experimental results and to be able to perform appropriate area averaging of the stress strain curves. To obtain stress levels at the 1.5 mm scale Weibull scaling was implemented as discussed in Section 6.3. To use Weibull scaling the Weibull parameters need to be calculated. The strengths of each simulated single layer reinforced fabric composite stress strain curve were obtained and the resulting Weibull modulus was 46.2 with a Weibull strength of 342 MPa at a characteristic length of 88.9 mm, Figure 52. Next, the simulation stresses were scaled to a 1.5 mm characteristic length using Equation 6 at each strain in the stress strain curve.

Abaqus inputs are in terms of true stress and logarithmic strain calculated using Equations 10 and 11 using uniaxial simulation data. In these equations σ_{eng} and ε_{eng} are the axial stress and axial strain from the measured or simulated uniaxial tension stress-strain curves. This conversion for true stress and logarithmic strain is appropriate when a material has large inelastic strains or a yield stress that is orders of magnitude less than the elastic modulus, E. The fabric composite has a yield stress of 50 MPa and an elastic modulus of 125 GPa satisfying this condition. The Abaqus ductile damage evolution model was used to describe decay of the fabric properties after reaching the simulated failure strain of each segment. Inputs for the ductile damage module include the plastic failure strain which initiates damage, the triaxiality stress, and strain rate. For each fabric segment the plastic strain to initiate damage is set equal to the failure strain of the section, the stress triaxiality was 0.324, and the strain rate was set equal to 0.001 s^{-1} (the uniaxial composite tension test rate). An element is deleted when it reaches a displacement of 0.0045 μm approximately equal to the displacement required to unload the element at a strain similar to the segment failure strain after the damage criteria is met.

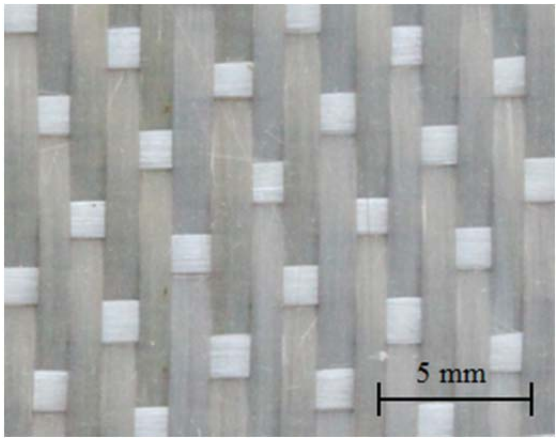

Figure 8. 8-harness satin weave Nextel™ fabric desized.

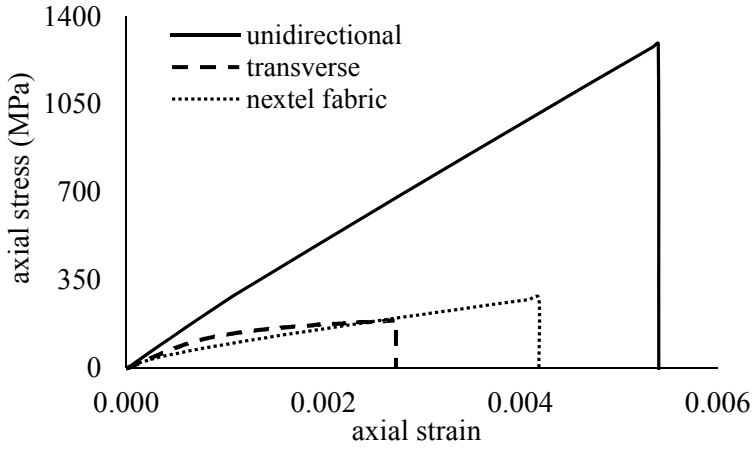

Figure 12. Nextel™ unidirectional (0°), transverse (90°) and woven fabric (0°/90°) continuous fiber reinforced composites.

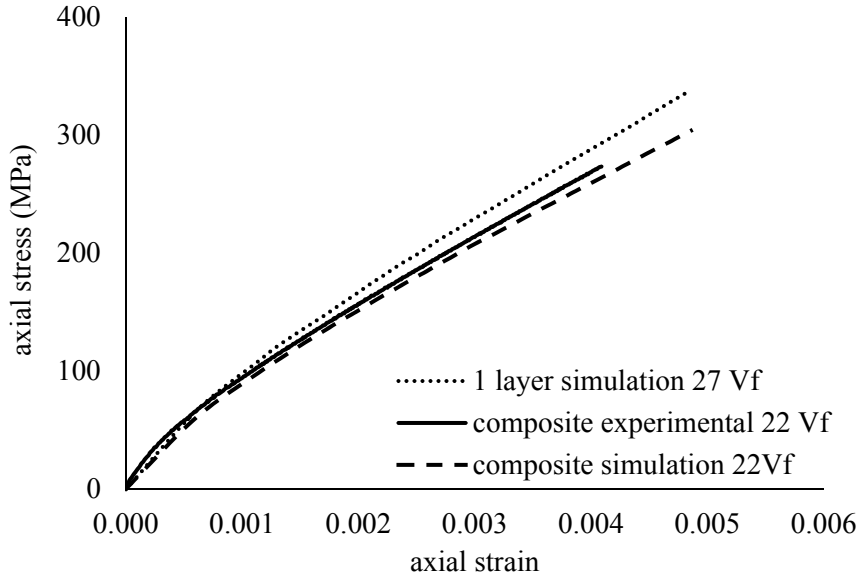

Figure 51. Tensile simulation prediction of composites with one and four fabric layers as well as the four layer composite experimental results.

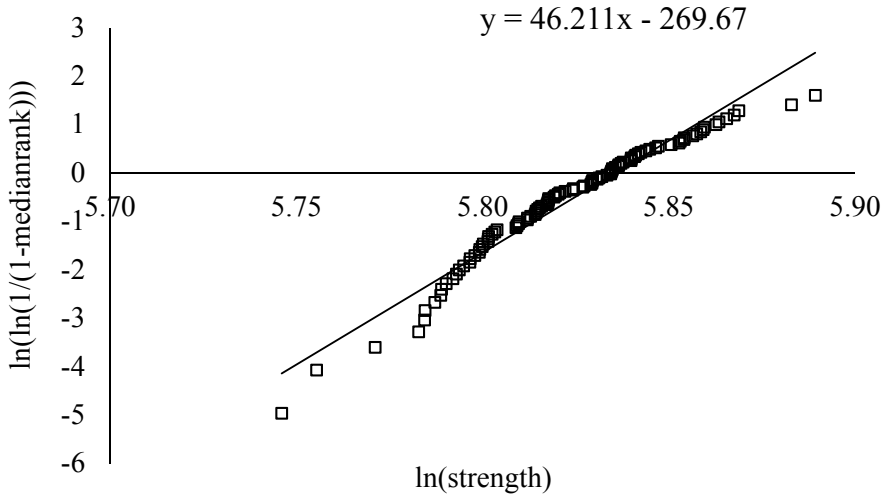

Figure 52. Single layer fabric composite 27 V_f simulated strength distribution in the form of a Weibull plot.

$$\sigma_{true} = \sigma_{eng}\left(1 + \varepsilon_{eng}\right) \quad 10$$

$$\varepsilon_{ln}^{plastic} = \ln\left(1 + \varepsilon_{eng}\right) - \frac{\sigma_{true}}{E} \quad 11$$

A small Abaqus model was used to check if these inputs return the desired fabric composite axial stress-axial strain behavior. The fabric model consists of three fabric segments each 1.5 mm long with randomly assigned properties from the predicted fabric strength distribution. The model geometry is rectangular with a 0.494 mm width, equal to the thickness of one fabric composite layer, and 4.5 mm high. A two dimensional plane stress model was used with four-node plane stress reduced integration elements of type CPS4R. As indicated in the Abaqus user manual, solution of a ductile damage problem should be done using the unsymmetric equation solver because the material Jacobian matrix will be unsymmetric once damage evolution is triggered. Additionally, these solutions are unstable due to the stiffness degradation at the onset of damage and to help with convergence difficulties viscous regularization should be included with the element definition. Boundary conditions on the rectangular two-dimensional model include a fixed bottom edge and a displacement applied to the top surface simulating a uniaxial tension test. Figure 53 shows the response of the fabric section when one of fabric sections fails resulting in failure of the composite. The model predicts fabric strains slightly lower than the tensile

simulation prediction. The response of a fabric element which has failed is plotted in Figure 54 along with the element assigned true stress-true strain material properties. As shown, once the element failure strain is reached the element gradually unloads until reaching the assigned full failure strain (prescribed as a displacement to minimize mesh size effects).

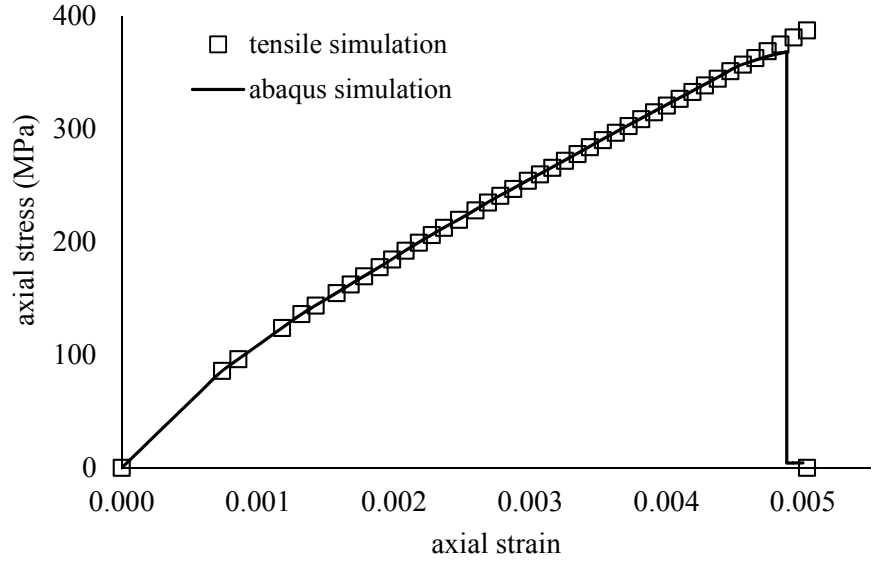

Figure 53. Fabric composite tensile simulation and Abaqus ductile damage simulation response to uniaxial tension.

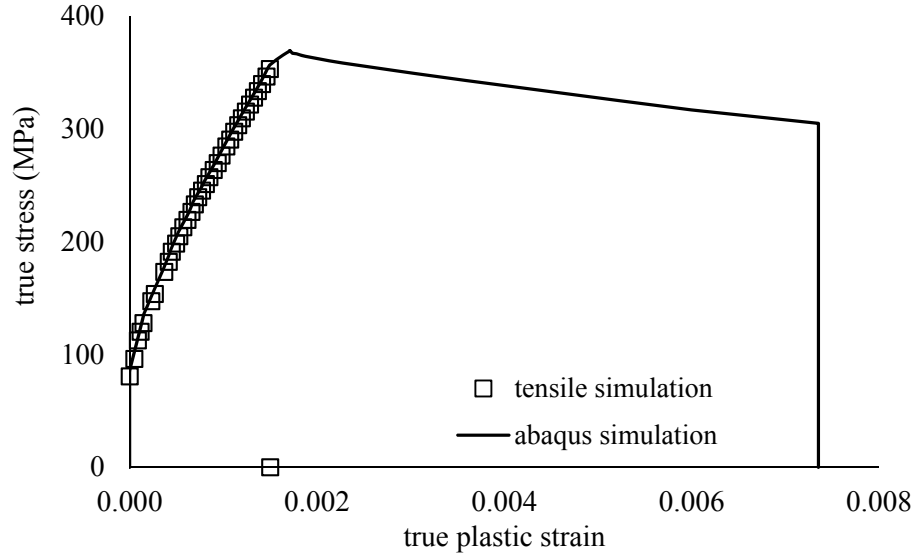

Figure 54. Fabric composite tensile simulation inputs into Abaqus and the ductile damage response of a fabric element after damage initiation is triggered.

8.2 SAFFIL® PAPER COMPOSITE

A similar approach is used to determine and check the inputs for the paper composite ductile damage model. Only one paper section will be prescribed in the hybrid model since Saffil® cracking does not seem to be controlling hybrid behavior. The paper model is 1.04 mm wide (similar to the thickness of one Saffil® paper composite layer) and 25.5 mm long. In Figures 55 and 56, the uniaxial stress strain curve and element response using the ductile damage model are similar to the experimental Saffil® paper results. Reasonable uniaxial tension predictions of the fabric and paper composites were obtained using the ductile damage evolution model. Next, a hybrid model consisting of both composites and their interaction with each other in uniaxial tension will be addressed.

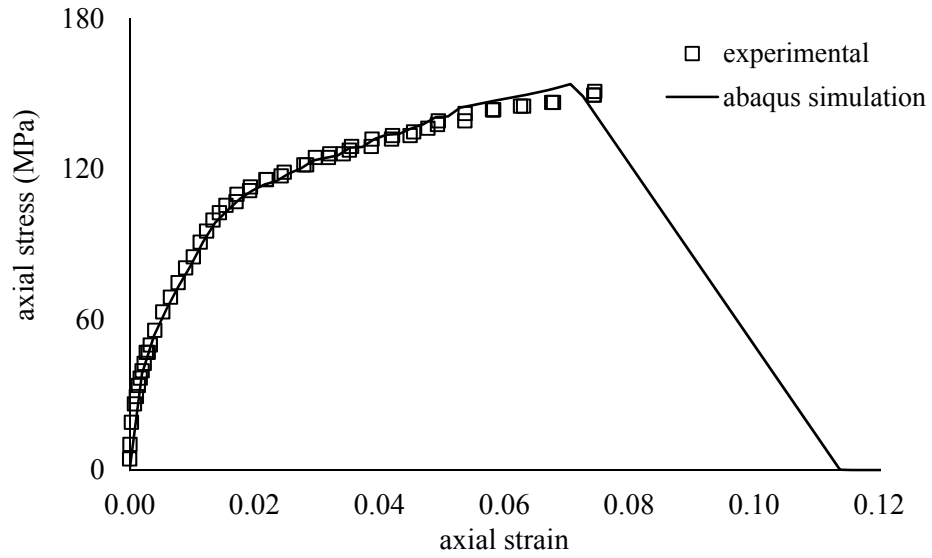

Figure 55. Saffil® paper composite axial experimental and ductile damage material model representation.

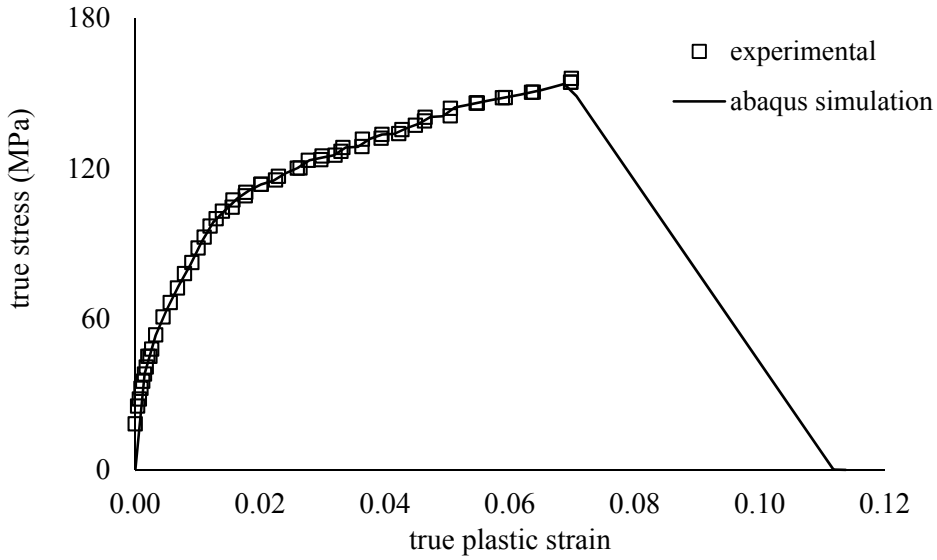

Figure 56. Saffil® paper Abaqus inputs and the response of a failed Saffil® paper element in the simulation.

8.3 Hybrid Composite Simulation

A gradual unloading behavior was observed in hybrid composites 65P and 65P Inverted. The only difference between these two composites is their lamination scheme with 65P having outer and 65P Inverted having inner fabric layers. As a first attempt, to begin understanding the complex stress transfer between layers in the hybrid, a hybrid ductile damage model was used. Material properties and geometries are the same as the fabric and paper descriptions above. Each fabric composite section has dimensions of 0.494 mm x 1.5 mm while dimensions for the paper composite section are 1.05 mm x 25.5 mm. There are a total of 17 fabric segments in each hybrid model which were randomly assigned failure properties based on the fabric composite tensile simulation strength distribution. For the simulations shown here, both the 65P and 65P Inverted have the same Nextel™ section assignments for comparison purposes. The boundary conditions for both models are identified in Figure 57. A half model was used taking advantage of the lamination symmetry about the x-axis. To check for convergence 420, 612, and 1224 element solutions were obtained. The 612 and 1224 solutions returned similar axial stress-axial strain behavior and therefore the 612 element solution was used for computational efficiency.

Mises stress contours at defining points in the composite response in the hybrid 65P are presented in Figure 58. The contour in image (a) is at the peak strain of the two fabric elements about to fail (orange), (b) represents the stress contour one increment after (a) when parts of the weakest (lowest assigned failure strain) fabric section have failed. At this point the fabric layer unloads and locally distributes stress into the Saffil® layer near the broken segment. Contour (c) displays the stress state right as damage is being initiated in the Saffil® layer and shortly after the Saffil® section has fully cracked and ultimate failure of the hybrid has occurred (d). Similarly, Figure 59 displays Mises stress contours for hybrid 65P Inverted. Each contour is taken at the same damage states described for 65P. Comparing the two hybrids, the fabric section in hybrid 65P Inverted has more failed elements than in 65P. As a result more load is transferred into the Saffil® layer once failure occurs (b) indicated by a larger high stress band in the Saffil® layer. After failure of the Nextel™ elements has happened (b) the Nextel™ layer carries a higher stress than in hybrid 65P. Once damage begins entering the Saffil® layer in (c) hybrid 65P has additional fabric sections near failure, indicated by the orange elements above and below the broken fabric section. 65P Inverted has no high near failure fabric elements at this point of failure. Failure of the Saffil® layer was banded in laminate 65P while 65P Inverted showed a large section of unloaded/failed Saffil® elements.

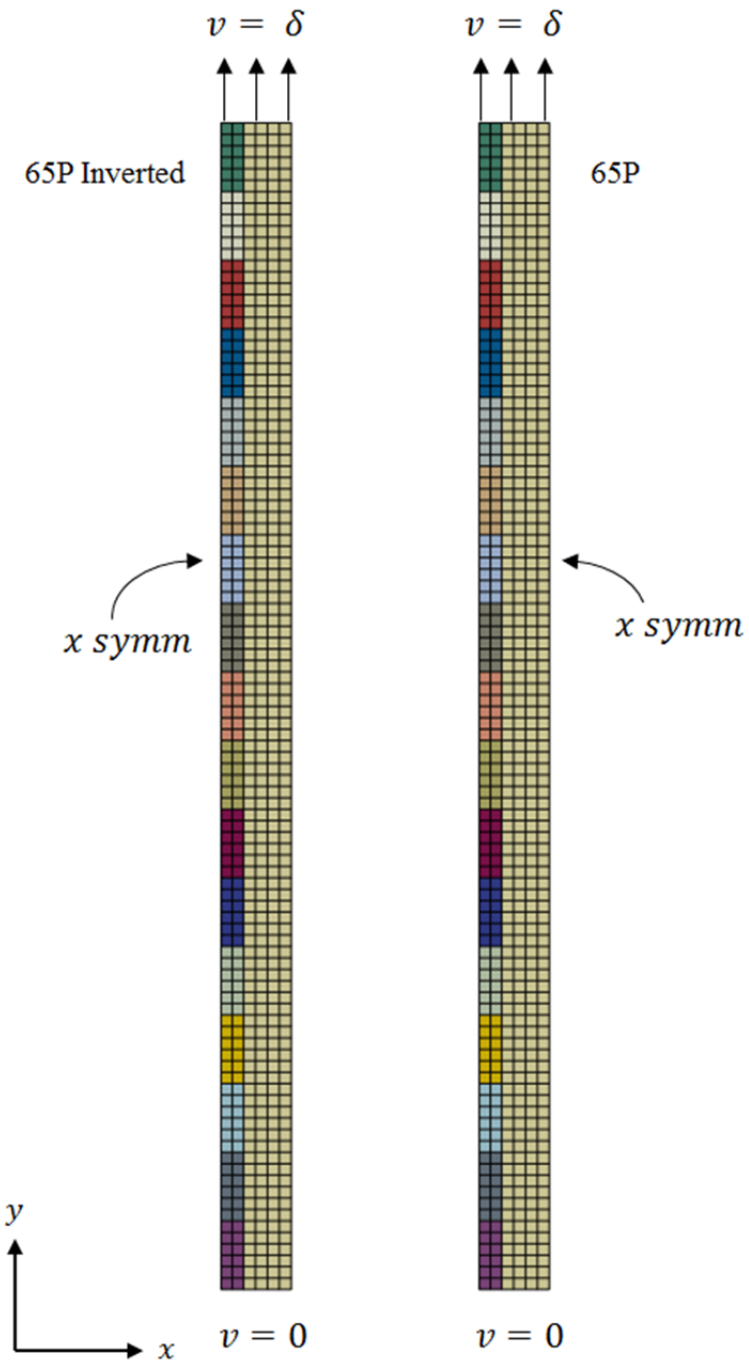

Figure 57. Hybrid simulation boundary conditions.

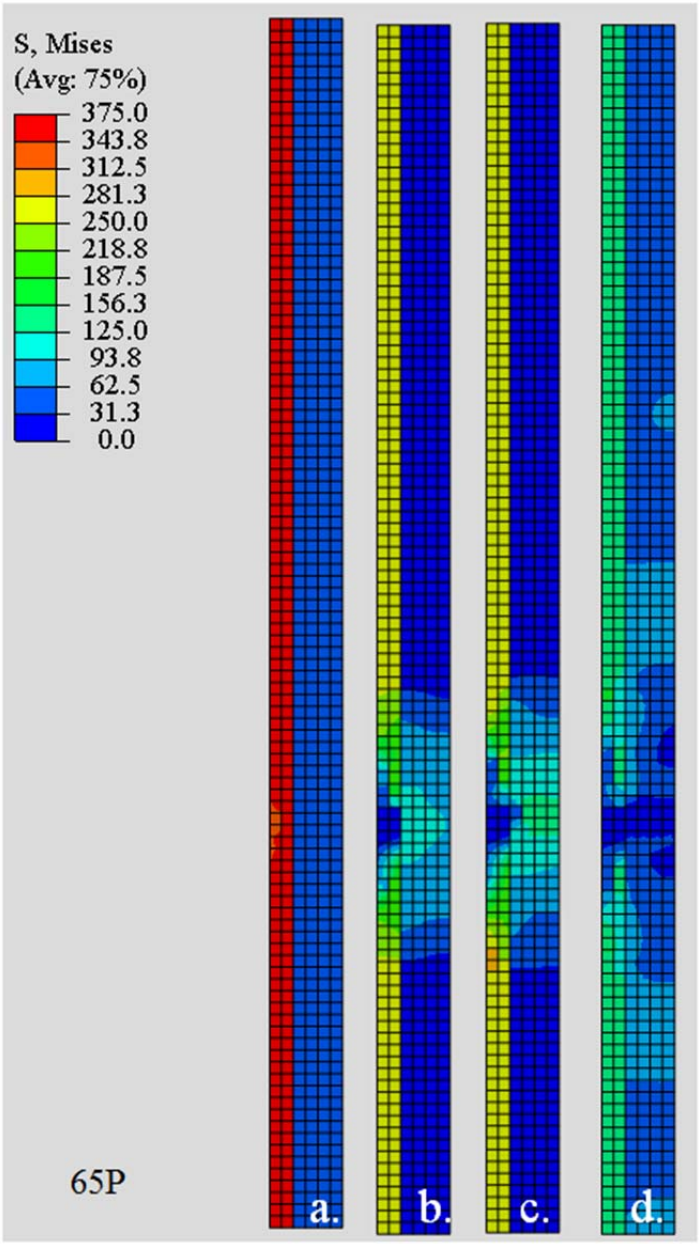

Figure 58. 65P hybrid model with outer Nextel™ layers Mises stress contours at (a) the onset of damage initiation in the Nextel™ section, (b) failure and unloading of some Nextel™ elements, (c) damage has propagated into the Saffil® layer, (d) full composite failure.

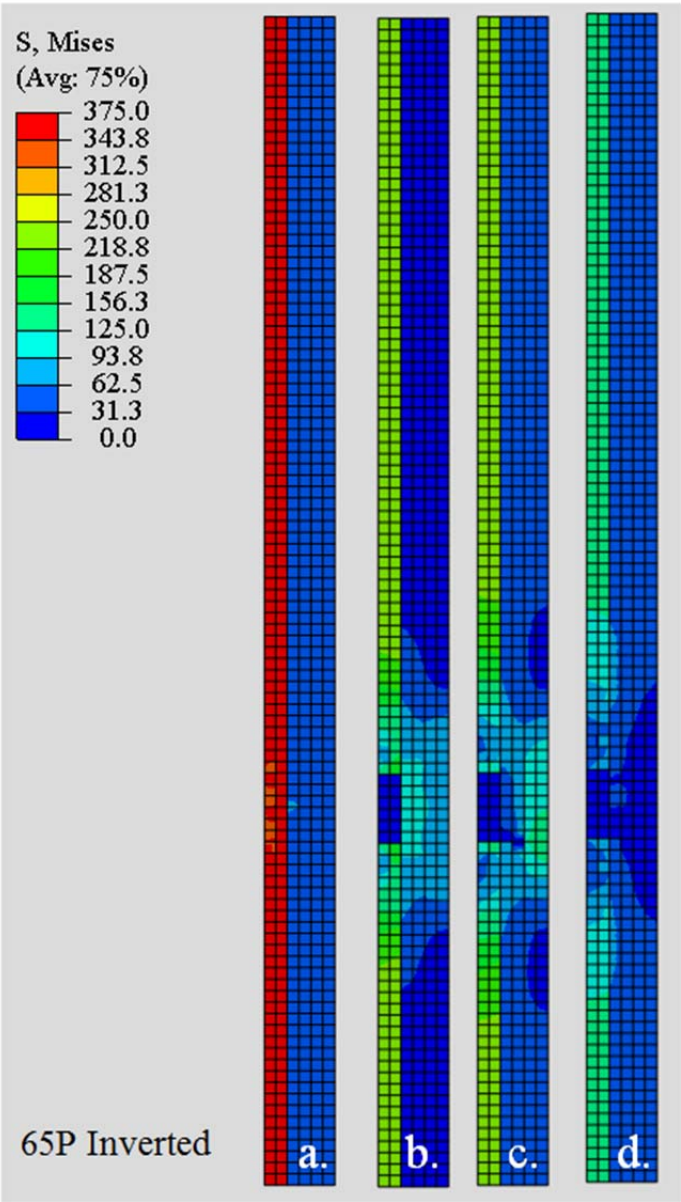

Figure 59. 65P Inverted hybrid model with inner Nextel™ layers Mises stress contours at (a) the onset of damage initiation in the Nextel™ section, (b) failure and unloading of some Nextel™ elements, (c) damage has propagated into the Saffil® layer, (d) full composite failure.

8.4 Hybrid Simulation Discussion

The uniaxial tension stress strain curves for the simulations and experiments can be found in Figure 60. The 65P Inverted experimental behavior does not follow the initial loading portion of the other three curves, this indicates the hybrid composite might have a higher volume fraction than hybrid 65P. Looking back at Table IV, 65P Inverted has a lower thickness than the 65P. Since the number of reinforcement layers are the same it is likely that there is less aluminum in the 65P Inverted, increasing the fiber volume fraction. The failure behavior of both simulations is different than the experimental results. Progressive failure was captured in the simulations however the load drop at the onset of cracking is much higher in the simulations than in the experiments. Additionally, only one crack is forming in the fabric layer in the simulations while multiple cracks were observed on the surfaces of the 65P samples. In the simulations, once one fabric section has failed the remaining fabric segments are not reaching their failure properties before the Saffil® layer fails. Another significant difference between the experiments and the model is hybrid 65P has a higher failure strain than 65P Inverted experimentally. The opposite of this is seen in the simulation results. Only one section of fabric composite failing in the simulation indicates less load is being transferred back into the fabric layer in the simulation than in the experiments.

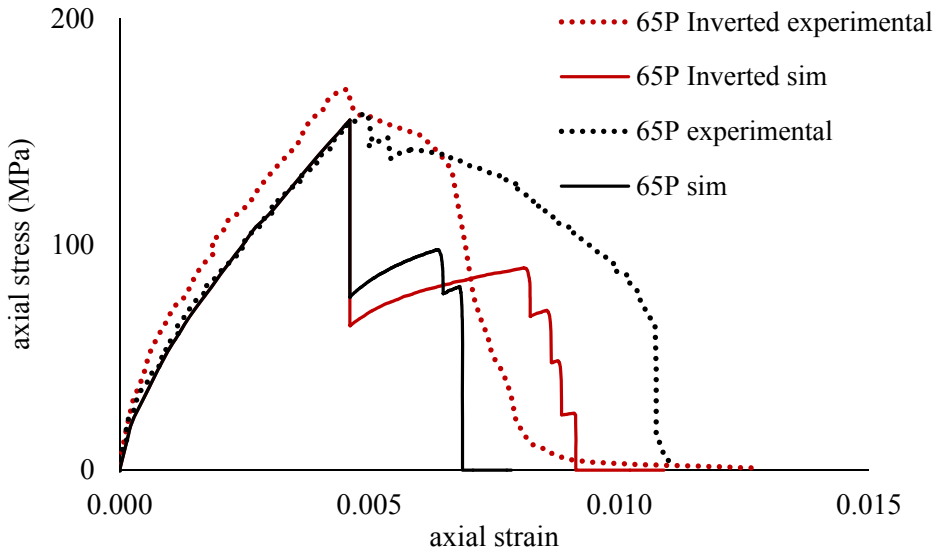

Figure 60. Uniaxial tension stress strain behavior for the simulated and experimental hybrid laminates 65P and 65P inverted.

Although the non-catastrophic failure of the hybrid composite was captured using this approach, it isn't predictive of the experimental tensile behavior after cracking. The simulation behaviors are significantly different than the experiments. Simulated failure behavior is more similar to the other hybrids characterized in this study with large drops in load at the onset of cracking. To improve the simulations failure behavior needs to be similar to the experiments with multiple cracks forming within the outer fabric layer in 65P. Since hybrid 65P had visible cracks this is the best place to start looking into improving the model to better fit the damage observed during testing. One possible way to do this would be to use connectors between the fabric segments. The connectors can be randomly assigned force displacement responses, including unloading, to simulate a crack opening between two fabric segments. Instead of failing large regions of fabric sections the connectors will be assigned the failure properties predicted in the fabric tensile simulation. This improvement should result in a lower load drop when a crack occurs as well as keeping the fabric layer at higher loads increasing the likelihood it will have multiple failures. The simulations are showing straight across failure through the Saffil® layer while the sample failure surfaces are showing shear failures through the Saffil® layer at approximately a 45° angle. In the simulation, a plane stress assumption was used. Employing a three-dimensional solution may better capture the hybrid failure characteristics.

The hybrid simulation attempt here was a starting point for beginning to understand how load is transferred between the continuous and discontinuous hybrid composite layers. In the future, advanced approaches should be used to further the simulation efforts of the hybrid laminates. Eventually, a local damage evolution model similar to Xia and Curtin's tensile simulation could be implemented. The simulation needs to be able to predict hybrid failure behavior for a range of continuous/discontinuous reinforcement ratios and layer volume fractions to identify hybrid laminates with high specific strength, specific stiffness, and modulus of toughness.

9 DISCUSSION

The goal of this work was to improve the toughness and failure strain of a continuous woven fiber reinforced metal matrix composite through hybridization with a discontinuous fiber reinforced composite while maintaining the continuous composite's strength and stiffness. Researchers have reported success in creating hybrid composites by reinforcing with two types of continuous fiber reinforcements, one having a high failure strain and the other a low failure strain. Hybrid composites using this approach have had failure strains up to three times higher than the low failure strain composite. Using a similar high and low failure strain hybrid composite approach, the continuous fabric composite, with a low failure strain of 0.42%, was laminated with one of two discontinuous composites with high failure strains of 7.5% and 2% respectively, to create continuous/discontinuous fiber reinforced hybrid composites. Two different discontinuous layers were used to determine continuous/discontinuous hybrid response. Hybrid composites with a discontinuous layer possessing a high failure strain but low strength (Saffil® paper 5% fiber volume fraction) versus a lower failure strain and a higher strength than Saffil® paper (Saffil® board 15% fiber volume fraction) were investigated. A total of six different continuous/discontinuous hybrid metal matrix composites were designed and characterized in uniaxial tension. Two of the hybrid laminates were created to observe the effects of having outer or inner continuous fabric reinforced composite layers (65P and 65P Inverted). Four additional hybrid composites were made to look at the effect of hybrid reinforcement ratio (continuous to discontinuous composite ratio by thickness) these hybrids included 48P, 54B, 63B, and 87B. The continuous/discontinuous fiber reinforced hybrid composites characterized exhibited a non-catastrophic uniaxial tension behavior resulting in hybrid composites with increased modulus of toughness (area under the axial stress-axial strain curve) and failure strain compared to the continuous fabric reinforced composite. During the hybrid composite uniaxial tension test, local damage occurred in the form of cracks within the continuous fabric composite layer causing a drop in the load carried in the sample. Initial cracking was typically followed by multiple loading/unloading curves until ultimate failure. Evidence of the cracking and unloading/reloading behavior was visible during the tensile tests of hybrid 65P by the author during the experiment, within the DIC axial strain fields, and on the failed sample surfraces. Two distinctly different failure behaviors were observed, following the onset of cracking, in the

hybrid composite: high strength and gradual unloading. The gradual unloading hybrids (65P and 65P Inverted) reached a little over half the strength of the continuous fabric reinforced composite and exhibited an effective damage response. Once the maximum load was reached, a small decrease in load was seen, approximately 10%, and was followed by stable damage propagation. 65P Inverted exhibited slow and steady unloading after the onset of cracking while 65P had multiple loading and unloading curves before gradually unloading to ultimate failure. Opposing the previous hybrid work done on high and low unidirectional fiber reinforced hybrid composites [5], in this work outer continuous (low failure strain) layers resulted in hybrids with a higher failure strain and modulus of toughness. High strength hybrids (48P, 54B and 63B) had a similar strength and stiffness as well as an improved cracking strain than the continuous fabric reinforced composite. After the onset of cracking, in the high strength hybrids, large decreases in load were observed with small reloading portions of the axial stress-axial strain curves making the progressive failure of these samples more catastrophic and abrupt than 65P and 65P Inverted. As evidenced in the tensile behavior, failed sample surfaces, and axial strain contours during the tensile test, the hybrid laminate response is greatly influenced by the amount and propagation of damage within the continuous fabric reinforced composite layer. Five of the six hybrid laminates characterized had a higher modulus of toughness or area under the axial stress-axial strain curve than the continuous fabric reinforced composite. Additionally, one of the hybrids, 48P, had a higher specific strength, specific stiffness and modulus of toughness than the continuous fabric reinforced composite. The ideal hybrid would have a combination of the two distinct hybrid behaviors observed resulting in a hybrid composite with a high strength, increased cracking strain, and stable damage propagation with gradual loading and unloading curves ultimately reaching strain values 3 to 4 times larger than the fabric composite. Characterization of six continuous/discontinuous fiber reinforced hybrid composites has revealed the importance of predicting cracking within the continuous fabric layer and has provided a basis to which hybrid tensile behavior predictions can be compared.

To design a hybrid with enhanced properties, modeling efforts are needed to determine discontinuous layer properties and the lamination scheme required to design future hybrid composites. As evidenced in the failure behavior, hybrid failure is controlled by the failure response of the continuous Nextel™ fabric composite layer. To simplify the complex fabric

composite geometry, it was looked at as consisting of continuously reinforced layers of axial and transverse fiber. Failure of the axial fiber reinforced composite was predicted using a tensile simulation while experimental results were used for the transverse layer. Fabric composite tensile simulations were performed by applying Xia and Curtin's stochastic damage evolution model [34]. This tensile simulation uses a multiscale approach to identify broken fiber segments, redistribute load to intact fiber segments near the break, and track the stress state within the composite until a catastrophic cluster of fiber breaks occurs resulting in ultimate failure. Inputs to the tensile simulation include continuous fiber properties, matrix properties, and composite geometry. Characterization of the continuous Nextel™ 610 fiber was performed using single fiber tension testing. Unprocessed and extracted fibers were characterized to quantify fiber damage during processing and to obtain as-processed fiber properties. A 15% decrease in fiber strength was measured due to damage induced during processing. Continuous composite predictions were then performed using unprocessed, extracted, and literature [27, 28] fiber properties. Continuous axial and fabric fiber reinforced composite strength predictions using the measured extracted fiber properties were within 10% of the experimental results. Predictions were within 25% of the experimental results when the unprocessed fiber properties were used while predictions using the fiber properties found in the literature had up to a 92% difference. In this work, fiber damage during processing had a significant effect on fiber properties and therefore the strength predictions. Nextel™ 610 fiber properties reported in the literature were not representative of the unprocessed (raw fibers taken from the tow) Nextel™ 610 3,000 and 10,000 denier fiber properties measured in this work. When possible, extracted fiber properties should be characterized and chosen over unprocessed fiber properties to be used as modeling inputs. Xia and Curtin's multiscale tensile simulation did a good job at predicting axial and fabric fiber reinforced composite strengths within 10% of the experimental and was used to predict cracking within the continuous fiber reinforced layers of the hybrid composite. The tensile simulation inputs included fiber and matrix properties as well as geometry; all inputs were obtained experimentally and reported in this work.

The final goal of this work was to begin development of a model to predict hybrid uniaxial tension failure behavior. An Abaqus finite element model was implemented using the predicted fabric composite strength distribution as an input. To allow for cracks to occur in the fabric layer,

similar to the experimental results, it was segmented and randomly assigned failure strains based on the predicted fabric composite axial stress-axial strain curves. Modeling the behavior of the discontinuous Saffil® reinforced composite was beyond the scope of this work and the experimental behavior was used. To describe failure of the continuous and discontinuous layers an elastic-plastic material model was implemented with a ductile damage failure criterion. Two hybrid laminates were modeled using this model and resulted in predicted failure behavior much different than the experimental results. Progressive failure was captured in the simulations however, the load drop at the onset of cracking is higher in the simulations than in the experiments. Additionally, only one crack occurred within the fabric layer in the simulations while multiple cracks were observed on the surfaces of the 65P samples. In the simulations, once one fabric section failed the remaining fabric segments were not reaching their failure properties before the Saffil® layer failed. This hybrid simulation is a starting point for beginning to understand the complex load transfer between the continuous and discontinuous hybrid composite layers. In the future, advanced approaches should be used to further the simulation efforts of the hybrid laminates. Eventually, a local damage evolution model similar to the continuous composite tensile simulation, which tracks local damage to determine the response of the hybrid laminate, would be beneficial towards the goal of designing enhanced toughness hybrid composites. The future hybrid simulation needs to be able to predict failures for a range of continuous/discontinuous reinforcement ratios and layer volume fractions to identify hybrid layups capable of producing high specific strength, specific stiffness, and modulus of toughness composites.

Five of the six MMC hybrids created in this work had increased toughness and specific stiffness compared to the continuous reinforced composite alone. One hybrid had a higher specific strength, specific stiffness and modulus of toughness compared to the continuous fiber reinforced composite. Hybrid uniaxial tension tests revealed cracking within the continuous fiber reinforced layer greatly influences continuous/discontinuous hybrid behavior. A stochastic damage evolution model was used to accurately predict cracking within the continuous fiber reinforced layers of the hybrid composite. Improvement of the hybrid model can lead to determining the reinforcement ratio and volume fractions necessary to obtain ideal hybrid properties and move one step closer to creating materials with mixed properties that currently do not coexist. In this

work the uniaxial tension properties of continuous/discontinuous hybrids were reported. In the future, characterization of the through-thickness hybrid composite properties using punch tests and iosipescu shear tests may be beneficial towards characterizing and understanding the impact behavior of these hybrids. The work performed here is a starting point for beginning to understand the mechanics behind continuous and discontinuous fiber-reinforced hybrid metal matrix composites. To date no researchers have reported uniaxial tension or impact behaviors for continuous/discontinuous fiber reinforced hybrid composites. Making this a new problem to solve with a wide range of applications where high specific strength, specific stiffness and toughness materials are needed.

10 REFERENCES

[1] Chin, E. S. C., 1999, "Army focused research team on functionally graded armor composites," Materials Science and Engineering A-Structural Materials Properties Microstructure and Processing, 259(2), pp. 155-161.

[2] Qiao, P. Z., Yang, M. J., and Bobaru, F., 2008, "Impact mechanics and high-energy absorbing materials: Review," Journal of Aerospace Engineering, 21(4), pp. 235-248.

[3] Hogg, P. J., 2006, "Composites in armor," Science, pp. 1100-1101.

[4] Deve, H. E., and Mccullough, C., 1995, "Continuous-Fiber Reinforced Al Composites - A New-Generation," Jom-Journal of the Minerals Metals & Materials Society, 47(7), pp. 33-37.

[5] Aveston, J., and Kelly, A., 1980, "Tensile First Cracking Strain and Strength of Hybrid Composites and Laminates," Phil. Trans. R. Soc. Lond. A, 294, pp. 519-534.

[6] Jung, S. W., Lee, J. H., Nam, J. B., Nam, H. W., and Han, K. S., 2000, "Analysis of strengthening mechanism in hybrid short fiber/particle reinforced metal matrix composites," Fracture and Strength of Solids, Pts 1 and 2, 183-1, pp. 1297-1302.

[7] Zhang, X. N., Geng, L., and Wang, G. S., 2006, "Fabrication of Al-based hybrid composites reinforced with SiC whiskers and SiC nanoparticles by squeeze casting," Journal of Materials Processing Technology, 176(1-3), pp. 146-151.

[8] Narasimalu, S., and Gupta, M., 2006, "Effect of the presence of continuous/discontinuous/hybrid reinforcement on the damping characteristics of pure aluminium matrix," Science and Technology of Hybrid Materials, 111, pp. 71-74.

[9] Gupta, M., Lai, M. O., and Lim, C. Y. H., 2006, "Development of a novel hybrid aluminum-based composite with enhanced properties," Journal of Materials Processing Technology, 176(1-3), pp. 191-199.

[10] Wong, W. L. E., Gupta, M., and Lim, C. Y. H., 2006, "Synthesis and characterization of hybrid aluminum composites reinforced with Ni particulates and interconnected Fe mesh," Science and Technology of Hybrid Materials, 111, pp. 39-42.

[11] Sadighi, M., Alderliesten, R. C., and Benedictus, R., 2012, "Impact resistance of fiber-metal lamiantes: a review," International Journal of Impact Engineering, 49, pp. 77-90.

[12] Fukuda, H., 1984, "An Advanced Theory of the Strength of Hybrid Composites," Journal of Materials Science, 19(3), pp. 974-982.

[13] Fukuda, H., and Chou, T. W., 1982, "Monte-Carlo Simulation of the Strength of Hybrid Composites," Journal of Composite Materials, 16(Sep), pp. 371-385.

[14] Fariborz, S. J., Yang, C. L., and Harlow, D. G., 1985, "The Tensile Behavior of Intraply Hybrid Composites 1. Model and Simulation," Journal of Composite Materials, 19(4), pp. 334-354.

[15] Jones, K. D., and Dibenedetto, A. T., 1994, "Fiber Fracture in Hybrid Composite Systems," Composites Science and Technology, 51(1), pp. 53-62.

[16] Zweben, C., 1977, "Tensile-Strength of Hybrid Composites," Astronautics & Aeronautics, 15(10), pp. B24-B24.

[17] Fukunaga, H., Chou, T. W., Schulte, K., and Peters, P. W. M., 1984, "Probabilistic Initial Failure Strength of Hybrid and Non-Hybrid Laminates," Journal of Materials Science, 19(11), pp. 3546-3553.

[18] Fariborz, S. J., and Harlow, D. G., 1987, "The Tensile Behavior of Intraply Hybrid Composites .2. Micromechanical Model," Journal of Composite Materials, 21(9), pp. 856-875.

[19] Dilandro, L., Dibenedetto, A. T., and Groeger, J., 1988, "The Effect of Fiber-Matrix Stress Transfer on the Strength of Fiber-Reinforced Composite-Materials," Polymer Composites, 9(3), pp. 209-221.

[20] ASTM-D3552, 2002, "Standard Test Method for Tensile Properties of Fiber Reinforced Metal Matrix,"ASTM International, West Conshohocken, PA.

[21] ASTM-E1012, 2005, "Standard Practice for Verification of Test Frame and Specimen Alignment Under Tensile and Compressive Axial Force Application,"ASTM International,West Conshohocken, PA.

[22] 3M, Ceramic Textiles Technical Notebook, http://www.3m.com/market/industrial/ceramics/pdfs/Nextel_Tech_Notebook_11.04.pdf.

[23] Communications with Eric Klier of the Army Research Laboratory, 2012, Aberdeen, MD.

[24] Saffil Ltd. online data sheet. www.saffil.com.

[25] Friend, C. M., 1987, "The Effect of Matrix Properties on Reinforcement in Short Alumina Fiber Aluminum Metal Matrix Composites," Journal of Materials Science, 22(8), pp. 3005-3010.

[26] Curtin, W. A., 1999, "Stochastic damage evolution and failure in fiber-reinforced composites," Advances in Applied Mechanics, Vol 36, 36, pp. 163-253.

[27] Gonczy, S., Wansom, S., and Goettler, R., "Tensile testing of oxide ceramic fibers in single filament and multifilament tow configurations," Proc. 24th Annual Conference on Composites, Advanced Ceramics, Materials, and Structurs: A: Ceramic Engineering and Science, T. Jessen, and E. Ustundag, eds., pp. 549-557.

[28] Wilson, D. M., 1997, "Statistical tensile strength of Nextel™ 610 and Nextel™ 720 fibres," Journal of Materials Science, 32(10), pp. 2535-2542.

[29] Asthana, R., Tewari, S. N., and Draper, S. L., 1998, "Strength degradation of sapphire fibers during pressure casting of a sapphire-reinforced Ni-base superalloy," Metallurgical and Materials Transactions A-Physical Metallurgy and Materials Science, 29(5), pp. 1527-1530.

[30] Draper, S. L., and Locci, I. E., 1994, "Al_2O_3 Fiber Strength Degradation in Metal and Intermetallic Matrix Composites," Journal of Materials Research, 9(6), pp. 1397-1411.

[31] Friler, J. B., Argon, A. S., and Cornie, J. A., 1993, "Strength and Toughness of Carbon-Fiber-Reinforced Aluminum Matrix Composites," Materials Science and Engineering a-Structural Materials Properties Microstructure and Processing, 162(1-2), pp. 143-152.

[32] Feih, S., Thraner, A., and Lilholt, H., 2005, "Tensile strength and fracture surface characterisation of sized and unsized glass fibers," Journal of Materials Science, 40(7), pp. 1615-1623.

[33] Weibull, W., 1939, "A Statistical Theory of the Strength of Materials," The Royal Swedish Institute for Engineering ResearchStockholm, Sweden.

[34] Xia, Z. H., and Curtin, W. A., 2001, "Multiscale modeling of damage and failure in aluminum-matrix composites," Composites Science and Technology, 61(15), pp. 2247-2257.

[35] Ibnabdeljalil, M., and Curtin, W. A., 1997, "Strength and reliability of fiber-reinforced composites: Localized load-sharing and associated size effects," International Journal of Solids and Structures, 34(21), pp. 2649-2668.

[36] Xia, Z., Curtin, W. A., and Okabe, T., 2002, "Green's function vs. shear-lag models of damage and failure in fiber composites," Composites Science and Technology, 62(10-11), pp. 1279-1288.

[37] Xia, Z., Curtin, W. A., and Peters, P. W. M., 2001, "Multiscale modeling of failure in metal matrix composites," Acta Materialia, 49(2), pp. 273-287.

[38] Zhang, F., Lisle, T., Curtin, W. A., and Xia, Z., 2009, "Multiscale modeling of ductile-fiber-reinforced composites," Composites Science and Technology, 69(11-12), pp. 1887-1895.

[39] Zhou, S. J., and Curtin, W. A., 1995, "Failure of Fiber Composites - a Lattice Green-Function Model," Acta Metallurgica Et Materialia, 43(8), pp. 3093-3104.

[40] Hedgepeth, J. M. V. D., P., 1967, "Local Stress Concentrations in Imperfect Filamentary Composite Materials," Journal of Composite Materials, 1, pp. 294-309.

[41] Landis, C. M., and McMeeking, R. M., 1999, "A shear-lag model for a broken fiber embedded in a composite with a ductile matrix," Composites Science and Technology, 59(3), pp. 447-457.

11 APPENDICES

11.1 APPENDIX A: VARIATION IN MEASURED PROPERTIES

Table VII. Standard deviations for properties of single reinforcement composites and neat aluminum matrix reported in Table III.

Composite	**Strength** (**MPa**)	**Modulus** (**GPa**)	**Failure Strain** (%)	**Yield Stress** (**MPa**)	**Poisson's Ratio**	**Density** $\left(\frac{\mathbf{g}}{\mathbf{mm^3}}\right)$	**Modulus of Toughness** $\left(\mathbf{MPa}\cdot\frac{\mathbf{mm}}{\mathbf{mm}}\right)$	**Volume Fraction** (%)	**Thickness** (**mm**)	**Population Size**
	Measured Standard Deviations									
Nextel™ Fabric	10	14	0.04	5	0.05	0.03	0.05	2.87	0.04	5
Saffil® Paper	10	12	3.42	5	0.07	0.01	2.06	0.83	0.06	11
Saffil® Board	10	14	1.21	4	0.03	0.01	2.53	0.93	0.04	5
Al-2Cu* *no reinforcement	20	6	2.96	7	0.05	0.01	4.42	-	0.14	10
Nextel™ Unidirectional	180	12	0.09	-	0.08	0.01	1.01	1.09	0.59	15
Nextel™ Transverse	10	13	0.08	23	0.02	0.03	0.10	2.93	0.03	14

Table VIII. Standard deviations for hybrid composite properties listed in Table IV.

Hybrid Composite	**Layup**	**Strength (MPa)**	**Modulus (GPa)**	**Cracking Strain (%)**	**Failure Strain (%)**	**Density $\left(\frac{g}{mm^3}\right)$**	**Modulus of Toughness $\left(MPa \cdot \frac{mm}{mm}\right)$**	**Thickness (mm)**	**Population Size**
		Measured Standard Deviations							
65P	$[N/P]_s$	10	3	0.02	0.16	0.08	0.18	0.11	11
65P Inverted	$[P/N]_s$	10	13	0.07	0.25	0.01	0.23	0.07	9
48P	$[N_2/P]_s$	10	6	0.06	0.07	0.02	0.09	0.07	10
87B	$[N/B]_s$	10	10	none	0.39	0.01	0.71	0.08	8
63B	$[N_2/B/N_2]$	10	7	0.06	0.06	0.01	0.11	0.08	15
54B	$[N_3/B/N_3]$	20	8	0.08	0.15	0.01	0.17	0.02	9

† Standard deviations for each of the properties listed in Table III can be found in Appendix A.

11.2 APPENDIX B: UNIAXIAL TENSION STRESS-STRAIN CURVES

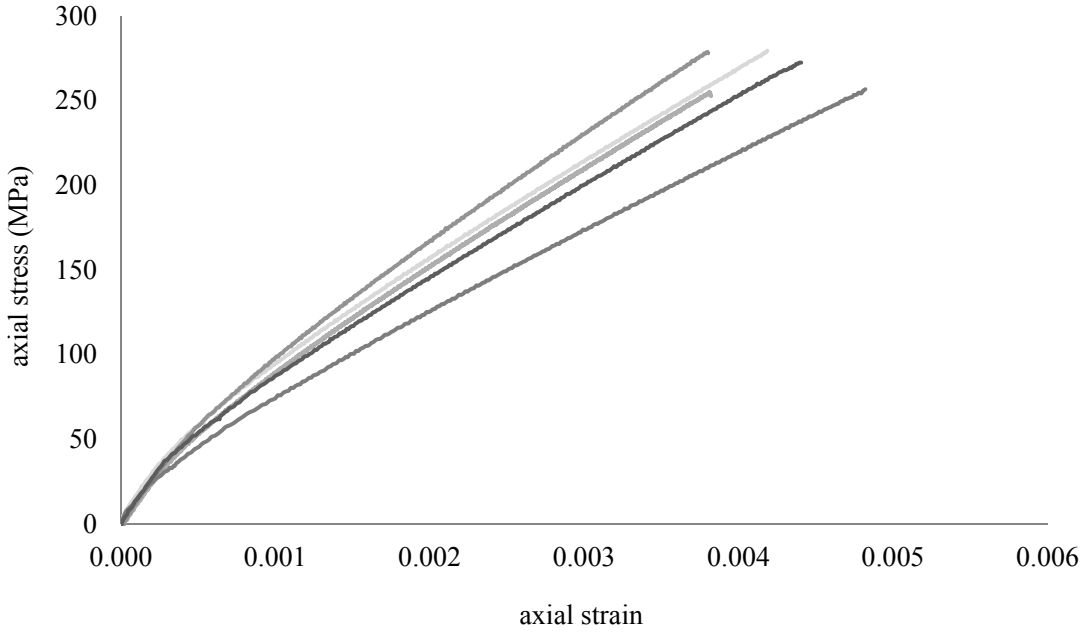

Figure 61. Nextel™ fabric reinforced composite sample uniaxial tension behavior.

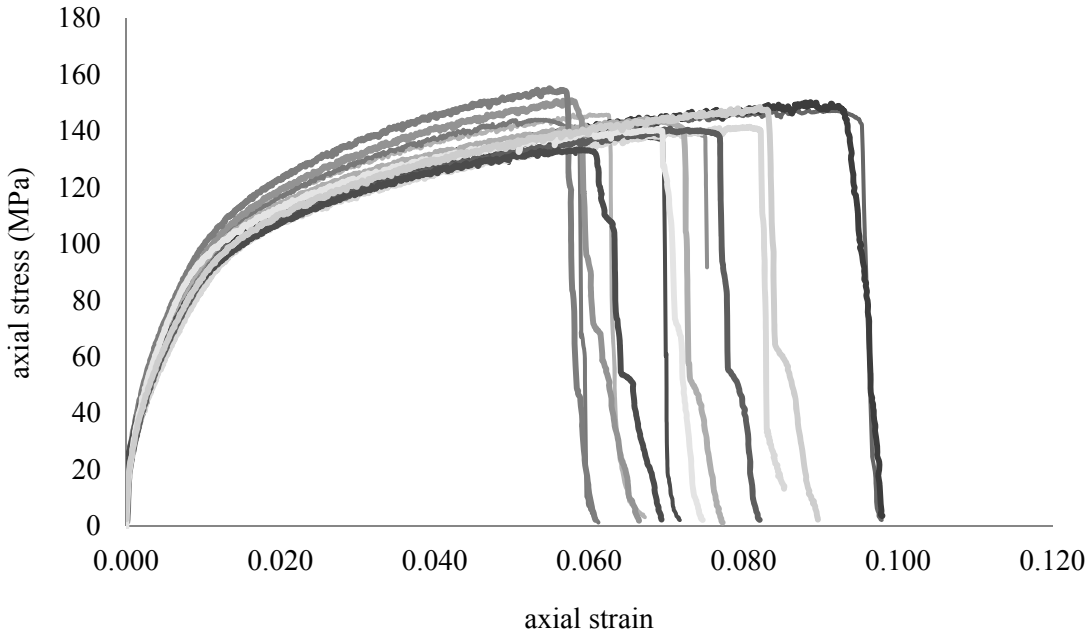

Figure 62. Saffil® paper reinforced composite samples uniaxial tension behavior.

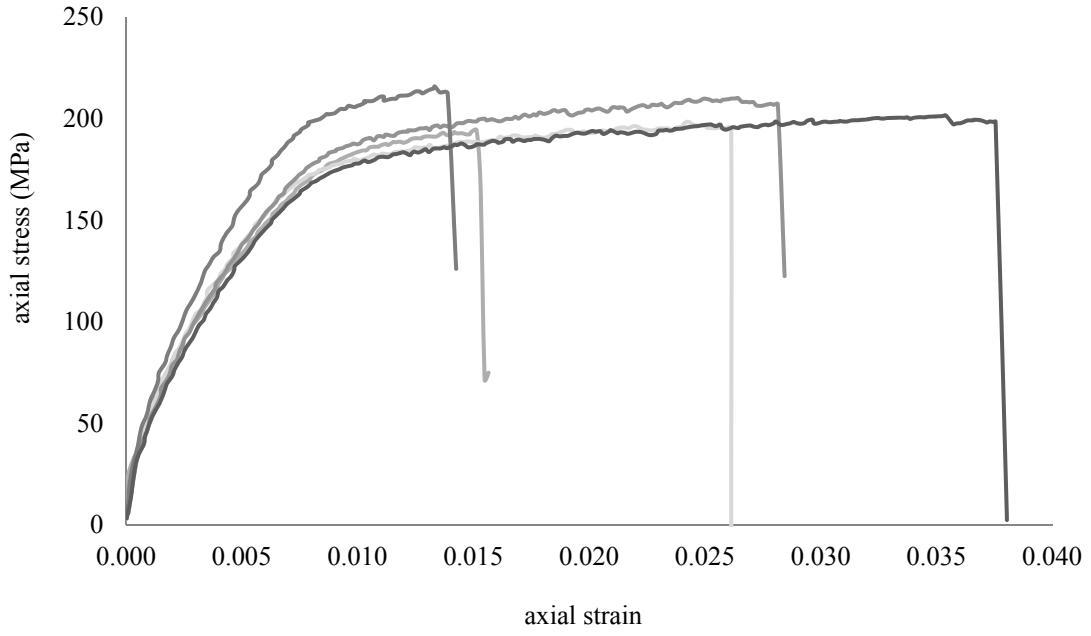

Figure 63. Saffil® board reinforced composite samples uniaxial tension behavior.

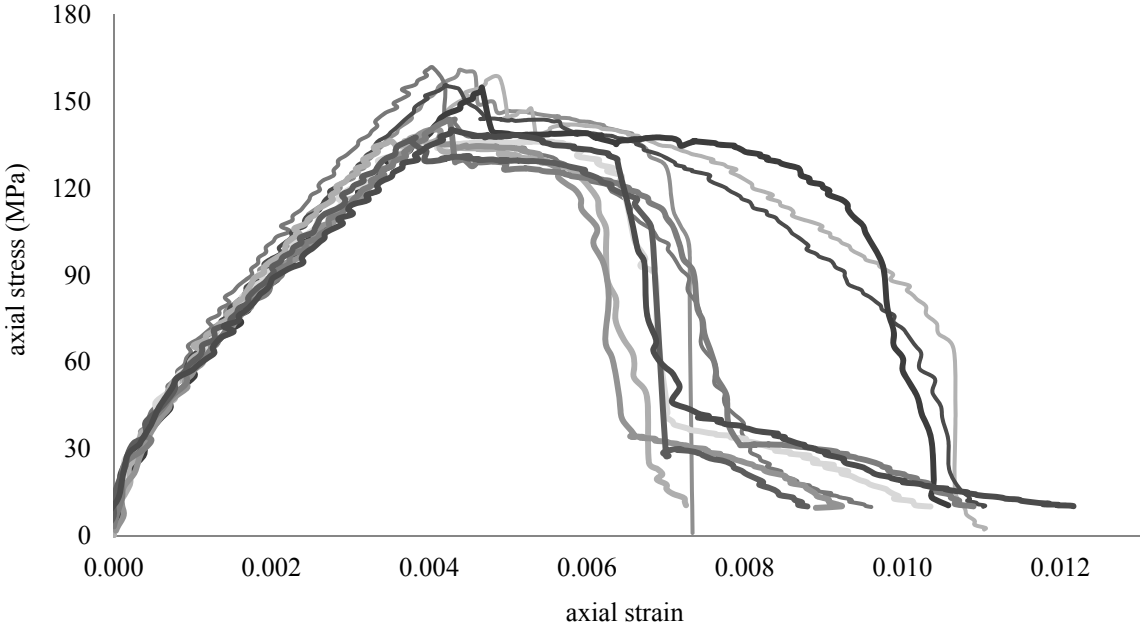

Figure 64. Hybrid composite 65P samples uniaxial tension behavior.

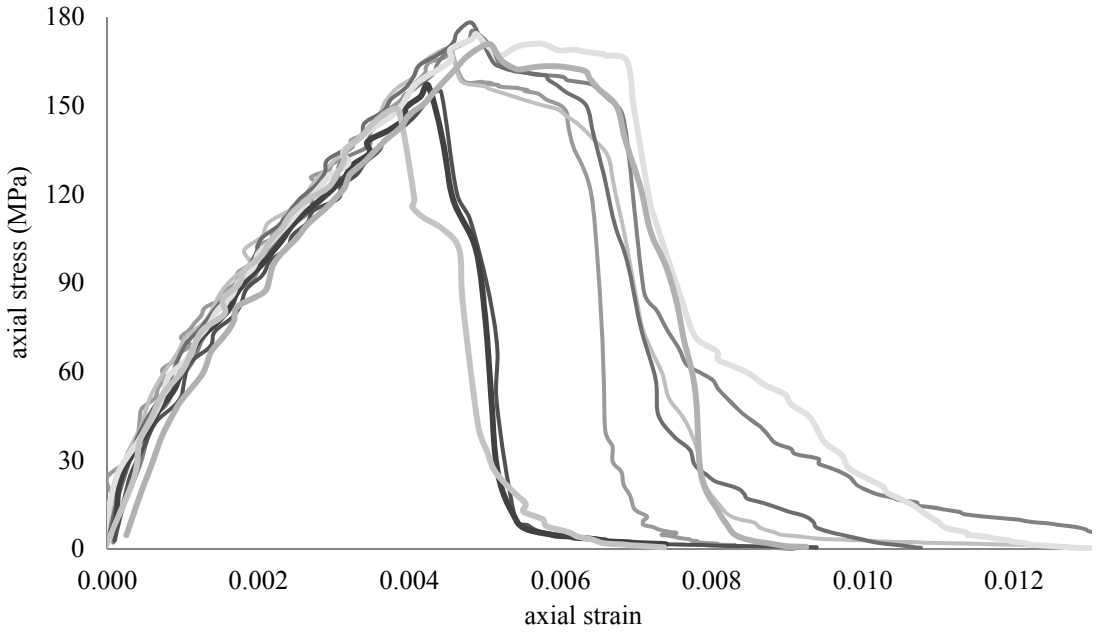

Figure 65. Hybrid composite 65P Inverted samples uniaxial tension behavior.

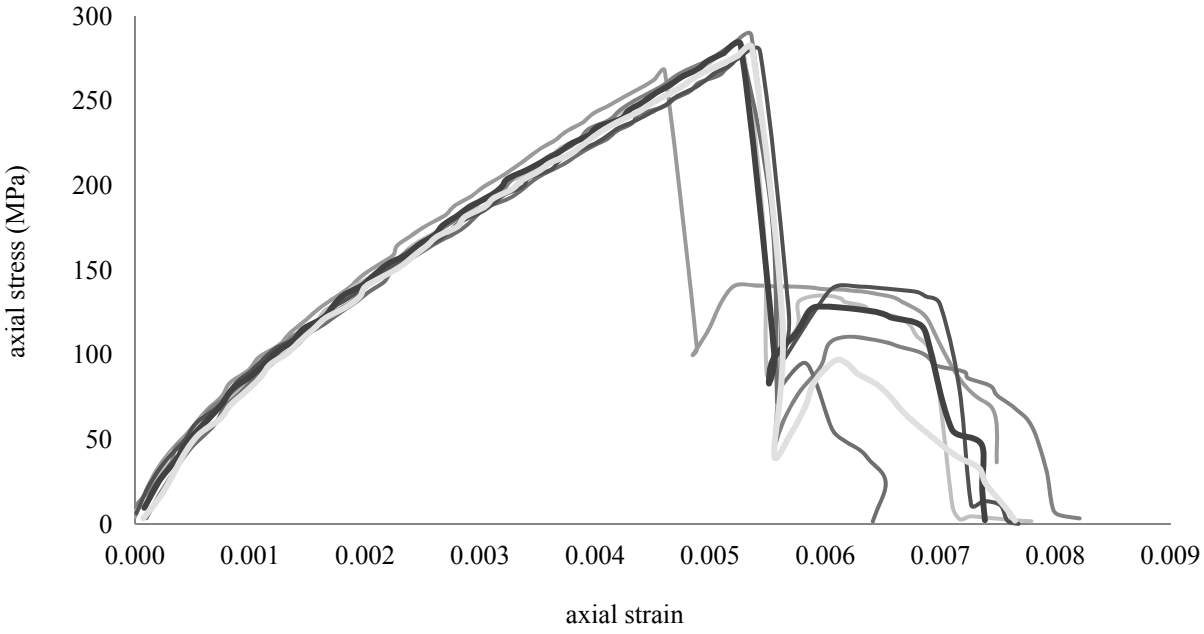

Figure 66. Hybrid composite 48P samples uniaxial tension behavior.

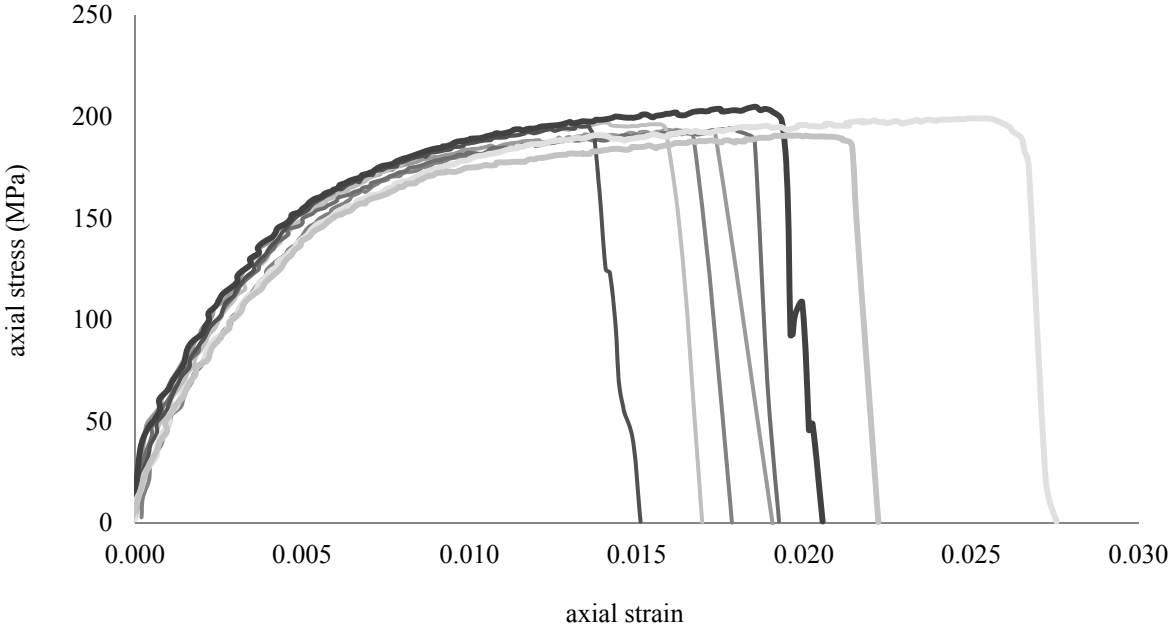

Figure 67. Hybrid composite 87B samples uniaxial tension behavior.

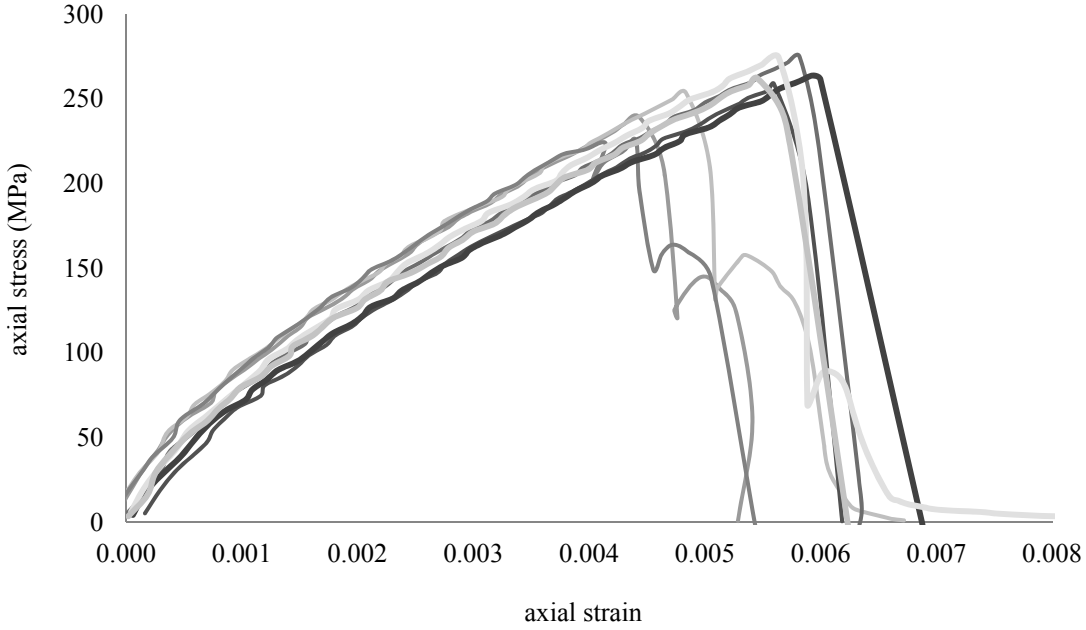

Figure 68. Hybrid composite 63B samples uniaxial tension behavior.

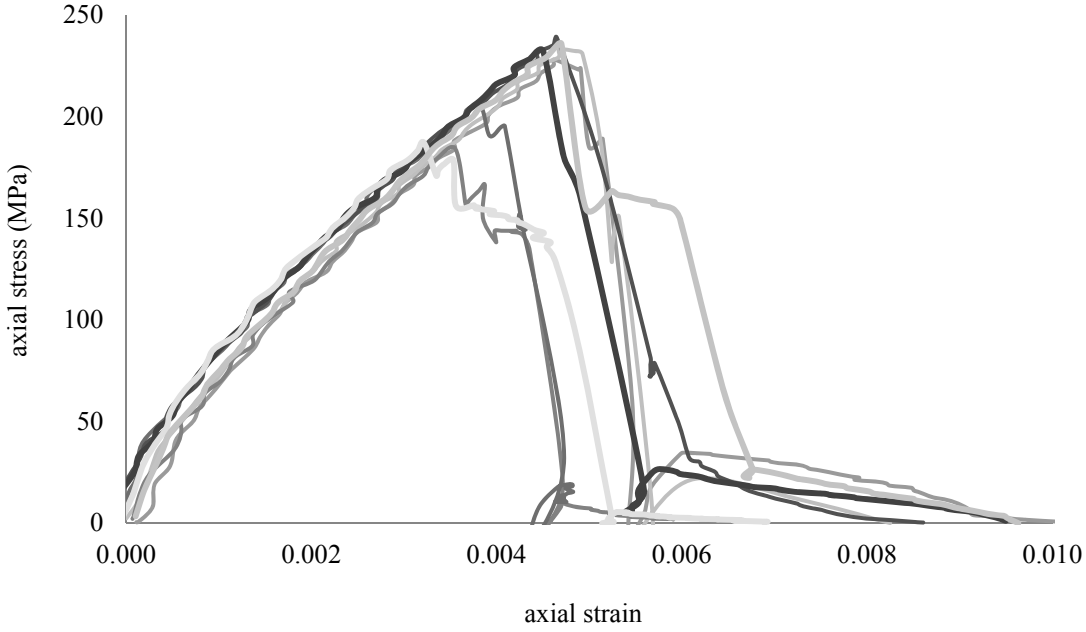

Figure 69. Hybrid composite 54B samples uniaxial tension behavior.

11.3 APPENDIX C: COPYRIGHT PERMISSIONS

THE ROYAL SOCIETY LICENSE
TERMS AND CONDITIONS

Apr 03, 2013

This is a License Agreement between Jessica Dibelka ("You") and The Royal Society ("The Royal Society") provided by Copyright Clearance Center ("CCC"). The license consists of your order details, the terms and conditions provided by The Royal Society, and the payment terms and conditions.

License Number	3121181127034
License date	Apr 03, 2013
Licensed content publisher	The Royal Society
Licensed content publication	Philosophical Transactions A
Licensed content title	Tensile First Cracking Strain and Strength of Hybrid Composites and Laminates
Licensed copyright line	Copyright © 1980, The Royal Society
Licensed content author	J. Aveston, A. Kelly
Licensed content date	1980
Volume number	294
Issue number	1411
Type of Use	Thesis/Dissertation
Requestor type	academic/educational
Format	print and electronic
Portion	figures/tables/images
Quantity	5
Will you be translating?	no
Circulation	1
Title of your thesis / dissertation	Mechanics of Hybrid Metal Matrix Composites
Expected completion date	Apr 2013
Estimated size (number of pages)	110

ELSEVIER LICENSE
TERMS AND CONDITIONS

Apr 03, 2013

This is a License Agreement between Jessica Dibelka ("You") and Elsevier ("Elsevier") provided by Copyright Clearance Center ("CCC"). The license consists of your order details, the terms and conditions provided by Elsevier, and the payment terms and conditions.

All payments must be made in full to CCC. For payment instructions, please see information listed at the bottom of this form.

Supplier	Elsevier Limited The Boulevard,Langford Lane Kidlington,Oxford,OX5 1GB,UK
Registered Company Number	1982084
Customer name	Jessica Dibelka
License number	3121181509919
License date	Apr 03, 2013
Licensed content publisher	Elsevier
Licensed content publication	Composites Science and Technology
Licensed content title	Multiscale modeling of damage and failure in aluminum-matrix composites
Licensed content author	Z.H Xia,W.A Curtin
Licensed content date	November–December 2001
Licensed content volume number	61
Licensed content issue number	15
Number of pages	11
Start Page	2247
End Page	2257
Type of Use	reuse in a thesis/dissertation
Intended publisher of new work	other
Portion	figures/tables/illustrations
Number of figures/tables/illustrations	5
Format	both print and electronic
Are you the author of this Elsevier article?	No
Will you be translating?	No
Title of your thesis/dissertation	Mechanics of Hybrid Metal Matrix Composites
Expected completion date	Apr 2013

Estimated size (number of pages)	110
Elsevier VAT number	GB 494 6272 12